Part II :

SOLAR ROTATION

Paul Charbonneau

HAO/NCAR (FL2, room 3022)

tel. 497-1594

email: paulchar@hao.ucar.edu

1. ANGULAR MOMENTUM LOSS AND SOLAR ROTATION

"Les observations sont l'histoire de la physique, et les systèmes en sont la fable."

Montesquieu
Mes pensées (1755?)

In this chapter we consider a number of issues, observational and theoretical, that have important bearing on the topic of solar rotation. We begin by a quick survey (§1.1) of solar and stellar rotation measurements, to identify the set of observational constraints to be met by models to be constructed in subsequent chapters. We continue (§1.2) by examining the circumstances under which stellar evolution in itself can lead to changes in surface rotation rates. Equipped with this knowledge and drawing on results from part I of the course, we construct our first, very simple rotational evolution model (§1.3), and compare its predictions to observations (§1.4).

1.1 The rotation of solar-type stars

The solar rotation was first observed in the early seventeenth century, as various astronomers more or less simultaneously turned the newly invented astronomical telescope toward the Sun. The best remembered historical figures to do so were Galileo Galilei (1564-1642) and the Jesuit Christoph Scheiner (1575-1650), but the first person to actually see sunspots through a telescope appears to have been the Englishman Thomas Harriott (1560-1621) on December 8 1610, and the first person to publish was certainly the young Dutch Johannes Fabricius (1587-1616), who in 1611 published a small pamphlet entitled *De maculis in sole observatis*. Harriott did not pursue the matter much further, and Fabricius soon thereafter met with an untimely death from the plague. Consequently, most of the rhetorical battles on the nature of sunspots occurred between Galileo and Scheiner (and their respective supporters and followers), turning the two astronomers into bitter enemies to the end of their lives.

Figure 1.1 is a reproduction of one of many drawings in Scheiner's massive sunspot work entitled *Rosa Ursina sive Sol*, showing the apparent path of sunspots across the solar disk, at different times of the year. Once the original debate on the physical nature of sunspots resolved itself in favor of sunspots being actual

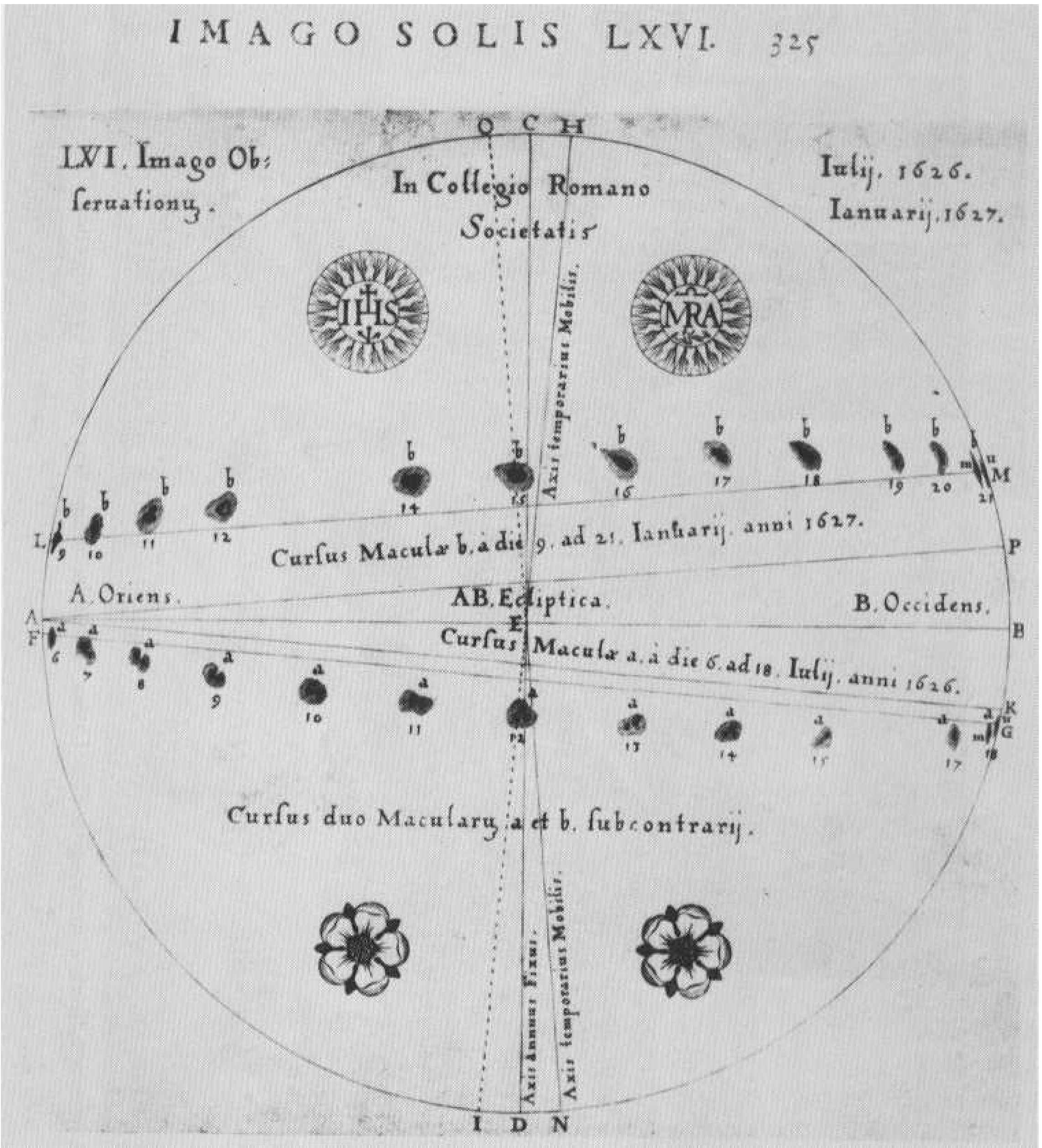

Figure 1.1: Diagram from C. Scheiner's *Rosa Ursina*, showing the apparent paths of sunspots across the solar disk, over two distinct two week periods separated by six months. From the angle between the two sunspots paths Scheiner correctly inferred that the Sun's rotation axis is inclined by about 7 degrees with respect to the ecliptic.

blemishes on the solar surface (rather than shadows of hitherto unknown small intramercurial planets, Scheiner's original position), astronomers such as Scheiner and Galileo were quick to use this motion to infer the axial rotation period of the

Sun, which Galileo estimated equal to a lunar month (about 28 days). Subsequent similar determinations carried out by other astronomers over the next two centuries produced comparable values, but never seemed to agree exactly with one another.

This situation was finally resolved in 1863 when R.C. Carrington showed, on the basis of a decade of assiduous sunspots observations, that the Sun rotates *differentially*, in the sense that the rotation period inferred from the apparent azimuthal motion of "tracers" such as sunspots is a function of the heliocentric latitude at which those tracers are located. The existence of the solar surface differential rotation was soon confirmed by H.C. Vogel in 1871, by measurements of the Doppler shift of solar spectral lines. Carrington originally parametrized the latitudinal differential rotation as[1]

$$\Omega(\theta) = 14.42 - 2.75 \cos^{7/4} \theta, \qquad [\text{deg day}^{-1}] \tag{1.1a}$$

where θ is the colatitude (i.e., the angle as measured from the pole)[2]. Subsequently, it has become customary to use instead something like

$$\Omega(\theta) = a - b \cos^2 \theta - c \cos^4 \theta, \tag{1.1b}$$

with the last term often omitted when dealing with sunspots, since they are seldom seen at high heliospheric latitudes. It turns out that the values of the numerical coefficients a, b, c in (1.1b) depends somewhat on the type of tracers followed to establish the latitudinal rotation profile: small spots rotate a little faster than large spots, and sunspot groups a little slower than individual spots, or faculae, or small-scale magnetic features. Moreover, all of those differ slightly from Doppler measurements in photospheric spectral lines. An extensive study of sunspot motions covering the interval 1921–1982, from white light photographic plates taken at Mt Wilson, yields the following best fit for the full dataset:

$$\Omega(\theta) = 14.522(\pm 0.004) - 2.840(\pm 0.043) \cos^2 \theta, \qquad [\text{deg day}^{-1}]\,\text{Sunspots}, \tag{1.1c}$$

with variations at the 1—2% level if groups or small spots or large spots are considered separately. The best fit for Doppler measurements, on the other hand, is

$$\Omega(\theta) = 13.76(\pm) - 1.74(\pm) \cos^2 \theta - 2.19 \cos^4 \theta, \qquad [\text{deg day}^{-1}]\,\text{Doppler}, \tag{1.1d}$$

The next quantum leap in our observational knowledge of solar rotation occurred in the past two decades, with the advent of *helioseismology*, which allows the

---

[1] Most observers still parametrize the solar surface differential rotation in terms of the *latitude* ($\pi/2 \leq \lambda \leq \pi/2$), i.e., the angle measured from the equatorial plane, rather than the colatitude angle $0 \leq \theta \leq \pi$ of the usual spherical polar coordinate. To get the equivalent of eqs. (1.1) for latitudes, simply replace the cosines by sines.

[2] What is the surface linear zonal velocity (in meters per seconds) at the solar equator?

determination of the *internal* solar rotation. This will be discussed at length in the next chapter.

The rotation of a star other than the Sun was first measured serendipitously at the beginning of this century by F. Schlesinger, in the bright component of the eclipsing binary δLibrae at occultation. Subsequent determinations of rotation rates for single stars relied on Doppler *broadening* of stellar spectral lines, as first suggested by W.W. Abney in 1877, but first successfully carried out much later by C.T. Elvey in 1929. For a single star, this projected rotational velocity ($v \sin i$) yields only a *lower limit* to the true equatorial rotation rate ($v_{\rm eq}$), as the angle i between the line of sight and the star's rotation axis is generally unknown.

As spectroscopic determinations of $v \sin i$ for a growing sample of single stars accumulated, the existence of systematic differences between average rotation rates for late-type and early-type stars was almost immediately recognized. Figure 1.2 herein is a reproduction of a diagram put together by R. Kraft in 1967, showing the distribution of rotation rates in an observational Hertzsprung-Russell diagram, for a sample of field stars. As one runs down the main-sequence, there is a sharp break in $v \sin i$ at spectral type F5. Stars on the cool side of this so-called rotational dividing line rotate rather slowly, while on the hot side rapid rotation is the rule. Kraft went on to show that under the assumption of internal solid-body rotation, in the interval $1.5 \lesssim M/M_\odot \lesssim 20$ the observed rotation rates are consistent with a power law dependence for the total angular momentum content (J) on stellar mass (M) of the form

$$J \propto M^{1.57}, \tag{1.2}$$

since then commonly referred to as Kraft's relation.

A number of hypotheses can be considered to explain the presence of the observed rotational break at F5. Late-type stars could divert a considerable fraction of their initial angular momentum content into planetary orbital angular momentum, or hide it from view in very rapidly rotating cores. Alternately, late-type stars could simply emerge from the star formation process with intrinsically less angular momentum per unit mass than early-type stars.

The preferred alternative, already then and still now, is that late-type stars experience *spin-down* during their main-sequence lifetime, through a mechanism that operates much less efficiently —or not at all— in early-type stars. This was perhaps best illustrated by A. Skumanich, in what is now a true classic diagram, reproduced here as Figure 1.3. Going beyond the then growing consensus that solar-type stars experience spin-down on the main-sequence, Skumanich used rotation rate data available for the Pleiades, Hyades and the Sun to show that the rotation rate of solar-type stars decreased in time in proportion to $t^{-1/2}$. This is now usually referred to as Skumanich's relation. Skumanich went still further and argued that chromospheric activity —a tracer of magnetic activity,— as measured by emission in the core of the CaH+K line, followed a similar decline. The relationship between rotation and magnetic activity represents the most fundamental aspect of solar magnetism, and will be dealt with at length in part IV of this course.

Subsequent observational work revealed that although the Skumanich relation

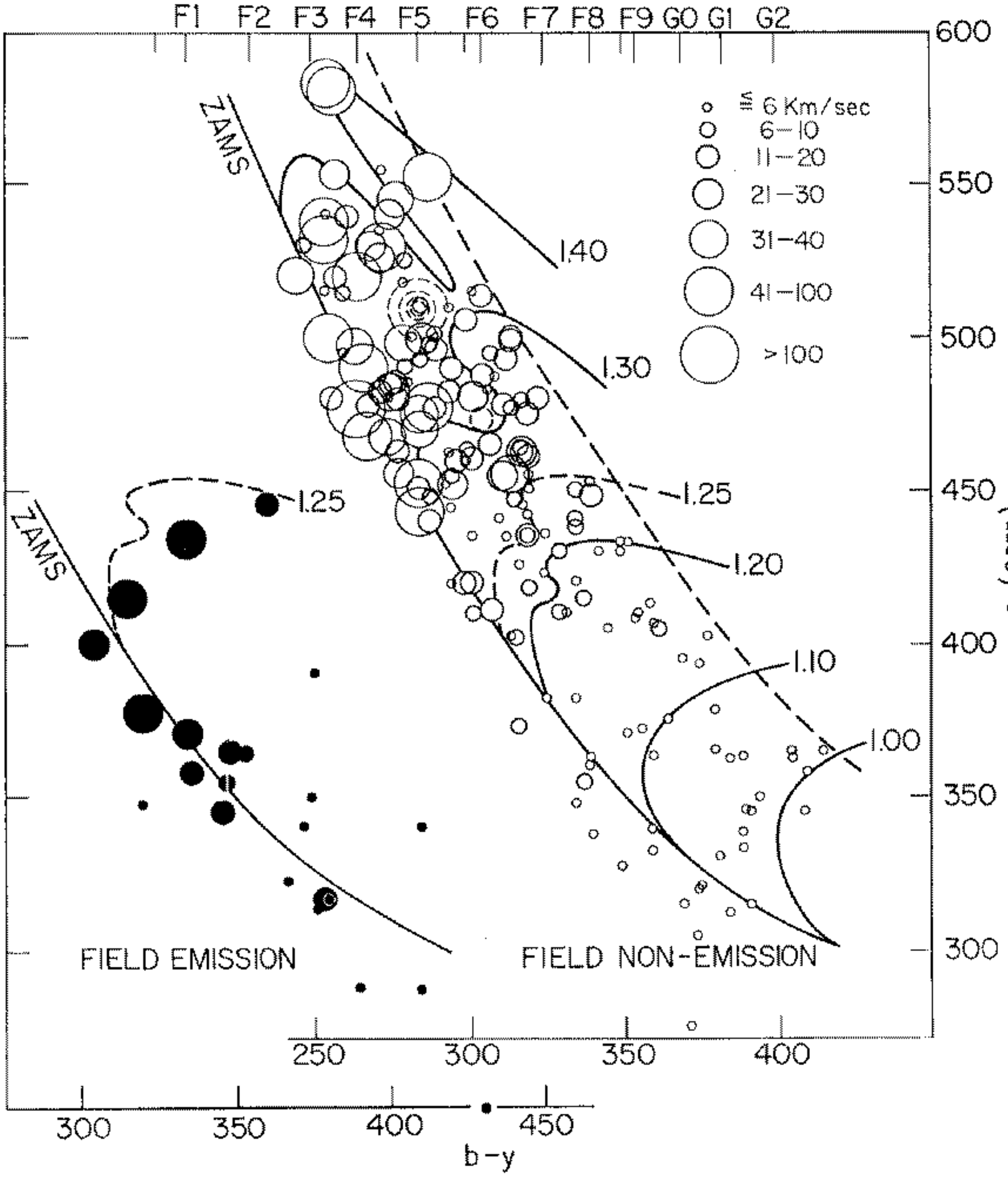

Figure 1.2: Distribution of projected rotational velocities for main-sequence stars, plotted in an observational HR diagram. Luminosity increases vertically upwards, and surface (effective) temperature horizontally *leftward.* Astronomical spectral types are listed along the upper axis. Solid lines are stellar evolutionary tracks, labeled according to mass in solar units. These tracks, especially for $M/M_\odot \gtrsim 1.2$, would today be considered obsolete. Figure reproduced from Kraft, R. 1967, ApJ, 150, 551 (Figure 1, p. 558).

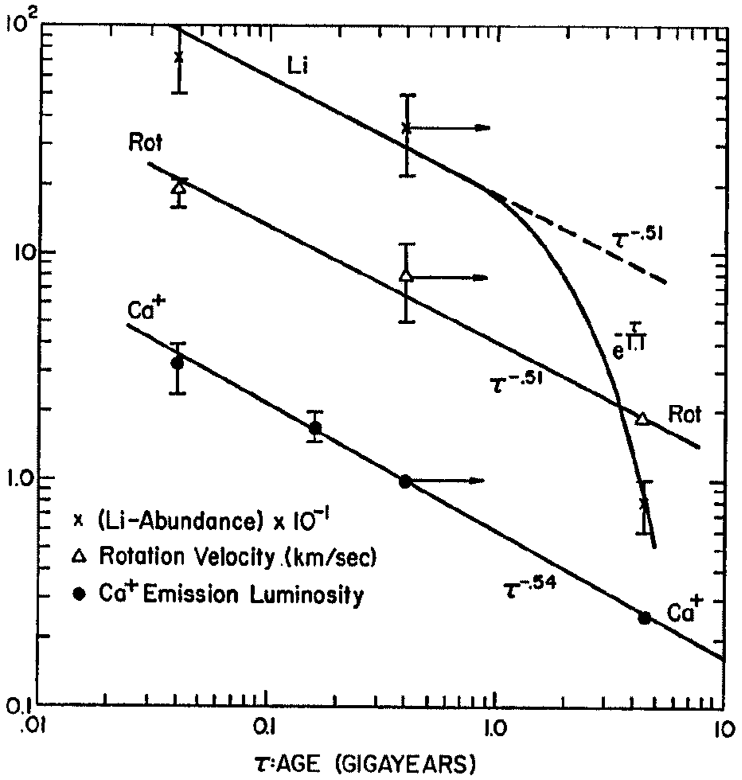

Figure 1.3: Evolution of rotation rates, Calcium emission, and Lithium abundances in main-sequence solar-type stars. Figure reproduced from Skumanich, A. 1972, ApJ, 171, 565 (Figure 1, p. 566).

held only for relatively old stars (i.e., age $\gtrsim 1\,\mathrm{Gyr}$), the main-sequence spin-down of solar-type stars is an observational fact. However, many new observations posed problems for the simple picture suggested by Skumanich's relation. The discovery of very rapidly rotating ($\gtrsim 200\,\mathrm{km\,s^{-1}}$) K-dwarfs in the Pleiades in the early 1980's is one such example. In addition, as gradual improvement in observational techniques and data analysis pushed the upper limit on observed $v \sin i$ below $10\,\mathrm{km\,s^{-1}}$, it became clear that many stars in young clusters actually rotate much slower than the $t^{-1/2}$ relationship would suggest. Figure 1.4 shows modern rotational velocity data for solar-type stars in three young stars clusters: αPersei, age $\simeq 50\,\mathrm{Myr}$; the Pleiades, age $\simeq 70\,\mathrm{Myr}$; and the Hyades, age $\simeq 600\,\mathrm{Myr}$. The following are some noteworthy aspects of the rotational evolution of solar-type stars that can be inferred from the data of Figure 1.4:

- Solar-type stars arrive on the ZAMS with a very broad range of rotation rates, from the current detection limit at $\sim 8\,\mathrm{km\,s^{-1}}$ up to $\sim 200\,\mathrm{km\,s^{-1}}$.

- Early on the main-sequence (αPersei and Pleiades), in any given temperature range there exists an excess of slow rotators ($v \sin i \lesssim 10\,\mathrm{km\,s^{-1}}$), with respect to what one would expect from a Maxwellian rotational velocity distribution and random orientations of projection axes.

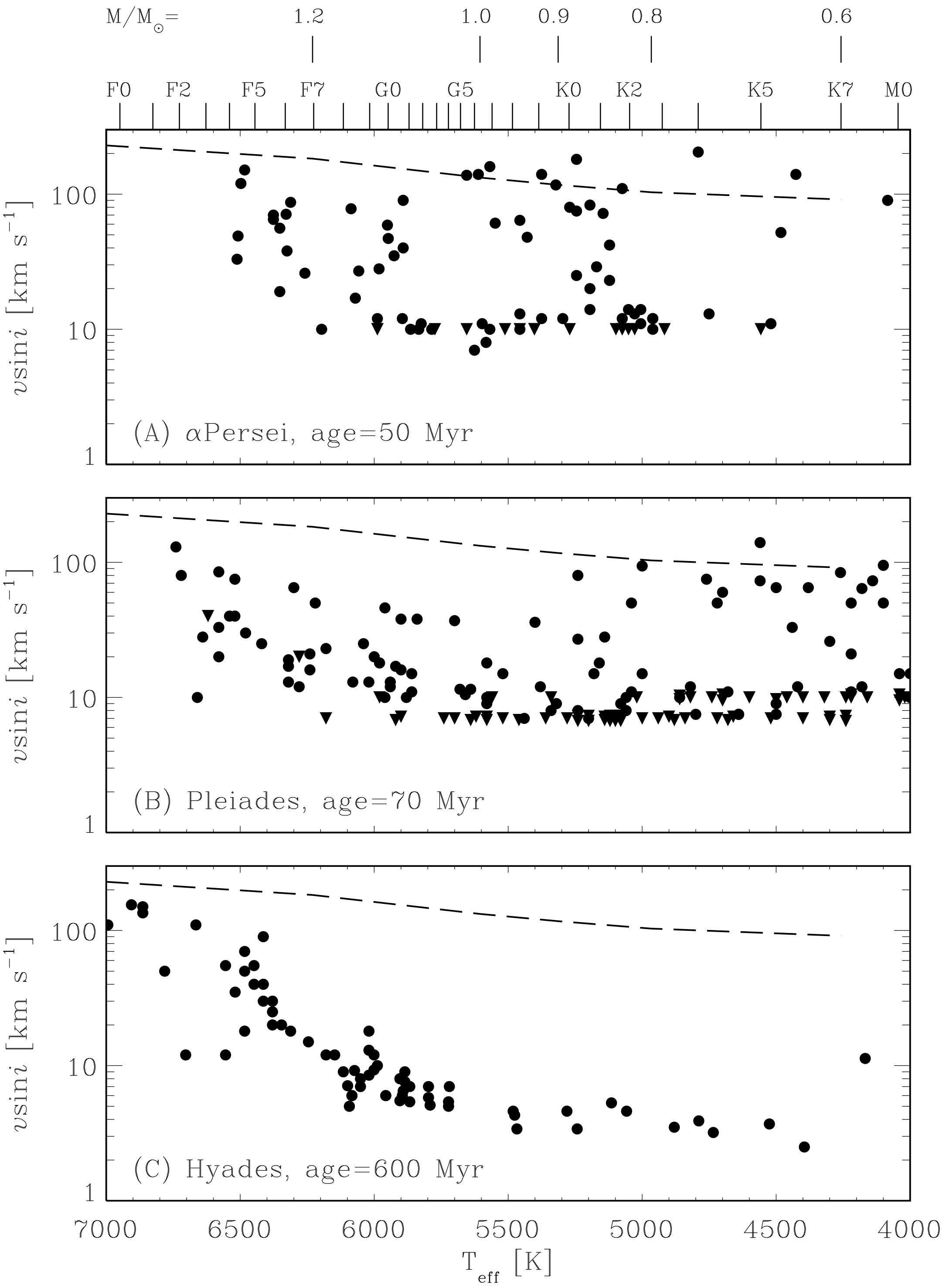

Figure 1.4: Observed rotation rates as a function of effective temperature for three young open clusters. Triangles are upper limits. The correspondence between spectral-types, mass and effective temperature is strictly valid only on the ZAMS. The dashed line corresponds to Kraft's relation (eq. [1.2]). Data courtesy of D. Soderblom.

- Rapid spin-down of the faster rotators occurs between the ages of the αPersei and Pleiades clusters; taken at face value, this implies a spin-down timescale of order $\sim 20\,\mathrm{Myr}$.
- Early main-sequence spin-down occurs more rapidly in G-stars than it does in K-stars.
- By the Hyades age ($\sim 600\,\mathrm{Myr}$), rotation rates have converged at all $T_{\mathrm{eff}} \gtrsim 7000\,\mathrm{K}$, in the sense that the rotation rate distribution at a given T_{eff} is well represented by a δ-function.

These, together with the helioseismic inferences discussed in the following chapter, provide key observational constraints on the rotational evolution models for the Sun that will occupy us in chapter 5[3].

1.2 Structural evolution and rotation

1.2.1 Angular momentum and moments of inertia

The total angular momentum content J of a spherically symmetric mass distribution of radius R rotating with angular velocity $\Omega(r, \theta)$ about a symmetry axis passing through the origin is[4]:

$$J = 2\pi \int_0^\pi \int_0^R \rho(r)\Omega(r,\theta) r^4 \sin^3\theta \mathrm{d}r\mathrm{d}\theta \tag{1.3}$$

in the usual spherical polar coordinates (r, θ, ϕ). For rigid rotation, $\Omega(r, \theta) \to \Omega$, this simplifies to

$$J = \Omega \left[\frac{8\pi}{3} \int_0^R \rho(r) r^4 \mathrm{d}r \right] . \tag{1.4}$$

The quantity within square brackets on the RHS of eq. (1.4) is the moment of inertia I of the mass distribution. For constant density, $I = (2/5)MR^2$, where M is the total mass of the sphere. Consider now a situation where the mass distribution is in a state of contraction or expansion, i.e., $R \to R(t)$ and $\rho(r) \to \rho(r,t)$, so that $I \to I(t)$. In the absence of an externally applied torque, and assuming that rigid rotation prevails, angular momentum conservation requires that

$$\Omega(t) = \Omega_0 \left(\frac{I_0}{I(t)} \right) , \tag{1.5}$$

[3] The use of these constraints relies implicitly on one very essential assumption. Can you figure out what it is?

[4] How can the internal mass distribution be spherically symmetric in the presence of rotation? The centrifugal force does not act in the radial direction, but rather in a direction perpendicular to the rotation axis. Do you think eq. (1.3) actually makes sense? Try to come up with a dimensional number that would allow you to estimate the regime under which this makes any sense.

where Ω_0 and I_0 are the rotation rate and moment of inertia of the star at some fiducial reference time. In general a star's moment of inertia will vary throughout its evolution both because of variations in the star's radius, and because of variations in the internal mass distribution [i.e., the $\rho(r,t)$ profile], leading to variations in its observed (surface) rotation rate. Consequently, before we can do anything with eq. (1.5) we need a structural evolutionary sequence for a $1\,M_\odot$ star.

1.2.2 Solar structure and evolution

The equations of solar/stellar structure represent the steady-state ($\partial/\partial t = 0$), static ($\mathbf{U} = 0$), unmagnetized ($\mathbf{B} = 0$) version of the equations of magnetohydrodynamics encountered in part I of the course. Under the assumption of spherical symmetry ($\partial/\partial\theta = \partial/\partial\phi = 0$), the remaining r-component of the equation of motion reduces to the familiar statement of hydrostatic equilibrium:

$$\frac{\mathrm{d}p}{\mathrm{d}r} = -\rho\frac{Gm(r)}{r^2}, \tag{1.6a}$$

where $m(r)$ is the mass contained within a spherical shell of radius r. The continuity equation can be expressed as

$$\frac{\mathrm{d}m}{\mathrm{d}r} = 4\pi\rho r^2. \tag{1.6b}$$

The energy equation becomes

$$\nabla\cdot(\mathcal{F}_r + \mathcal{F}_c) - \rho\epsilon_{\mathrm{nuc}} = 0, \tag{1.6c}$$

where ϵ_{nuc} (> 0) is the energy per unit mass liberated by nuclear reactions, in general a function of the local temperature, density, and chemical composition. The quantities $\mathcal{F}_r$ and $\mathcal{F}_c$ are the radiative and convective fluxes, which can be expressed in terms of other thermodynamical quantities and their derivatives. Equations (1.6) must be complemented with a suitable equation of state, tables of opacities and nuclear reaction rates, chemical composition, and a grid of model atmospheres for implementing the upper boundary conditions. In practice ϵ_{nuc} is a slowly varying function of time, because of changes in chemical composition brought about by nuclear burning. For evolutionary phases of interest here the corresponding timescales are much longer than other dynamical timescales, so that to a good degree of approximation stellar evolution on and near the main sequence is well approximated by a sequence of static models.

Good references to the art of solar/stellar structure and evolution computations are listed in the bibliography at the end of this chapter. For our present purposes, we shall simply consider the results of such calculations, namely a solar model. By this we mean a $1\,M_\odot$ model of solar chemical composition left to evolve for 4.5Gyr. Figure 1.5 illustrates, as a function of depth, structural, thermodynamical and chemical properties of such a model. For future reference, Table 1.1 lists the structural and thermodynamical quantities, for radial increments of about $0.03\,R_\odot$[5]. Note that the outermost portion of the convective envelope ($r/R_\odot > 0.92$) is not accurately represented in this interior model.

An important structural characteristic of solar-type stars on and near the main-sequence is the existence of an *outer convective envelope*, where energy transport occurs primarily via large-scale, turbulent fluid motions, rather than by radiative diffusion. The seventh column in Table 1.1 is the quantity

$$S = \left(1 - \frac{\nabla_{\rm ad}}{\nabla_{\rm rad}}\right) \tag{1.7}$$

where $\nabla_{\rm ad}$ and $\nabla_{\rm rad}$ are the adiabatic and radiative temperature gradient, respectively. The quantity S is negative in radiative zones, and positive in convective regions.

In the present-day Sun the convective envelope covers the interval $0.72 \lesssim r/R_\odot \lesssim 0.999$, contains $\sim 1\%$ of the total mass and accounts for $\sim 10\%$ of the total moment of inertia.

Figure 1.5 represents a single "snapshot" of the Sun, albeit an important one. To make use of eq. (1.5) we need a sequence of such models spanning the evolution of the Sun on and near the main-sequence. Figure 1.6 shows evolutionary tracks and Figure 1.7 the corresponding time variations of the moments of inertia for stars of various masses, from the pre-main-sequence all the way to the base of the giant branch. In themselves, variations in I are expected to lead to some level of spin-*up* on the pre-main sequence, and spin-*down* on the post-main sequence. On the main sequence I is essentially constant, as the small increase in radius ($\sim 15\%$ for $1\,M_\odot$) is almost exactly compensated by the increase in central condensation brought about by the conversion of Hydrogen to Helium in the inner core.

From these structural evolutionary considerations, one would conclude that solar-type stars should spin up on their way to the ZAMS, retain whatever rotation rate was produced by this spin up phase throughout their main-sequence lifetime, and finally spin-down once they leave the main-sequence on their way to the giant branch. The observations reviewed in §1.1 clearly indicate that this is not what happens in reality. Where did we go wrong?

1.3 The Skumanich $t^{-1/2}$ relation

The discrepancy between the expectations constructed on the basis of structural considerations alone and the observed rotational evolution of solar-type can only be resolved by allowing for *angular momentum loss* during the main-sequence evolutionary phase. It turns out that in the first part of this course we have already studied a promising physical mechanism that leads precisely to this: angular momentum loss in a rotating, magnetized, thermally-driven transsonic wind. Even better, in the Weber-Davis solution of §I.4.3 we even have at our disposal a *quantitative* model that allows us to *compute* the rate of angular momentum loss as a

[5] This model is available electronically, with better depth resolution, on the course Web Page: `http://www.hao.ucar.edu/public/education/astr7500.html`.

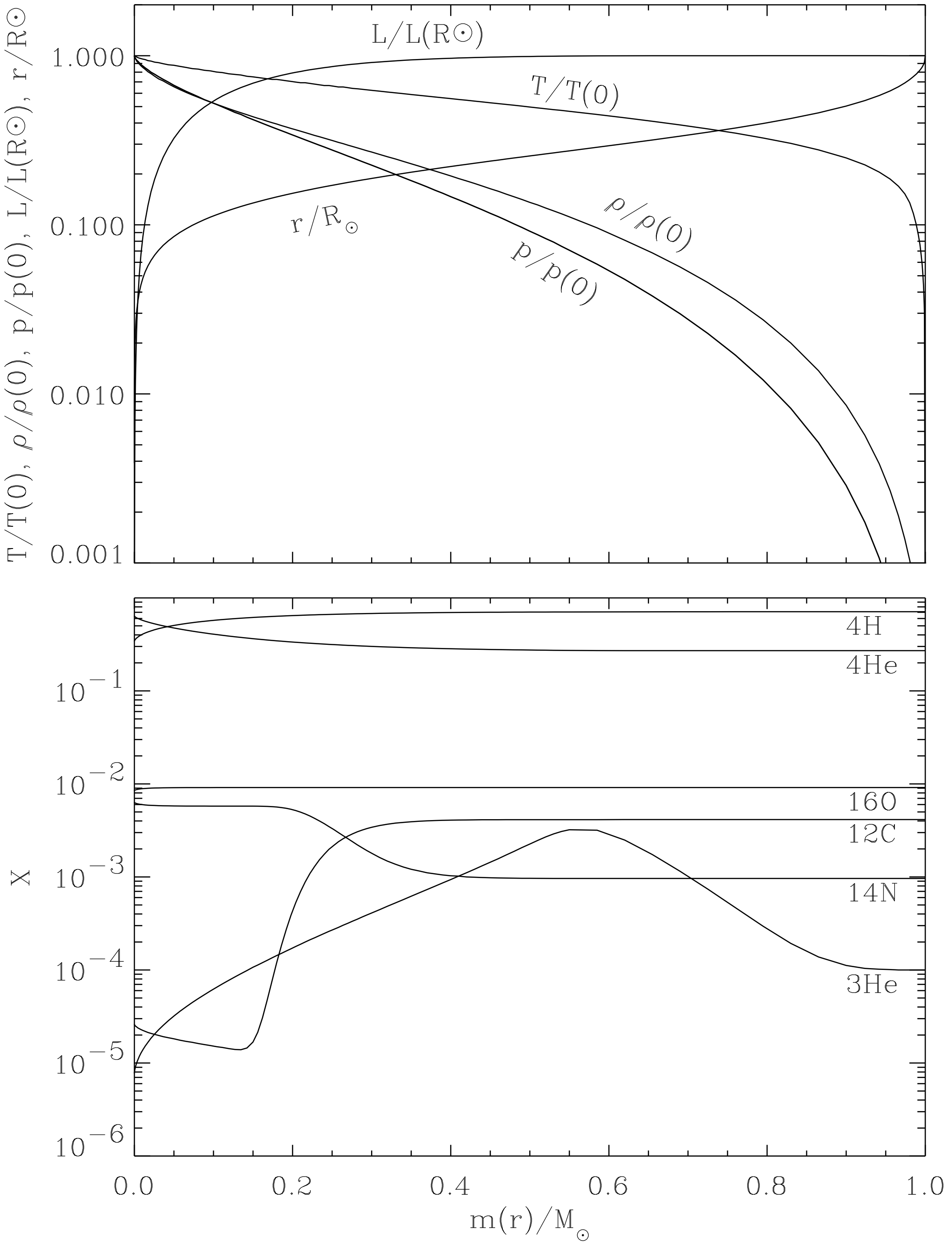

Figure 1.5: A standard non-rotating solar model, courtesy of J.N. Bahcall. This model has central temperature $T(0) = 1.56 \times 10^7\,\mathrm{K}$ central density $\rho(0) = 148\,\mathrm{g\,cm^{-3}}$, and central pressure $p(0) = 2.29 \times 10^{17}\,\mathrm{erg\ cm^{-3}}$.

Table 1.1: Standard solar model

$m(r)/M_\odot$	$r/R_\odot$	$T[K]$	$\rho[\mathrm{g\,cm^{-3}}]$	p [erg $\mathrm{cm^{-3}}$]	$L(r)/L_\odot$	Q	$X(H)$
0.0000	0.0000	1.56E+7	1.48E+2	2.29E+17	0.000	-0.127	0.3411
0.0008	0.0197	1.55E+7	1.44E+2	2.24E+17	0.007	-0.134	0.3533
0.0063	0.0400	1.51E+7	1.32E+2	2.08E+17	0.051	-0.150	0.3889
0.0211	0.0616	1.45E+7	1.16E+2	1.83E+17	0.157	-0.171	0.4418
0.0429	0.0804	1.38E+7	1.01E+2	1.60E+17	0.287	-0.188	0.4923
0.0808	0.1033	1.30E+7	8.40E+1	1.31E+17	0.466	-0.208	0.5506
0.1192	0.1217	1.22E+7	7.20E+1	1.10E+17	0.603	-0.228	0.5912
0.1620	0.1393	1.15E+7	6.20E+1	9.12E+16	0.716	-0.254	0.6235
0.2160	0.1594	1.08E+7	5.20E+1	7.29E+16	0.817	-0.312	0.6519
0.2760	0.1801	1.00E+7	4.30E+1	5.70E+16	0.891	-0.399	0.6729
0.3400	0.2014	9.31E+6	3.51E+1	4.36E+16	0.939	-0.488	0.6872
0.4000	0.2212	8.70E+6	2.88E+1	3.36E+16	0.966	-0.580	0.6956
0.4600	0.2415	8.13E+6	2.34E+1	2.56E+16	0.983	-0.644	0.7010
0.4700	0.2450	8.04E+6	2.25E+1	2.44E+16	0.985	-0.658	0.7016
0.5100	0.2591	7.67E+6	1.94E+1	2.00E+16	0.992	-0.707	0.7037
0.5200	0.2628	7.58E+6	1.86E+1	1.90E+16	0.993	-0.721	0.7041
0.5850	0.2876	7.01E+6	1.42E+1	1.34E+16	0.998	-0.815	0.7062
0.6550	0.3176	6.39E+6	1.01E+1	8.69E+15	1.000	-0.896	0.7081
0.6900	0.3344	6.08E+6	8.34E+0	6.82E+15	1.000	-0.946	0.7087
0.7250	0.3529	5.76E+6	6.75E+0	5.22E+15	1.000	-0.996	0.7091
0.7600	0.3737	5.44E+6	5.32E+0	3.88E+15	1.000	-1.029	0.7093
0.7950	0.3975	5.09E+6	4.06E+0	2.77E+15	1.001	-1.065	0.7095
0.8300	0.4255	4.73E+6	2.96E+0	1.88E+15	1.001	-1.101	0.7096
0.8650	0.4597	4.33E+6	2.03E+0	1.18E+15	1.001	-1.111	0.7097
0.9000	0.5038	3.88E+6	1.27E+0	6.59E+14	1.001	-1.093	0.7097
0.9237	0.5431	3.53E+6	8.42E-1	3.98E+14	1.001	-1.048	0.7097
0.9418	0.5818	3.20E+6	5.72E-1	2.45E+14	1.001	-0.974	0.7097
0.9556	0.6195	2.91E+6	3.96E-1	1.55E+14	1.000	-0.874	0.7097
0.9662	0.6559	2.64E+6	2.81E-1	9.94E+13	1.000	-0.700	0.7097
0.9742	0.6906	2.38E+6	2.05E-1	6.53E+13	1.000	-0.499	0.7097
0.9803	0.7230	2.11E+6	1.54E-1	4.37E+13	1.000	-0.167	0.7097
0.9850	0.7523	1.82E+6	1.22E-1	2.98E+13	1.000	0.285	0.7097
0.9886	0.7783	1.57E+6	9.81E-2	2.06E+13	1.000	0.556	0.7097
0.9913	0.8015	1.36E+6	7.92E-2	1.44E+13	1.000	0.708	0.7097
0.9933	0.8221	1.19E+6	6.42E-2	1.01E+13	1.000	0.801	0.7097
0.9949	0.8406	1.03E+6	5.22E-2	7.19E+12	1.000	0.867	0.7097
0.9961	0.8573	9.04E+5	4.26E-2	5.12E+12	1.000	0.910	0.7097
0.9970	0.8722	7.91E+5	3.48E-2	3.65E+12	1.000	0.937	0.7097
0.9978	0.8858	6.92E+5	2.84E-2	2.60E+12	1.000	0.956	0.7097
0.9983	0.8981	6.04E+5	2.31E-2	1.84E+12	1.000	0.969	0.7097
0.9987	0.9093	5.25E+5	1.87E-2	1.29E+12	1.000	0.978	0.7097
0.9990	0.9197	4.54E+5	1.50E-2	8.95E+11	1.000	0.984	0.7097
1.0000	1.0000	5.77E+3	0.00E+0	0.00E+00	1.000	-1.000	0.7097

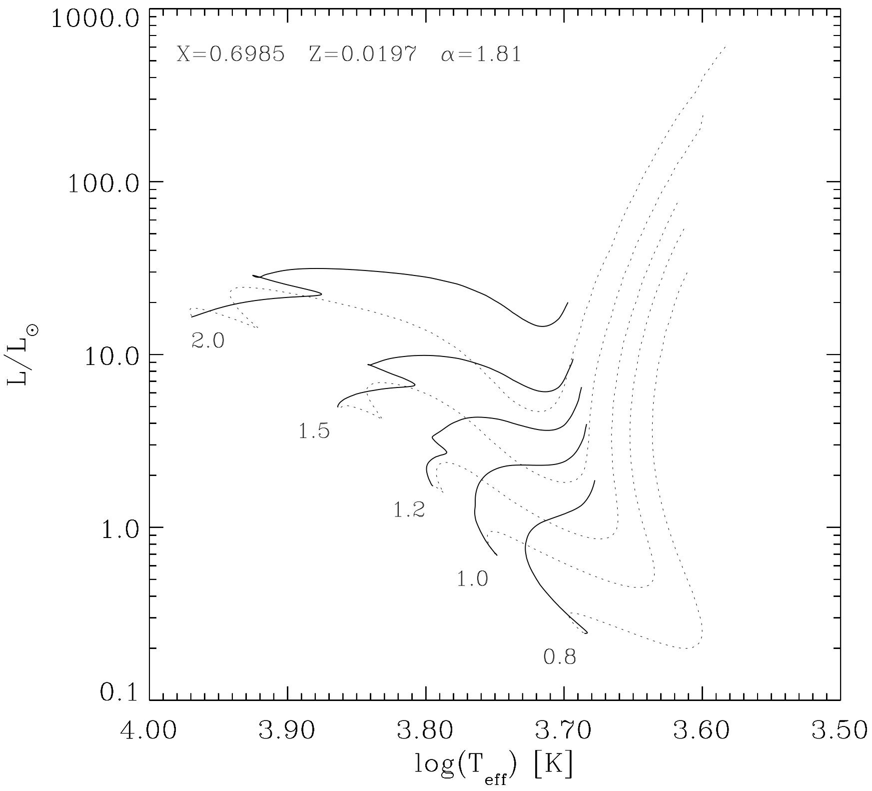

Figure 1.6: Evolutionary tracks for solar-type stars. The dotted portion of the tracks corresponds to the pre-main sequence. The solid portion begins on the Zero-Age Main-Sequence (ZAMS), and extends to the base of the giant branch. Tracks are labeled according to stellar mass, in units of $M_\odot$. Tracks courtesy of D.A. Vandenberg.

function of the wind parameters. The following little derivation makes extensive use of results from chapter 4 of part I; rather than reproduce material presented therein, we will write, e.g., eq. (I.4.20) to refer to equation (4.20) in part I, with a similar notation used for Figures.

For our present purposes, the most important result obtained in chapter I.4 is eq. (I.4.35), stating that the total angular momentum per unit mass L carried away by the wind is equal to that which would be carried away by an unmagnetized wind remaining in a state of strict co-rotation out to the Alfvén radius r_A:

$$L = \Omega r_A^2 \tag{1.8}$$

To obtain the net angular momentum loss, all we need to do is multiply L by the mass flux. But eq. (1.8) is valid only in the equatorial plane, where the WD solution was obtained. We need to construct an equivalent expression taking into account the whole sphere. This is not simply 4π times eq. (1.8), or something like

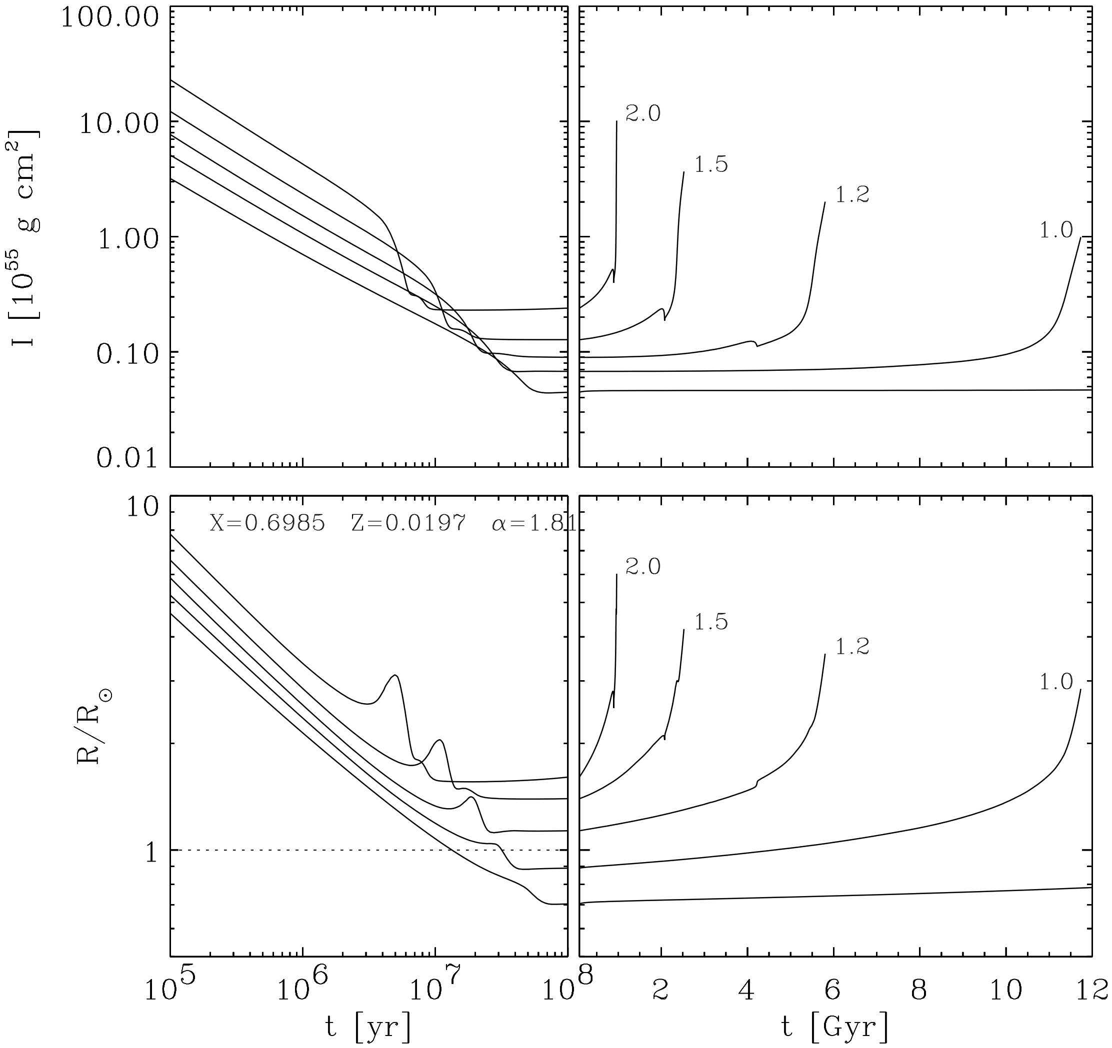

Figure 1.7: Time variation of the moments of inertia, along the evolutionary tracks of Figure 1.7. Note how the time of arrival on the ZAMS (corresponding to the beginning of the constant-I phase) varies with stellar mass.

that. Remember that angular momentum is extracted when fluid elements are displaced in a direction *perpendicular* to the rotation axis. A mass flux along the polar axis, no matter how large, carries away no angular momentum, whether it is magnetically coupled or not. We can stretch the WD model to the whole sphere by assuming that the total angular momentum per unit mass carried away by the wind is equal to that of a *spherical shell* corotating out to r_A; this means replacing

(1.8) by

$$L_{\rm sph} = \frac{2}{3}\Omega r_A^2 \tag{1.9}$$

where the factor 2/3 come from the moment of inertia calculation. The rate of angular momentum loss is then

$$\frac{\partial J}{\partial t} = \dot{\rm M} \times L_{\rm sph} = -4\pi\rho_A r_A^2 v_{rA}\left(\frac{2}{3}\Omega r_A^2\right). \tag{1.10}$$

Now, at the Alfvén radius we have (by definition) $v_{rA} = A_{rA}$. Furthermore, by virtue of eqs. (I.4.30) we have

$$B_{rA}^2 = 4\pi\rho_A A_{rA}^2, \tag{1.11}$$

so that we can then rewrite eq. (1.10) as

$$\frac{\partial J}{\partial t} = -\frac{2}{3}\frac{(r_A B_{rA})^2}{A_{rA}}\Omega r_A^2. \tag{1.12}$$

Conservation of magnetic flux (Equation [I.4.22]) also allows us to write $r_0^2 B_{r0} = r_A^2 B_{rA}$. Equation (1.12) becomes

$$\frac{\partial J}{\partial t} = -\frac{2}{3}B_0^2 r_0^4 \Omega A_{rA}^{-1}. \tag{1.13}$$

Returning to Fig. I.4.4, one sees that in the limit where the centrifugal and magnetic contributions to the net acceleration of the wind are much smaller than the thermal contribution (a situation we will refer to as “mostly thermally-driven”), $A_{rA} \simeq c_s$ within a factor of two or so. *For a given coronal temperature*, the angular momentum loss rate is then only a function of the rotation rate and surface magnetic field[6]. Both of these are known for the present day Sun. What about the “young” Sun? Observations of solar analogs in young clusters, as reviewed in §1.1, indicate that the Sun may well have been rotating anywhere between 5 and 100 times its present rate upon its arrival on the ZAMS. The various proxies of *magnetic activity* in these stars also suggest that young, rapidly rotating solar-type stars have large magnetic fields, and that these fields, at a given spectral

[6] Since the heating of the corona is very likely due to some form of magnetoacoustic heating, or whatever, related to magnetic activity, we should perhaps assume that the coronal temperature is also some function of B_{r0} (and probably Ω) This would make c_{s0} an implicit function of B_{r0} and Ω, which would be nasty.

type, tend to be stronger the higher the rotation rate[7]. So the young Sun rotated faster, but was then also losing much more angular momentum.

We will see in part IV of this course that there are reasonably good reasons to expect that the strength of a dynamo-generated surface magnetic field should increase with increasing rotation. In fact, one of the first semi-solid class of dynamo models, the so-called $\alpha\omega$ dynamos, predicted $B_0 \propto \Omega$. Assuming that this is indeed the case (but keeping in mind that it may well not be), and for a time-independent moment of inertia, eq. (1.13) can be rewritten as

$$\frac{\mathrm{d}\Omega}{\mathrm{d}t} \propto -\Omega^3. \tag{1.14}$$

This integrates [8] to

$$\frac{1}{\Omega^2(t)} - \frac{1}{\Omega^2(t_0)} \propto t - t_0, \tag{1.15}$$

which, in the asymptotic limit $t \gg t_0$, $\Omega \ll \Omega(t_0)$ becomes

$$\Omega(t) \propto t^{-1/2}. \tag{1.16}$$

which, wouldn't you know, is precisely the power law relationship inferred by Skumanich (cf. Fig. 1.3 above) There is something important that will later come back to haunt us about eq. (1.14). Because of the positive and relatively high index of the power law, it can be expected that faster rotators will spin down significantly faster than slow rotators. Therefore, if we start with a wide distribution of rotation rates on the ZAMS, magnetic braking leads naturally to a convergence of rotation rates at later epochs, erasing any "memory" of the initial condition.

At any rate, eq. (1.16) represent our first "model" for the main-sequence rotational evolution of solar-type stars. Using eq. (1.16) to extrapolate backward over the Sun's evolution on the main-sequence leads to equatorial rotational velocities in excess of $100\,\mathrm{km\,s^{-1}}$ on the ZAMS ($t_{\mathrm{ZAMS}} \sim 4 \times 10^7$ yr for a standard solar model). This fits rather nicely with the fastest rotation rates observed for solar analogs in the α-Persei cluster (Fig. 1.4). So it looks like we're in business, yippee

---

[7] The situation is actually quite a bit more subtle. Solar observations indicate that the Sun's magnetic field is not distributed homogeneously on its surface, but pierces the latter in discrete (active) regions. In these regions the magnetic field is very strong (in the kG range), but elsewhere it is near the detection limit. It is only in the surface-averaged sense that the Sun is believed to have a surface magnetic field strength of the order of a few Gauss. When we observe "stronger" magnetic fields in young solar analogs, we cannot tell whether we are seeing intrinsically stronger fields, or if a larger fraction of the star's surface is magnetically active with the same peak field strength as in the Sun.

[8] Do it.

hurraah yahooo[9]. So let us then proceed with our first attempt at addressing the observational constraints listed earlier.

1.4 The rotation of late-type stars on and near the ZAMS

In this section we use the results gathered so far in this chapter to look into two important observational constraints: the presence of very fast rotators on the ZAMS, and the rapid spin-down observed to occur between the ages of αPersei and the Pleiades amongst the faster rotators. The convergence of rotation rates by the Hyades age is left as a problem (1.2) at the end of this chapter.

1.4.1 Pre-main sequence spin-up

Our first task is to see if purely structural considerations can account for the observed ZAMS rotation rates. This requires a knowledge of the initial angular momentum content of those stars in their pre-main sequence phase. There exists rotational data for a class of pre-main sequence stars known as the T-Tauri stars, which have ages in the range 10^6—10^7 yr and a bimodal distribution of rotation periods ($P \equiv 2\pi/\Omega$), with the slowly rotating group having $P \sim 7.6 \pm 2.1$ days, and the faster rotating group $P \sim 4.1 \pm 1.7$ days. One can read off Figure 1.7 approximate moments of inertia and radii for these objects, and then use eq. (1.5) to infer approximate equatorial rotational velocity values on the ZAMS:

$$v_{\rm eq}({\rm ZAMS}) \sim 50\,{\rm km\,s^{-1}}, \qquad [\text{slow group}] \tag{1.17a}$$

$$v_{\rm eq}({\rm ZAMS}) \sim 150\,{\rm km\,s^{-1}}, \qquad [\text{fast group}] \tag{1.17b}$$

Note that this calculation relies on the following ingredients: (1) moments of inertia and ages for TTauri stars; these must be estimated from the position of TTauri stars in an HR diagram with respect to structural evolutionary tracks. This is tricky, among other things, because TTauri live in a region of the HR diagram where evolutionary tracks run parallel and close to one another; (2) assumption of internal solid-body rotation throughout pre-main sequence evolution. This may well be valid for TTauri stars, but certainly not during the last ~ 2 Myr of pre-main sequence evolution for a $1\,M_\odot$ star; (3) no angular momentum loss on the pre-main sequence.

While it is comforting that pre-main sequence spin up seems to be able to account for the fast rotators observed in αPersei, it suggests that the making of slow αPersei rotators may require significant pre-main sequence angular momentum loss. Although many plausible scenarii have been proposed, this remains a hot research topic in rotational evolution. For those interested, the bibliography at the end of this chapter lists a few good entry points into the technical literature.

---

[9] Make a list of the various assumptions having entered our derivation of eq. (1.16). How reasonable are they? Which of the assumption do you feel is the least reasonable? The most reasonable?

1.4.2 Early main-sequence spin-down

Our second task is to account for the swift spin down of rapidly rotating solar-type stars between the ages of αPersei and the Pleiades (cf. Figure 1.4), which implies a spin down timescale of the order of the age difference between these two clusters, i.e. $\sim 20\,$Myr. This is a powerful observational constraint: is such a short spin down timescale compatible with the angular momentum loss rates predicted by the WD model? The WD model provides an estimate for the torque applied to the star; the evolutionary tracks give us moments of inertia. Under the assumption of internal solid-body rotation, one can readily calculate an approximate spindown timescale τ_J:

$$\tau_J = \frac{1}{\Omega I}\left(\frac{\mathrm{d}J}{\mathrm{d}t}\right)^{-1} \tag{1.18}$$

The third and fourth columns of Table 1.2 below list ZAMS stellar moments of inertia (I_*) and spin-down timescales ($\tau_{J,*}$) for solar-type stars of various masses. The torque is computed assuming that in all cases the ZAMS star has a rotation period of one day, an average surface magnetic field strength of 50 G, and is surrounded by a $1.5 \times 10^6\,$K corona. Again, you should keep in mind that these represent a plausible set of assumptions, but we don't really know. In particular, it may well be that the coronal temperature is a complex function of the stellar surface parameters, including the magnetic field strength.

Table 1.2

ZAMS spindown timescales for late-type stars

$M_*/M_\odot$	$R_*/R_\odot$	I_* [10^{53}g cm^2]	$\tau_{J,*}$ [Myr]	$I_{\rm CE}$ [10^{53}g cm^2]	$\tau_{J,CE}$ [Myr]
0.8	0.703	4.41	810.	1.025	188.
0.9	0.784	5.50	604.	0.979	107.
1.0	0.882	6.75	396.	0.833	48.9
1.2	1.131	9.02	133.	0.139	2.05

It is clear from the fourth column of Table 1.2 that the estimated spin-down timescale for the star as a whole are in the range 10^8—$10^9\,$yr, which is too large by over an order of magnitude[10]. The calculation of $\tau_{J,*}$, however, used the moment of inertia of the stars as a whole in eq. (1.18), which implies that the star is decelerated as a solid-body.

[10] Something potentially weird should attract your attention upon scrutiny of Table 1.2: although the moments of inertia are increasing with increasing stellar mass (which makes perfect sense in view of eq. [1.3]), the spin-down timescale $\tau_{J,*}$ actually *decreases* with increasing $M/M_\odot$. How do you explain this?

We will see in the following chapters that there are good reasons to believe that, *in terms of its response to an externally applied torque*, the convective envelope indeed behaves like a solid body. The situation is not so clear for the radiative core. In chapter 3 we will estimate internal angular momentum redistribution timescales in the radiative core for a variety of physical mechanisms, and find that these timescale may well be comparable to the spin-down timescale. This suggests that the wind-mediated torque may well only decelerate the convective envelope, with the radiative core retaining most of it angular momentum during the initial spin-down phase. The two rightmost columns in Table 1.2 list the moments of inertia of the envelope only ($I_{\rm CE}$), and the corresponding spin-down timescale ($\tau_{J,CE}$) computed via eq. (1.18) with $I \equiv I_{\rm CE}$. This time the spin-down timescales are a few 10^7 yr for $M/M_\odot = 1$, which is good enough given the order-of-magnitude nature of the calculation.

We thus conclude that fast enough spin-down following the arrival on the ZAMS requires some degree of *core-envelope decoupling*. This clearly says something about the efficacy of whatver physical mechanism is responsible for the redistribution of angular momentum within the solar radiative interior. We will revisit this issue in greater depth in chapter 3.

Problems

(1.1) Compute the moment of inertia of the solar model listed in Table 1.1. Rather than typing in the numbers, you are encouraged to obtain the data from the course's Web Page:

`http://www.hao.ucar.edu/public/education/astr7500.html`

From the top of the main Page, click on Problems: software and data, find the appropriate subsection and follow the instructions given there. Then,

(a) Assuming solid-body rotation, calculate the net moment of inertia for: (1) the full model, and (2) the convective envelope.

(b) Then, compute (and plot) the angular momentum *per unit mass* as a function of depth in the model. Where is most of the angular momentum stored in a rigidly rotating star?

(c) Based on your results in (b), by how much would you need to spin up the radiative core to double the total angular momentum content of the Sun?

(1.2) Calculate the proportionality constant in eq. (1.16). Calculate (and plot) the predicted rotational evolution of stars of masses 0.8, 0.9, 1.0 and 1.2 $M_\odot$, starting from ZAMS rotation rates 5, 10, 50 and 100 times that of the present-day Sun. Assume a fixed coronal temperature $T = 1.5 \times 10^6$ K. Can you reproduce the observed convergence of rotation rates by the Hyades age?

(1.3) This problem lets you relax some —but not all— of the assumptions involved in the derivation of the Skumanich relation. Your first step consists in going to the course Web Page, as described above, and grabbing the required software for problem II.1.3, as described in the instructions. Essentially, the software is a black box FORTRAN-77 subroutine that allows you to calculate $\mathrm{d}J/\mathrm{d}t$ as predicted by the WD model, for a given rotation rate Ω and surface magnetic field strength $\mathbf{B}_{\rm surf}$. Once you have the software do the following:

(a) Assuming as before $\mathrm{B}_{\rm surf} \propto \Omega$, plot the angular momentum loss rate predicted by the WD model against rotation rate, and compare the resulting curve with the prediction of eq. (1.14). You may assume internal solid-body rotation.

(b) Write down an ODE describing the time variation of total angular momentum, and use the WD interpolation subroutine to integrate this ODE for a rigidly rotating $1\,M_\odot$ model starting on the ZAMS at 5, 10, and 50 times the present-day solar rotation rate. Compare the evolution of surface rotation to that predicted by the Skumanich relation. You may assume a constant moment of inertia on the main-sequence.

(c) Explore the effects of *dynamo saturation*. Specifically, repeat step (b) above, but this time assume $\mathrm{B}_{\rm surf} \propto \Omega$ up to a critical rotation rate ($\Omega_{\rm crit}$, say), and $\mathrm{B}_{\rm surf}$=constant for $\Omega > \Omega_{\rm crit}$. Compare the resulting curves of surface rotation vs time with those produced in (b), for a few different values of $\Omega_{\rm crit}$ in the range $5 \leq \Omega_{\rm crit} \leq 20$.

Bibliography

Galileo's thoughts on solar rotation and the nature of sunspots, first published in his so-called *Letters on Solar Spots*, are still well worth reading today. A good abridged English translation is given found in

Drake, S. (trans.) 1957, *Ideas and Opinions of Galileo*, New York: Doubleday.

A thorough discussion of the debates over the early sunspots observations can be found in

Mitchell, W.M. 1916, Popular Astronomy, 24, 22-ff.

Rumors are afloat that A. Van Helden is right now putting the finishing touches on a book dedicated to the history of early sunspot telescopic observations, with particular emphasis on the Galileo-Scheiner controversies. Other historical references cited in §1.1 are to:

Abney, W. de W. 1877, MNRAS, 37, 278,
Carrington, R.C. 1863, *Observations of the Spots on the Sun*, London: Williams and Norgate,
Schlesinger, F. 1909, Pub. Allegheny Obs., 1, 123,

Vogel, H.C. 1872, Astron. Nachr., 78, 248,
Elvey, C.T. 1929, ApJ, 70, 141.

The following are two early reviews, still well worth reading:

Struve, O. 1945, Popular Astronomy, 53, 201-ff,
Kraft, R.P. 1970, in *Spectroscopic Astrophysics*, ed. G.H. Herbig (Berkeley: University of California Press), p. 385.

Analysis and results of the Mt. Wilson sunspot survey are reported in

Howard, R., Gilman, P., & Gilman, P.I. 1984, ApJ, 283, 373,
Howard, R. 1984, ARA&A, 22, 131.

Equation (1.1d), for Doppler measurements of the solar surface rotation, is taken from

Howard, R., & Harvey, J. 1970, SolP, 12, 23.

The Skumanich "$t^{-1/2}$ relation" was first inferred observationally:

Skumanich, A. 1972, ApJ, 171, 565,

with a theoretical derivation in the context of $\alpha\omega$ dynamo theory due to:

Durney, B.R. 1972, in *Solar Wind*, eds. C.P. Sonett, P.J. Coleman, & L.M. Wilcox (Washington: NASA Scientific and Technical Information Office), p. 282.

see also

Soderblom, D.R. 1983, ApJS, 53, 1
Soderblom, D.R., Stauffer, J.R., Hudon, J.D., & Jones, B.F. 1993, ApJS, 83, 315.
Soderblom, D.R., Stauffer, MacGregor, K.B., & Jones, B.F. 1993, ApJ, 409, 624.

The notion that magnetized outflows from stars can lead to angular momentum loss can be traced to

Schatzman, E. 1959, in IAU Symp. 10, *The Hertzsprung-Russell Diagram*, ed. J.L. Greestein, 129.
Schatzman, E. 1962, *Ann. Astrophys.*, **25**, 18.

although Schatzman's model itself has not sustained the test of time. The first detection of very rapidly rotating solar-type stars in solar-type Pleiades stars is due to

Van Leeuwen, F., & Alphenaar, P. 1982, ESO Messenger, 28, 15.

The need for core-envelope decoupling to account for the rapid spin-down of solar type stars following their arrival on the ZAMS was first put forth by

Stauffer, J.R., & Hartmann, L.W. 1986, ApJ, 318, 337

The study of rotational evolution of solar-type stars has received renewed interest in recent years. The following two volumes contain many reviews of interest:

Catalano, S., & Stauffer, J.R. (eds.) 1991, *Angular Momentum Evolution of Young Stars* (Dordrecht: Kluwer),

Caillault, J.-P. (ed.) 1994, *Eight Cambridge Workshop on Cool Stars, Stellar Systems, and the Sun*, ASP Conference Series vol. 64.

In Catalano & Stauffer see in particular the papers by Collier Cameron, Jianke & Mestel (p. 297), MacGregor (p. 315), Soderblom (p. 151), and Stauffer (p. 117); in Caillault see the papers by Bouvier (p. 151), Stauffer (p. 163), MacGregor & Charbonneau (p. 174), and Cameron, Campbell & Quaintrell (p. 187). Good texts on stellar structure and evolution are

Clayton, D.D. 1968, *Principles of Stellar Evolution and Nucleosynthesis*, University of Chicago Press.

Hansen, C., & Kawaler, S.D. 1994, *Stellar Interiors*, Springer.

Kippenhahn, R., & Weigert, A. 1990, *Stellar Structure and Evolution*, New York: Springer, chap. 42.

The solar model of Figure 1.5 and Table 1.1 is discussed in

Bahcall, J.N., & Ulrich, R.K. 1988, Rev. Mod. Phys., 60, 297.

Bahcall, J.N. 1989, *Neutrino Astrophysics*, Cambridge University Press, chap. 4.

2. HELIOSEISMOLOGY

3. THE SOLAR RADIATIVE CORE

"So, so you think you can tell / Heaven from Hell? / Blue sky from pain? / Can you tell a green field / From a cold steel rail / A smile from a veil? / Do you think you can tell?"

Pink Floyd
Wish You Were Here (1975)

We saw in §1.4 that depending on whether the wind-mediated torque applied to the solar surface decelerates the Sun as a whole or only its convective envelope, very different spin-down rates can result. While there appears to be little doubt that the envelope reacts to externally applied torques as a solid-body, this may not be the case in the radiative interior.

In this chapter we will be concerned with the response, on structural evolutionary timescales, of the solar radiative core to angular momentum loss in a wind. Specifically, we examine how the radiative core reacts to the buildup of a radial shear at the core-envelope interface, as a consequence of envelope spin-down. We begin by establishing some order-of-magnitude estimates for the importance of various potential internal angular momentum transport mechanisms (§3.1). We then consider the effects of ordinary microscopic viscosity (§3.2), followed by a general discussion of the effects of large-scale internal flows (§3.3). Finally, we discuss in detail two specific classes of models for the rotational evolution of the solar radiative interior (§§3.4 and 3.5).

Throughout the chapter we will enforce solid-body rotation and homogeneous chemical abundances in the convective envelope, usually by arbitrarily increasing the transport coefficients therein by many orders of magnitude. This can be justified on the grounds that turbulent convective motions redistribute angular momentum and chemical species on timescales far shorter than any other relevant timescales in the problem. Some theoretical justification this procedure will be provided in chapter 4.

3.1 Some order-of-magnitude estimates

There exist many potentially important players in the redistribution of angular momentum in the solar radiative interior. Broadly speaking these can be divided into three classes: (1) large-scale flows, (2) viscous-like transport, where this is meant to incorporate possible contributions of small-scale turbulent fluid motions, and (3) magnetic stresses[1]. The potential efficiency of these mechanisms can be estimated as follows. Working in spherical polar coordinates and under the assumption of axisymmetry, let us simply write down the ϕ-component of the equations of motion, including contributions from a large-scale meridional flow $\mathbf{U}_p$, effective viscosity $\nu_{\rm eff}$, and Lorentz Force:

$$\frac{\partial}{\partial t}(\rho\varpi^2\Omega) = -\rho\mathbf{U}_p\cdot\nabla(\varpi^2\Omega) + \nabla\cdot[\rho\varpi^2\nu_{\rm eff}\nabla\Omega] + \frac{1}{4\pi}\mathbf{B}_p\cdot\nabla(B_\phi\varpi), \tag{3.1}$$

where $\varpi \equiv r\sin\theta$. Of course, in practice this equation must be complemented with evolution equations for $\mathbf{U}_p$, $\mathbf{B}_p$, B_ϕ, and an expression for $\nu_{\rm eff}$. Instead, as a starting point for the following discussion, let us assume that $\mathbf{U}_p$, $\mathbf{B}_p$, and $\nu_{\rm eff}$ are known, and carry out a dimensional analysis of eq. (3.1). This means replacing $\partial/\partial t \to 1/\tau$, $\nabla \to 1/\ell$, and quantities such as ρ, $\mathbf{B}_p$ or $\nu_{\rm eff}$ by representative average values [2]. This leads to

$$\frac{1}{\tau} = \frac{1}{\tau_U} + \frac{1}{\tau_\nu} + \frac{\tau}{\tau_B^2}, \tag{3.2}$$

where we have defined the three timescales

$$\tau_U = \ell/|\mathbf{U}|, \tag{3.3a}$$

$$\tau_\nu = \ell^2/\nu_{\rm eff}, \tag{3.3a}$$

$$\tau_B = \ell/A_p, \tag{3.3a}$$

In eq. (3.3c) $A_p \equiv |\mathbf{B}_p|/\sqrt{4\pi\bar{\rho}}$ is the Alfvén speed based on the poloidal field strength, and $\bar{\rho}$ is some representative average value for the density. Note that eqs. (3.3) presuppose that there exists a single, suitable length scale ℓ that adequately characterizes the flow, magnetic field, and size of the system. Keeping in mind that eqs. (3.3) provide at most order-of-magnitude estimates, one can calculate the magnitude of the flow speed, effective viscosity and magnetic field required to independently bring about angular momentum transport over a length scale $\ell \sim R_\odot$ on a timescale $\tau \sim 1\,$Gyr. This exercise yields

$$|\mathbf{U}_p| \sim 10^{-6}\,\text{cm s}^{-1}, \tag{3.4a}$$

---

[1] Over the past few years considerable attention has been paid to the possible contributions of *gravity waves* to internal angular momentum redistribution; see for example Kumar & Quataert 1997, ApJ, 475, 143, and Zahn, Talon & Matias 1997, Å322320. However, the current state of theory and modeling is such that it cannot yet be discussed on par with the other mechanisms considered in this chapter. Maybe at the next iteration of this course...

[2] One quantity appearing in eq. (3.1) that requires a bit of extra work is the toroidal field B_ϕ; how do you think B_ϕ is estimated?

$$\nu_{\rm eff} \sim 10^7\,{\rm cm}^2\,{\rm s}^{-1}, \tag{3.4b}$$

$$|\mathbf{B}_p| \sim 10^{-5}\,{\rm Gauss}, \tag{3.4c}$$

for $\bar\rho \sim 1\,{\rm g\,cm}^{-3}$. None of these numbers is unreasonably high, so that no class of processes can be dismissed *a priori* with any confidence. In the remainder of this chapter we will consider various specific physical mechanisms that can contribute to angular momentum redistribution in the radiative core. At this juncture, in view of the above estimates we simply note the following points:

- The lower bound for $\nu_{\rm eff}$ corresponds to viscous transport enhanced by a factor of about 10^5 over that associated with simple microscopic viscosity, but still three to five orders of magnitude smaller than the effective viscosity in the convective envelope ($\nu_{\rm eff} \sim 10^{10}$—$10^{12}\,{\rm cm}^2\,{\rm s}^{-1}$, according to mixing length theory). While this may appear a large factor, it is actually not inconceivable that small-scale turbulence fed by rotational instabilities could lead to enhanced viscous-like transport at that level.
- The lower bound for $|\mathbf{B}_p|$ is of the order of the interstellar magnetic field. This is almost absurdly low, since conservation of magnetic flux during stellar formation is expected to intensify any pre-existing field. This suggests that magnetic field may well be a key player in the internal redistribution of angular momentum.

3.2 Viscous transport of angular momentum

We first consider a physical mechanism that is absolutely certainly acting in the solar radiative interior: angular momentum transport by ordinary microscopic viscosity. The process is described by:

$$\frac{\partial}{\partial t}(\rho\varpi^2\Omega) = \nabla\cdot[\rho\varpi^2\nu\nabla\Omega], \tag{3.5}$$

where ν is the coefficient of kinematic viscosity. What we call *viscosity* is the macroscopic consequence of momentum exchange occurring through collisions and scattering of the microscopic constituents of the fluid. The rate at which these collisions occur depends on the charge and mass of the colliding particles, their density, their mean kinetic energy, and so on. The kinematic viscosity ν can be expressed as

$$\nu = \frac{0.406 m_i^{1/2}(kT)^{5/2}}{\rho(Ze)^4\ln\Lambda} = 2.2\times10^{-15}\,\frac{T^{5/2}}{\rho\ln\Lambda}, \qquad [{\rm cm}^2\,{\rm s}^{-1}] \tag{3.6}$$

for a gas of fully ionized hydrogen, where the contribution of electron collisions to momentum exchange have been neglected. The quantity $\ln\Lambda$ is the Coulomb logarithm, where

$$\Lambda \simeq 10^{-5}\frac{T}{\rho^{1/2}}, \qquad [{\rm cgs}], \qquad T \gtrsim 4\times10^5\,K \tag{3.7}$$

At the base of the solar convective envelope, $\rho \sim 0.1\,\mathrm{g\ cm^{-3}}$ and $T \sim 2\times10^6\,\mathrm{K}$, which yields $\nu \sim 10^2\mathrm{cm^2\,s^{-1}}$. This will prove a useful number to keep in mind.

The important point here is that while it may be the case that the solar radiative interior is strictly turbulence free or unmagnetized, microscopic viscosity is a fundamental property of any fluid, and so *must* be taken into consideration. Using our above estimate $\nu \simeq 10^2\,\mathrm{cm^2\,s^{-1}}$ in conjunction with the timescale estimate given by eq. (3.3b) with $\nu_{\rm eff} \equiv \nu$ and $\ell \equiv R_\odot$ yields

$$\tau_\nu \simeq 10^{12}\,\mathrm{yr} \qquad \text{[microscopic viscosity]}, \tag{3.8}$$

indicating that while microscopic viscosity is certainly operating in the solar interior, on structural evolutionary timescales it makes a negligible contribution to the internal redistribution of angular momentum over length scales comparable to the size of the radiative core. This, however, does not guarantee that microscopic viscosity cannot make a significant contribution *locally*, in regions where large angular velocity gradients are present. We will have the occasion to revisit the role of microscopic viscosity in chapter 5.

3.3 Advective transport of angular momentum

We consider next the advective transport of angular momentum, as described by:

$$\frac{\partial}{\partial t}(\rho\varpi^2\Omega) = -\rho\mathbf{U}_p\cdot\nabla(\varpi^2\Omega) \tag{3.9a}$$

where $\mathbf{U}_p$ is an axisymmetric meridional flow:

$$\mathbf{U}_p = U_r(r,\theta)\hat{\mathbf{e}}_r + U_\theta(r,\theta)\hat{\mathbf{e}}_\theta. \tag{3.9b}$$

In a rotating star, numerous physical processes can contribute to $\mathbf{U}_p$. This is a vast topic which could easily occupy a full block of lectures; what follows is only a brief introduction to two such mechanisms; it includes some largely unsubstantiated statements, the origin of which should be sought in the numerous classical and contemporary references provided in the bibliography at the end of this chapter.

3.3.1 Ekman circulation

Consider an open cylindrical container of height H and cylindrical radius R filled with an incompressible (ρ =const.) viscous fluid and rotating (both container and fluid) at a fixed angular velocity Ω about a vertical axis coinciding with the axis of the container. Working in cylindrical polar coordinates (ϖ,θ,z), the ϖ-component of the equation of motions in static steady-state reads

$$\frac{u_\phi^2}{\varpi} = -\frac{1}{\rho}\frac{\partial p}{\partial\varpi} \tag{3.10}$$

where $u_\phi \equiv \varpi\Omega$. The centrifugal force (LHS) can only be compensated by a pressure gradient in the direction perpendicular to the rotation axis. Equation (3.10) is readily integrated to yield a pressure profile $p(\varpi, z)/p(0, z) = (1/2)\Omega\varpi^2$, where $p(0, z)$ is the fluid pressure at height z along the symmetry axis of the container. In an open rotating container filled with an incompressible fluid, this implies that isobaric surfaces —including the air-fluid surface— have the shape of paraboloids.

Assume now that the spin of the container is abruptly halted ($\Omega = 0$). Experience —and inertia— tells us that the bulk of the fluid will keep rotating pretty much at the same rate for a while. Near the container walls and bottom however, there will appear a thin, viscous boundary layer where the fluid's rotation will vary from $\sim \Omega$ at the top of the layer, down to zero at the boundary. The less viscous the fluid, the thinner the layer, but such a layer will *always* be there in view of the no-slip condition that must be imposed at rigid boundaries. Consider now the force balance within the thin layer adjacent to the bottom of the container. Because $u_\phi/\varpi < \Omega$ therein, the centrifugal force no longer balances the radial pressure gradient, since the latter is set *globally* by the rotation of the fluid in the bulk of the container. It follows that momentum balance in the ϖ-direction cannot be satisfied and consequently, within the layer, a flow will be generated, along the negative ϖ-direction (i.e., $u_\varpi < 0$). Mass conservation will require that fluid be sucked downward into the layer, and pumped out of the layer upwards along the rotation axis (The name "Ekman pumping" is often used in this context). Within the layer, the ϕ-component of the equation of motion now looks like:

$$\frac{\partial u_\phi}{\partial t} = -2\frac{u_\varpi u_\phi}{\varpi} + \nu\frac{\partial^2 u_\phi}{\partial z^2} \tag{3.11a}$$

Focus now on the nearly horizontal return flow ($u_\varpi > 0$) near the top of the container. The equation of motion there reduces to:

$$\frac{\partial u_\phi}{\partial t} = -2\frac{u_\varpi u_\phi}{\varpi} \tag{3.11b}$$

since there are no viscous stresses imposed there by rigid boundaries. The asymmetry between eq. (3.11a) and (3.11b) has important consequences. Along the top of the container fluid spins down to conserve angular momentum, cf. eq. [3.11b]) as it moves away from the rotation axis, but spins up by a lesser amount upon moving back toward the axis in the bottom boundary layer, in view of the ever-present vertical viscous stress existing there (eq. [3.11a], RHS). In this manner angular momentum is advectively carried from the bulk of the fluid to the boundary layer, and viscously from the layer to the boundary. The corresponding timescale for angular momentum evolution can be shown to be

$$\tau_{U,1} \simeq \left(\frac{H^2}{\nu\Omega}\right)^{1/2} \tag{3.12}$$

This needs to be be compared to the purely viscous timescale $\tau_\nu \simeq H^2/\nu$. For example, the Ekman spin-down timescale for water set spinning in a coffee cup ($\nu \sim 10^{-2}\,\mathrm{cm}^2\,\mathrm{s}^{-1}$, $H \sim 5\,\mathrm{cm}$, $\Omega \sim 2\pi$ rad s^{-1}) is $\tau_{U,1} = 20$s, while the viscous dissipation timescale is... $\tau_\nu \sim 40$ minutes! The former figure is far better in line with common experience. Clearly, Ekman circulation will dominate angular momentum redistribution for high rotation rate and low viscosities. This is measured by a dimensionless number called the *Ekman Number*:

$$E = \frac{\nu}{H^2\Omega} \tag{3.13}$$

For the solar interior, one has $E \sim 10^{-14}$ and $\tau_{U,1} \sim 10^5\,\mathrm{yr}$, suggesting that Ekman circulation should dominate over viscous effects in the internal redistribution of angular momentum.

How Ekman pumping may operate in the solar radiative interior is illustrated schematically on Fig. 3.1, in a situation where a shear $\partial\Omega/\partial r < 0$ exists within an Ekman layer located below the core-envelope interface. Under such circumstances, the flow in the boundary layer is θ-directed and poleward. Mass conservation requires that the underlying fluid be sucked into the layer in the equatorial regions, and ejected downward in the polar region, so that a large-scale flow must exist in the interior. An advected fluid parcel, moving outward from A to B on Fig. 3.1, spins down so as to conserve angular momentum since $\varpi = r\sin\theta$ is increasing. However, it does not spin back up by the same amount upon moving back towards the rotation axis (even though ϖ is now decreasing from B to C), since it does so within the boundary layer, where viscous stresses continuously decellerate the fluid. In this manner, angular momentum is continuously transferred from the core to the envelope; first by the flow from the interior to the Ekman layer, and then by viscous stresses from the Ekman layer to the convective envelope.

There are quite a few points to elucidate in the solar/stellar context: (1) how fast is the flow within the Ekman layer; (2) how deep does the return flow penetrate into the strongly stratified radiative interior; and, (3) how is the dynamics of the Ekman flow altered by the fact that the core-envelope interface is definitely *not* a rigid boundary.

An estimate of the flow velocity in the Ekman pumping layer can be obtained by dimensional analysis of eq. (3.11a) in a (quasi-) steady-state:

$$U \sim \frac{R_\odot \nu}{h^2}, \tag{3.14}$$

where h is the thickness of the layer. The theory of incompressible rotating fluids suggests an Ekman layer thickness $h = (\nu/\Omega)^{1/2} \sim 50$ meters, which is ridiculously thin and leads to an equally ridiculous $U \sim 3\,\mathrm{km\,s}^{-1}$ flow speed in the layer. Attempts to include compressibility and a non-rigid core-envelope boundary in the calculation has produced estimated speeds $\lesssim 10^{-5}\,\mathrm{cm\,s}^{-1}$ for the secondary Ekman flow, with larger flow velocities in the Ekman boundary layer proper, but numerous uncertainties remain. More serious is the fact that the return flow most likely

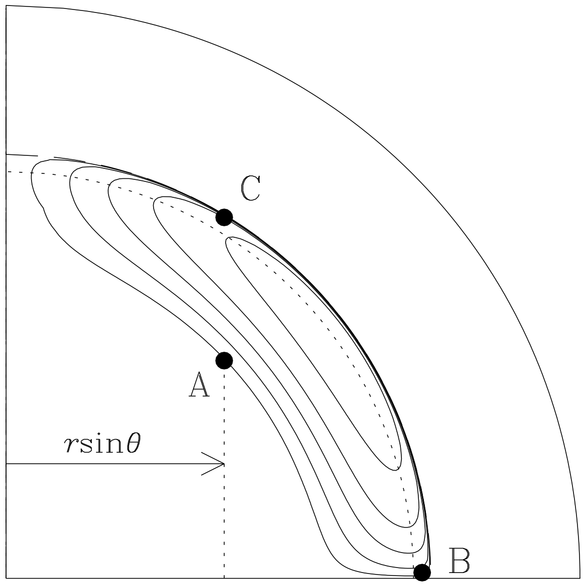

Figure 3.1: Schematic representation of Ekman circulation in a meridional quadrant. The core-envelope interface is indicated by a dashed line, and the extent of the Ekman pumping layer —its thickness exaggerated for illustrative purposes— by a dotted line. The strong density stratification is expected to deflect the Ekman circulation a few scale heights below the pumping layer; here this depth has been (arbitrarily) set at $0.5\,R_\odot$. The rotation axis is vertical and coincides with the left quadrant boundary.

closes upon itself no more than a scale height below the core-envelope interface, so that Ekman circulation probably cannot redistribute angular momentum in the bulk of the solar radiative interior, as it did for our cylindrical container of incompressible fluid. While no truly satisfactory theory applicable to solar/stellar radiative interiors is available as yet, the papers listed in the bibliography should give you a good flavor of the complexities and difficulties involved.

3.3.2 Thermally driven flows in rotating stars: a quick primer

The Ekman circulation discussed in §3.3.1 is *mechanically driven*, in the sense that it arises as a consequence of the impossibility, in a rotating but otherwise static ($\mathbf{U}=0$), steady-state ($\partial/\partial t=0$) system, to satisfy force balance in the presence of externally imposed viscous stresses. In the stably stratified portion of a rotating star, there exist additional mechanisms that can drive a large circulatory flow. The classical example is the so-called Eddington-Sweet meridional circulation, which arises from the impossibility of simultaneously satisfying hydrostatic and radiative equilibrium in the stably stratified interior of a rotating star.

In the absence of rotation (i.e., spherical symmetry), $\nabla T \equiv \partial T/\partial r$; the temperature and pressure gradients and gravity are then colinear, and static, steady-state, spherically symmetric solutions to the equations of stellar structures can be constructed as outlined in §1.2.2. Under this assumption and outside of the nuclear burning regions, the energy equation reduces to

$$\frac{\partial}{\partial r}\left(\chi\frac{\partial T}{\partial r}\right)=0 \tag{3.15}$$

where χ is the net thermal conductivity[3], the main contribution to which comes from radiative transport[4], so that

$$\chi\equiv\chi_R=\frac{4acT^3}{3\bar{\kappa}\rho} \tag{3.16}$$

where $\bar{\kappa}$ is the Rosseland mean opacity (units cm^2 g^{-1}), and $a=7.56566\times10^{-15}$ erg cm^{-3} K^{-4} is is the radiation pressure constant ($\equiv 4\sigma/c$, where σ is the Stefan-Boltmann constant of $L=\sigma T_{\rm eff}^4$ fame).

In the presence of rotation, however, things become more complicated. In a frame of reference rotating at the angular velocity Ω of a rigidly rotating Sun/star, a centrifugal force appears in the momentum equation. It can be expressed in

---

[3] This is a good place to clarify some confusing bits of notation where various authors adopt different definitions; The thermal conductivity χ (units erg (s K cm)$^{-1}$) was introduced by Fourier and relates heat flux $\mathcal{F}$ (units erg s^{-1} cm^{-2}) to the temperature gradient ∇T via a relation of the form:

$$Q=-\chi\nabla T.$$

The thermal diffusivity κ (units cm^2 s^{-1}), on the other hand, is the quantity appearing in the heat conduction equation:

$$\frac{\partial T}{\partial t}=\kappa\nabla^2 T$$

clearly, the two coefficients are related: $\kappa=\chi/\rho c_v$, where c_v is the specific heat at constant volume. Either coefficient can appear in the energy equation, depending on whether the latter is written in terms of temperature, entropy or internal energy (i.e., $\partial T/\partial t=$..., or $\partial S/\partial t=$..., etc.). To further complicate matters, the notation for χ and κ is not uniform throughout the literature; here we follow Tassoul's *Theory of rotating stars*, Batchelor's *An introduction to Fluid Dynamics* and Spiegel & Zahn in their original tachocline paper, but the exact opposite notation is used in Stix's *The Sun*, Hansen & Kawaler's *Stellar Interiors* and some popular compendia such as Lang's *Astrophysical Formulae*. Add to this that the symbol κ is often used to denote the opacity (we use $\bar{\kappa}$ herein), and that some authors use ν to denote the thermal conductivity (ν is used herein for viscosity), and you have an absolute mess. So beware.

[4] This of course is not the case in the convective envelope.

terms of a potential and used to define an effective gravity $\mathbf{g} = -\nabla\Phi$ such that the constraint of hydrostatic equilibrium (arising from consideration of the (r, θ)-component of the equations of motion in a static steady-state) becomes:

$$\frac{\mathrm{d}p}{\mathrm{d}\Phi} = -\rho\frac{\mathrm{d}}{\mathrm{d}\Phi}(V - \frac{1}{2}\Omega^2\varpi^2) \tag{3.17}$$

where $\varpi \equiv r\sin\theta$ is the perpendicular distance to the rotation axis, and $V = Gm(\Phi)/r$ is the usual gravitational potential, with $m(\Phi)$ the mass contained within a (nearly) spherical shell labeled by a given value of Φ. Because of the ϖ-dependency, we can now expect that the isobaric surfaces will no longer be exactly spherical; instead, p will be constant on surfaces $\Phi = const.$ In view of this rotationally-induced distorsion of the structure, the radiation field encounters a different density and pressure stratification along the polar axis than it does along the equatorial plane. As a consequence of this, temperature differences will tend to materialize along isobaric surfaces. There is nothing to balance the energy flux associated with this temperature gradient in a static steady-state; this is the (in)famous Von Zeipel paradox. Note that unlike the case of Ekman circulation, this will occur even for strict solid-body rotation. Balancing the non-zero divergence of the radiative flux is however possible by introducing a *meridional flow*

$$\mathbf{U} = U_r\hat{\mathbf{e}}_r + U_\theta\hat{\mathbf{e}}_\theta \tag{3.18}$$

such that

$$\rho c_v \mathbf{U}\cdot\nabla T = \nabla\cdot(\chi\nabla T), \tag{3.19}$$

so that steady-state (but no longer *static*) solutions of the energy equation can be constructed. Ultimately, the driving of this large-scale circulation arises from the relative heating/cooling of fluid elements located at different latitudes on the same isobaric surface. In response to this uneven heating/cooling the fluid will begin to rise/sink, leading to the buildup of a large-scale flow. If the rotation is rigid or very nearly rigid, and is small in the sense that the centrifugal force can be treated as a perturbation of the gravitational force, then the meridional flow is characterized by a single flow cell per quadrant, with fluid rising (sinking) in the polar (equatorial) regions.

At this point, in analogy with the Ekman circulation discussed in the preceding section, you may think that an order-of-magnitude estimate for the thermally driven meridional flow $\mathbf{U}$ can be obtained by dimensional analysis of eq. (3.19). This is not as simple, however, since the departure from spherical symmetry that is responsible for the non-vanishing of the RHS of eq. (3.19) is governed by the equations of motion, the equation of state, and Poisson's equation for the gravitational potential. An estimate for $\mathbf{U}$ can indeed be obtained, by perturbation analysis of the full set of structural equations. Launching into this here would really take us too far from our subject matter, so for now let us simply state[5] that

[5] I really hate to ask you to take things on faith like this, so please do take

the meridional flow speed is of order

$$|\mathbf{U}| \sim \frac{LR^5\Omega^2}{G^2M^3} \tag{3.20}$$

where L and M are the stellar/solar luminosity and mass. This implies a circulatory timescale

$$\tau_{U,2} \equiv t_{ES} \equiv \frac{R}{|\mathbf{U}|} = \frac{G^2M^3}{LR^4\Omega^2} \tag{3.21}$$

usually known as the Eddington-Sweet time. For the present-day Sun,

$$t_{ES} \simeq 2 \times 10^{12}\,\mathrm{yr}, \qquad \mathrm{Eddington-Sweet\ circulation},$$

i.e., much longer than its main-sequence lifetime, from which we conclude that rotationally-induced thermally-driven circulation makes a negligible contribution to mass and momentum transport in the bulk of the solar radiative core. Keep in mind that this may not always have been the case if the Sun went through a phase of rapid rotation near the ZAMS, like many solar-type stars seem to do (cf. §1.1). For a young Sun rotating at 50 times the present solar rate, $t_{ES} \simeq 10^9\,\mathrm{yr}$, which is now of the order of the Hyades age and much smaller than the main-sequence lifetime for a $1\,M_\odot$ star.

The above discussion may have left you with the impression that calculating a meridional circulation profile that offsets horizontal thermal gradients should be a relatively straightforward process. This is not the case. In particular, the meridional flow $\mathbf{U}$ also contributes terms in the ϕ-momentum equation, corresponding to the advection of angular momentum (unless $\mathbf{U}$ is parallel to the rotation axis, but this is not possible here[6]). This leads to $\partial\Omega/\partial t \neq 0$, which in turns locally alters the centrifugal force and feeds back nonlinearly on $\mathbf{U}$. Even in the axisymmetric case ($\partial/\partial\phi = 0$), finding self-consistent solutions for $\mathbf{U}(r,\theta)$ and $\Omega(r,\theta)$ is far from being a trivial task.

We conclude from this discussion that advective processes most likely do not contribute significantly to angular momentum redistribution in the bulk of the solar radiative interior. However, driving a large-scale flow is not the only way in which rotation can lead to angular momentum transport. This leads us to the next class of processes, viscous-like turbulent transport.

---

a bit of time to look into how eq. (3.20) can be obtained; good places to start are chapter 8 of Tassoul's *Theory of Rotating Stars*, and §42 of Kippenhahn & Weigert's *Stellar Structure and Evolution* (see bibliography).

[6] Why is it not possible to have $\mathbf{U}$ parallel to the rotation axis here?

3.4 Turbulent transport of angular momentum

3.4.1 Turbulent mass and momentum transport

One of the most confounding effects of (moderate) rotation in otherwise stably stratified radiative interiors is its potential for destabilization. The number of possible rotationally fed hydrodynamical instabilities is indeed enormous, and grows even larger in the presence of angular velocity gradients. For the purpose of the present discussion one may first establish a distinction between *dynamical* and *secular* instabilities. The former are violent instabilities, with very short growth rates. Many of these are discussed extensively in Tassoul's *Theory of rotating stars* (see bibliography), to which we refer the interested reader. It may be safely assumed that in the quasi-static evolutionary phases considered here, whenever stars become unstable with respect to such instabilities they readjust their structure (in particular their internal rotation profile) quasi instantly so as to restore stability. Secular instabilities are of a milder nature, and can manifest themselves as slow, large-scale bulk fluid motion (e.g. the Eddington-Sweet meridional circulation encountered in the preceding section), and/or small-scale fluid motions known as turbulence. Properly formulating a turbulent transport model is a rather involved task. At the very least, the steps involved are:

(1) Estimate conditions under which a given flow becomes unstable;

(2) Follow the growth of the instability into its nonlinear regime, to estimate the saturated amplitude of the resulting turbulent fluid motions;

(3) Construct appropriate expression for the transport coefficients associated with these turbulent motions.

Estimating hydrodynamical or MHD stability criteria (point [1] above) is already no simple matter (we will consider a specific instance of such calculations in chapter 5 below). Points (2) and (3) are even worse, as solar interior conditions are in a physical parameter regime far removed from that accessible in laboratory experiments or by the largest direct numerical simulations than can be performed today, or next year for that matter. Perhaps the simplest approach, and the one to date almost universally adopted in the solar/stellar astrophysics literature, is to retain the functional form of the viscous stress tensor, while replacing the microscopic viscosity ν by an "effective viscosity" ν_{eff}, with $\nu_{\text{eff}}/\nu \gg 1$. Some theoretical justification for this admittedly very simplistic approach to turbulent transport modeling will be provided in the following chapter.

In practice quantities such as ν_{eff} cannot be computed from first principles, and so the resulting transport models are not truly *predictive*. A more pragmatic approach consists in treating quantities such as ν_{eff} as adjustable parameters, to be calibrated by confronting the resulting rotational evolution models with observations. This then yields a *descriptive* model, which remains a useful tool to interpret observation and develop physical intuition. Because many adjustable parameters are usually needed to define a turbulent transport model, additional observables are required for this strategy to be meaningful.

One such set of secondary observables is the abundances of the light elements lithium, beryllium and boron. These elements are destroyed by proton capture at relatively low temperatures, and so can be used as probes of the extent of turbulent mixing in stellar radiative interiors. The underlying idea is that the small scale turbulent motions responsible for enhanced, viscous-like angular momentum transport will also cause enhanced transport of chemical species, above and beyond the rate associated with purely microscopic diffusion processes. The quality of the available data (particularly for Li) is such that this procedure can yield constraints on the rotational evolution models themselves. Let us then digress a bit on the topic of light elements and their abundances.

3.4.2 Light element abundances

The so-called light elements Lithium (Li), Beryllium (Be) and Boron (B) are only present in minute quantities in the Sun. Current abundance determinations and meteoritic values (assumed to be representative of the protosolar nebula) are as follows:

Table 3.1

Observed light element abundances, $\log(X_E/X_H)$

Element	Present-day Solar	Meteoritic	Depletion factor
Li	1.16 ± 0.1	3.31 ± 0.04	$\simeq 10^{-2}$
Be	1.15 ± 0.10	1.42 ± 0.04	$\simeq 0.5$
B	2.6 ± 0.3	2.88 ± 0.04	~ 1

Abundances are given logarithmically with respect to Hydrogen, with $N_H = 10^{12}$, and the depletion factor is simply the ratio of the present-day solar photospheric value to the meteoritic value. Li is depleted by a factor ~ 100 with respect to its "initial" value, while Be and B are essentially undepleted. The observed solar light element abundances are of course only representative of the solar atmosphere. What about in the interior ?

When a proton impinges on a ^{7}Li nucleus with sufficient kinetic energy to overcome the Coulomb barrier, the resulting assemblage of four protons and four neutrons, which one would want to associate with some excited state of ^{8}Be, quasi-instantly forms two Helium nucleii instead[7]:

$$^7\mathrm{Li} + \mathrm{p} \rightarrow 2\,^4\mathrm{He} + 17.3\,\mathrm{MeV}$$

This is known as a (p, α) reaction. Likewise, under solar interior conditions, proton capture by ^{9}Be and ^{10}B almost always ends up producing two He nucleii, plus

[7] The lifetime of the excited state of ^{8}Be resulting from proton capture by a ^{7}Li nucleus has actually been measured; it is a few times 10^{-16} s!

some leftovers proton and neutrons[8]. This is all due to the extremely high nuclear binding energy of ^{4}He, itself arising from the filling of the first proton and neutron nuclear shells. Given the high temperatures and proton densities characterizing the solar interior, sufficiently energetic collisions can be expected to be quite common in the bulk of the interior. Indeed, calculations of nuclear reaction rates indicate that during most phases of their evolution, most stars are far better at destroying light elements than at producing them. Because of the small abundances of the nucleii involved, the energy so liberated ends up making an utterly negligible contribution to the stellar luminosity.

Figure 3.2 shows the expected profiles of light element abundances in a present-day solar model, in the absence of any mixing. The aforementioned extreme sensitivity of the light element to proton capture reactions translates into step-like abundance profiles, with the abundances going from undepleted to zero over a very narrow temperature interval. Moving downward from the base of the convective envelope, Li vanishes abruptly below $T \simeq 2.7 \times 10^6$ K, Be below 3.5×10^6 K, and B below 5×10^6 K. This translates into depths of $r/R_\odot \simeq 0.65$, 0.54 and 0.4, respectively. Clearly, an essentially normal Be abundance *and* a Li depletion by a factor of $\sim 10^2$ imposes strict bounds on the spatial extent of mixing below the solar convective envelope; mixing must extend down a distance of at least $\delta \sim 0.1 R_\odot$, but not exceeding 0.15—0.2 $R_\odot$ or, alternately, at least one scale height below the base of the envelope, but less than two. This represents an extremely stringent constraint on *any* global mixing mechanism operating below the convective envelope.

3.4.3 Simple models with enhanced, "turbulent" viscosity

In this section we consider perhaps the simplest possible model for the evolution of angular momentum and light element abundances in the Sun. Given a solar model, we assume spherical symmetry, and neglect any large-scale flow or magnetic field. The ϕ-component of the equations of motion reduces to:

$$\rho r^2 \frac{\partial \Omega}{\partial t} = \frac{1}{r^2} \frac{\partial}{\partial r} \left[\rho \nu r^4 \frac{\partial \Omega}{\partial r} \right] \tag{3.22}$$

where ν is the coefficient of kinematic viscosity. The governing equation for the Li concentration c has a similar form:

$$\rho \frac{\partial c}{\partial t} = \frac{1}{r^2} \frac{\partial}{\partial r} \left[\rho D_{12} r^2 \frac{\partial c}{\partial r} \right] + \rho S c \tag{3.23}$$

where D_{12} is the coefficient of microscopic diffusion (units cm^2 s^{-1}), for a trace species ("2") in a background gas ("1"). The quantity S (< 0) in (3.23) is a nuclear reaction rate (units s^{-1}) which, for the light elements, is a very rapidly

[8] Try to work out what the (p, α) reaction products are in the case of ^{9}Be and ^{10}B.

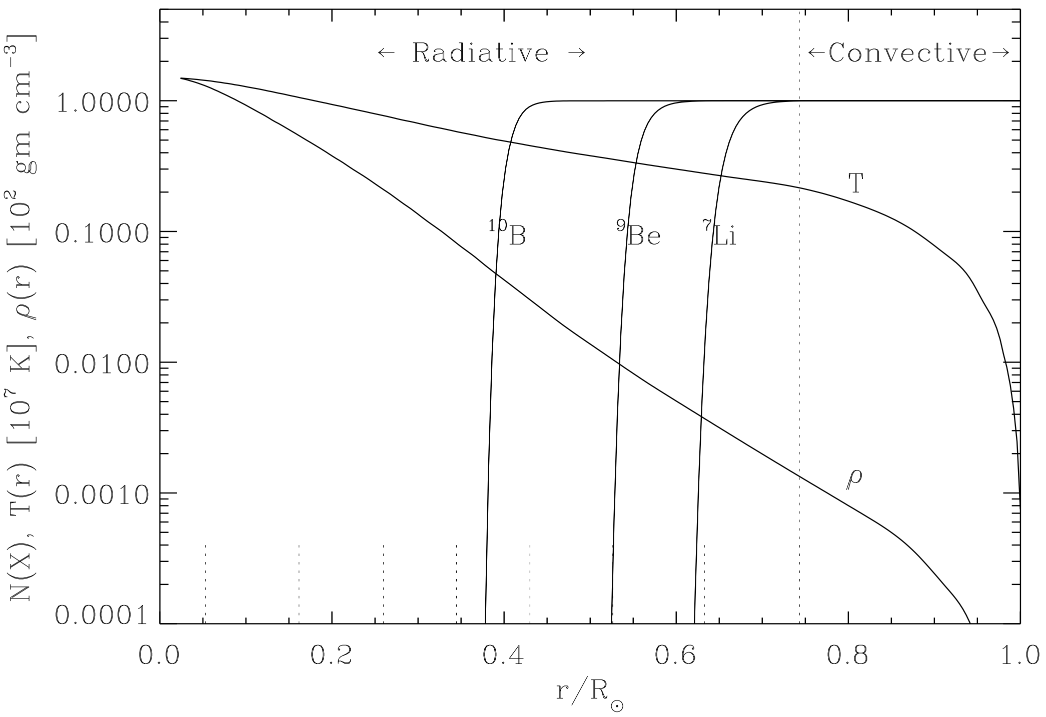

Figure 3.2: Expected variations with depth of the abundances of Li, Be and B in a present-day solar model, in the absence of any kind of mixing in the radiative interior. All abundances are normalized to their value on the ZAMS. The extreme temperature sensitivity of the (p, α) nuclear reactions causing the depletion of the light elements leads to step-like abundance profiles. The base of the convective envelope is located at $r/R_\odot \simeq 0.74$, where the temperature $T \simeq 2 \times 10^6$ K. The dotted tick marks along the lower x-axis are separated by one density scale height, working downward from the base of the convective envelope.

varying function of temperature[9]. Equation (3.23) is nothing more than a mass conservation statement for the trace species; local variations in the concentration are due either to a non-zero divergence of the diffusive flux (first term on RHS), or local destruction by nuclear reactions (second term on RHS).

Like viscous momentum transport, diffusive mixing of a specie of trace particle in a background of a different particle specie is also a consequence of collisions between the fluid constituents; when collisions with the background particles are dominant, the diffusion coefficient D_{12} is relatively easy to calculate. It turns out that for trace particle diffusion in a background of fully ionized hydrogen under

[9] And we do mean rapid; someone bothered to estimate that around $T \simeq 2.5 \times 10^6$ K, the rate of the (p, α) reaction responsible for Lithium burning varies as $\sim T^{22}$!

solar interior conditions, one has

$$D_{12} \simeq \nu \tag{3.24}$$

to an excellent level of approximation for light elements. Consequently, in what follows we use eq. (3.6) to evaluate both ν and D_{12} as a function of depth in our solar model.

As a first cut at a turbulent transport model, we consider a situation where small-scale turbulence is present, and its transport properties can be modeled via turbulent diffusion coefficients. Specifically, we replace ν by $\nu_{\rm eff}$ ($\gg \nu$) in eq. (3.22), and D_{12} by D_T ($\gg D_{12}$) in eq. (3.23). Rather than using some *ad hoc* functional form for $\nu_{\rm eff}$ and D_T, this substitution is carried out by simply multiplying the microscopic transport coefficients by a fixed numerical coefficient ($\gg 1$). For want of knowing any better, we also assume that

$$\frac{\nu_{\rm eff}}{\nu} = \frac{D_T}{D_{12}} \tag{3.25}$$

i.e., both transport coefficients are enhanced by the same factor with respect to their microscopic values[10]. Under such a setup eqs. (3.22) and (3.23) are decoupled, and so can be solved independently.

Figure 3.3 shows the surface rotation rate $\Omega_{\rm surf} \equiv \Omega(R_\odot)$ (panel [A]) and internal angular velocity profiles $\Omega(r)$ (panel [B]) for a sequence of solutions to eq. (3.22) for various values of $\nu_{\rm eff}/\nu$. All model begin on the ZAMS in a state of solid-body rotation at 50 times the present solar rate, and the Weber-Davis solution of §I.4.3 is used to compute the angular momentum loss rate, assuming as before $B_{\rm surf} \propto \Omega_{\rm surf}$. Solid-body rotation is enforced at all times in the convective envelope ($r/R_\odot = 0.734$ for the model used here). The curves are coded according to the enhancement factor $\nu_{\rm eff}/\nu$.

Upon examining Figure 3.3, it should be clear that the rotational evolution predicted by our model depends rather sensitively on the adopted value for $\nu_{\rm eff}/\nu$. We need to understand physically why this is so.

Figure 3.4 shows, for the three solutions of Figure 3.3, the time variations of the wind-mediated torque, as computed from the Weber-Davis model (thinner lines), and the net viscous torque at the core-envelope interface (thicker lines). The latter quantity is defined as

$$\sigma_\nu = 2\pi \rho r^4 \nu_{\rm eff} \int_0^\pi \frac{\partial \Omega}{\partial r} \sin^2\theta {\rm d}\theta. \tag{3.26}$$

where all quantities on the RHS are evaluated at the core-envelope interface. Since we started from an initial condition of internal solid-body rotation, at very early

---

[10] which implies that mass is being transported as efficiently as angular momentum. Can you think of a physical mechanism that can transport momentum more efficiently than mass?

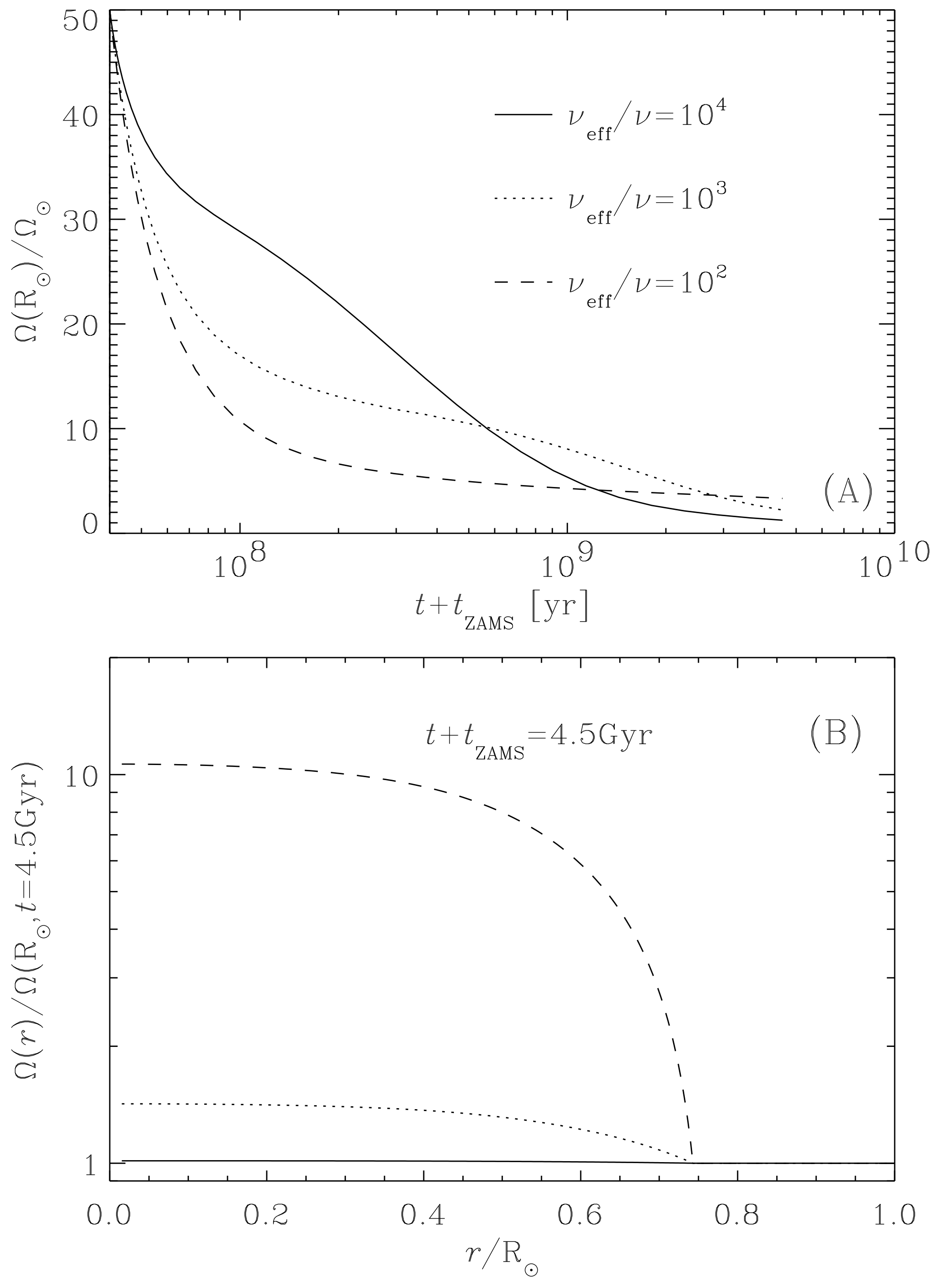

Figure 3.3: Evolution of surface and internal rotation in a solar model in response to turbulent mixing, modeled as a diffusion process as per eq. (3.22). Evolution was started on the ZAMS, on which a solar-like model arrives after a time $t_{\rm ZAMS} \simeq 4 \times 10^7$ yr. Part (A) shows the variation with time of surface rotation. Curves are labeled according to $\nu_{\rm eff}/\nu$. Part (B) shows internal differential rotation profiles in the interior (same curve coding as part [A]), at the age of the present-day Sun. A value $\nu_{\rm eff}/\nu \gtrsim 10^3$ leads to a flat rotation profile in the bulk of the radiative core, in agreement with helioseismic inferences.

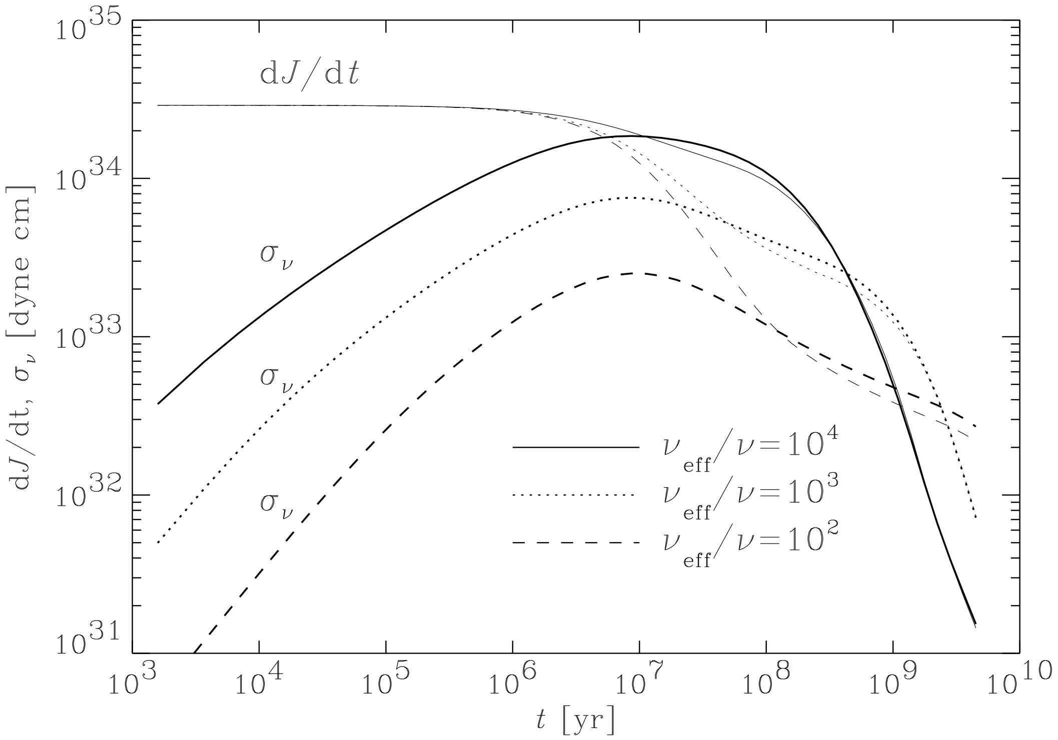

Figure 3.4: Dynamics of the "turbulent viscosity" solutions plotted on Figure 3.3. Note the horizontal axis is now simulation time t, not $t+t_{\rm ZAMS}$ as on Fig. 3.3. The thin lines correspond to the wind-mediated torque, and the thicker lines to the integrated viscous stress at the core-envelope interface (eq. [3.26]). At late time all solutions are characterized by a dynamical balance between the viscous stress and the applied torque (see text). Curve coding in terms of the enhancement factor, as on Figure 3.3.

times there is little or no viscous stress to offset the torque applied on the convective envelope by the wind, so the envelope begins to spin-down, on a timescale $\sim 10^6$ yr for an initial rotation rate of $50\Omega_\odot$ (cf. §1.4.2). The radiative core, however, retains its original angular velocity. This is what we referred to in §1.4 as *core-envelope decoupling*. As the envelope spins down, a radial shear steadily builds up at the core-envelope interface, with which is associated a viscous torque (σ_ν) that tends to offset the applied torque (dJ/dt). There eventually comes a time where this viscous torque equals in magnitude the applied torque, which means that angular momentum is being transferred from the core back up into the envelope at more or less the same rate as it is being carried away from the envelope by the wind. Figure 3.4 shows that this occurs after 10^7—10^8 yr, depending on the assumed value for $\nu_{\rm eff}/\nu$. The Figure also shows that this state of dynamical balance characterizes the subsequent evolution of the system.

Because models with lesser viscous coupling between the core and envelope spin down faster at first, they end up losing less total angular momentum than their more strongly coupled counterparts. This is because the angular momentum loss rate is proportional to a relatively high power of $\Omega_{\rm surf}$. As a consequence, models with lower $\nu_{\rm eff}/\nu$ values, even though they initially spin down faster, end up rotating *faster* at later times, because angular momentum is slowly getting transferred back up from the core to the envelope. This is a feature that we will encounter again further below in the context of magnetized models. For the same reason, models starting with different initial rotation rates but identical $\nu_{\rm eff}/\nu$ all end up rotating at about the same rate after a few Gyr. In models with lesser viscous coupling ($\nu_{\rm eff}/\nu \lesssim 10^3$, say), the internal differential rotation at the age of the present-day Sun becomes a very sensitive function of the value adopted for $\nu_{\rm eff}/\nu$. One also sees on Fig. 3.3(B) that a flat internal rotation curve in the deep radiative core after 4.5Gyr requires $\nu_{\rm eff}/\nu \gtrsim 10^3$.

Figure 3.5 is similar in format to Fig. 3.3, and shows the surface Li and Be abundances in a series of models with the same enhancement factors (here corresponding to D_T/D_{12}) used to obtain the solutions of Figure 3.3. Once again the convective envelope is assumed to remain thoroughly mixed. The surface Li and Be abundances are very sensitive function of D_T/D_{12} for $D_T/D_{12} \gtrsim 10^2$. For an enhancement factor of $\sim 10^2$, the solar Li abundance is adequately reproduced, but Be ends up depleted by twice the observed level. Fine tuning the model (namely, the D_T/D_{12} ratio) to produce a quasi-normal Be abundance is of course possible, but this then leaves Li insufficiently depleted.

At any rate the situation is as follows: the flat (or nearly flat) rotation profile in the solar radiative core inferred from helioseismic inversions requires that

$$\frac{\nu_{\rm eff}}{\nu} \gtrsim 10^3 \tag{3.27a}$$

while the solar Li and Be abundances can only be approximately reproduced for

$$\frac{D_T}{D_{12}} \simeq 10^2 \tag{3.27b}$$

If we insist that eq. (3.24) should hold, then both constraints cannot be reconciled. Evidently, they could be if one were to assume

$$\frac{\nu_{\rm eff}}{\nu} \simeq 10 \times \frac{D_T}{D_{12}} \tag{3.27c}$$

but at this stage of the game this would represent a rather *ad hoc* assumption, especially given the simplistic nature of our little model[11].

3.4.4 The Yale models

In retrospect, we should perhaps not be overly concerned with the failure of our simple model. After all, our aim was to produce a model which took into account

[11] Can you think of other possible ways to “fix” our little model?

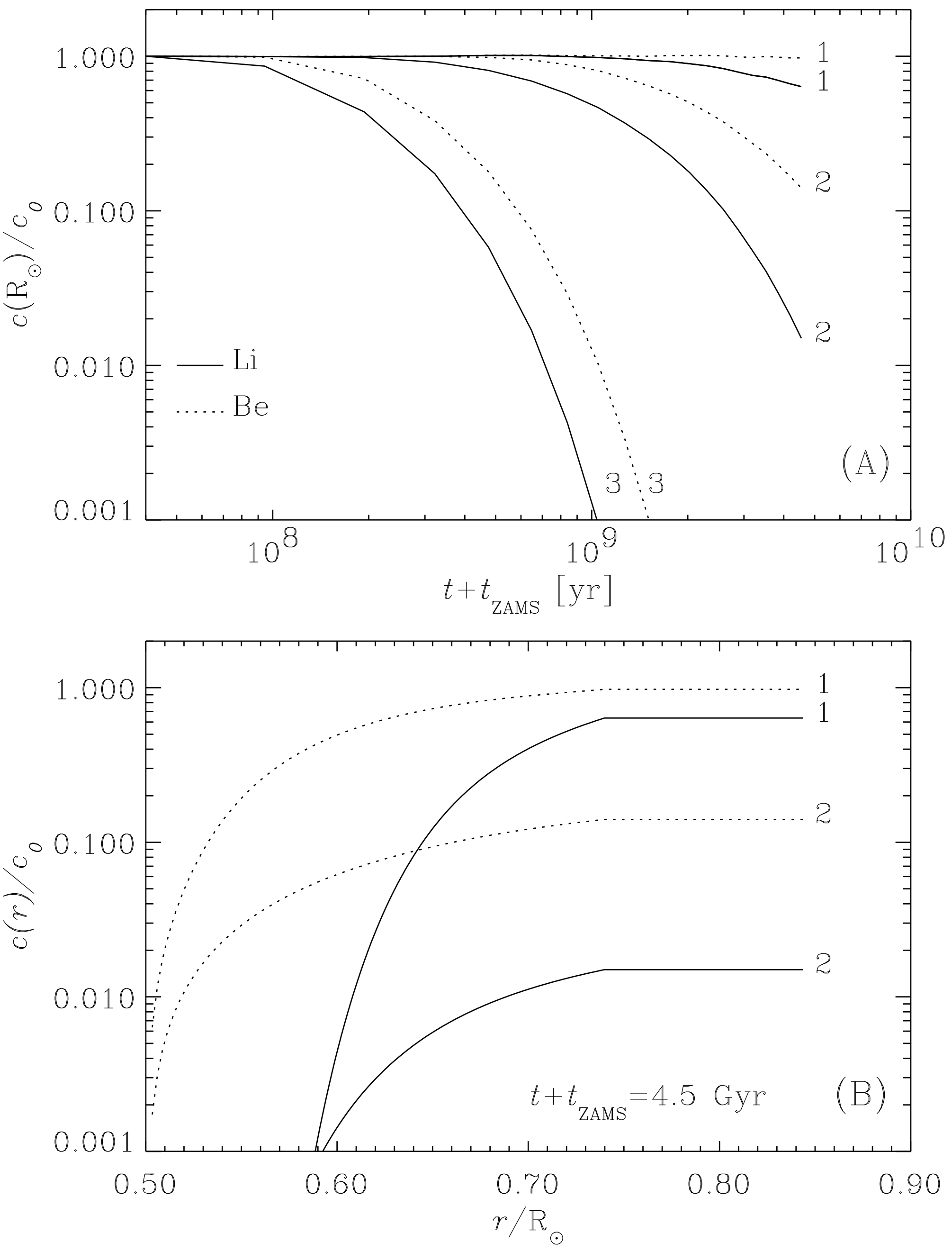

Figure 3.5: Evolution of Li and Be abundance in a solar model in response to turbulent mixing, modeled as a diffusion process, as per eq. (3.23). As on Fig. 3.3, evolution was started on the ZAMS ($t_{\mathrm{ZAMS}} \simeq 4 \times 10^7\,$yr). Part (A) shows the variation with time of surface abundances. Curves are labeled according to $\log(D_T/D_{12})$. Part (B) shows abundance profiles in the interior, at the age of the present-day Sun. The model with $D_T/D_{12} = 10^3$ ends up completely depleting Li and Be, so that the resulting curves are off scale on part (B). A value $D_T/D_{12} \sim 10^2$ a Li abundance compatible with observation, but produces too much Be depletion.

the transport properties of rotationally-induced turbulence, yet our prescription for ν_{eff} and D_T ended up being independent of rotation! In this section we briefly describe one set of recent (and relatively influential) models that explicitly introduce a dependency on Ω in the transport coefficients themselves. These models were originally developed by A. Endal and S. Sofia in the early 1980's, brought to maturity by M. Pinsonneault *et al.* in the late 1980's, and further elaborated upon by B. Chaboyer *et al.* in the mid-1990's. Since all these individuals were at these various times associated with the Astronomy Department at Yale University, their rotational evolution models are often referred to as the "Yale Models".

Within the general framework of the Yale models, the primary mechanism leading to the redistribution of angular momentum and chemical species in the upper part of the solar radiative interior is the *shear instability* of the internal differential rotation. We are concerned here with the *radial* shear developing as a result of the wind-induced rotational deceleration of the convective envelope.

The first thing needed is a stability criterion, i.e., an estimate of the minimal angular velocity gradient above which the flow becomes shear-unstable. Then, we need expressions for the transport coefficients associated with the turbulent flow field resulting from the growth of the instability and its saturated amplitude in the nonlinear regime. That's a pretty tall order, it turns out.

Is it known experimentally that a plane parallel, stratified shear flow $\mathbf{u} = (u(z), 0, 0)$, $\rho(z)$ with $\mathbf{g} = -g\hat{\mathbf{e}}_z$ is found to become unstable whenever the Richardson number

$$R_i = -g\frac{(\partial \ln \rho/\partial z)}{(\partial u/\partial z)^2} \tag{3.28}$$

drops below a certain critical value R_{crit}, equal to $1/4$ in the absence of other stabilizing and/or destabilizing mechanisms. The quantity R_i measures the relative influences of the (destabilizing) shear flow with respect to the (stabilizing) density stratification. In the stellar interior context, gradients in mean molecular weight are expected to stabilize the flow, while radiative diffusion is expected to destabilize it.

Nobody has yet derived from first principles an equivalent to eq. (3.28) applicable to solar interior conditions. The Yale models make use of a plausible stability criterion put forth by J.-P. Zahn, on the basis of an heuristic argument:

$$R_i = R_e\left(\frac{\nu}{\kappa}\right)N^2\left(\frac{\mathrm{d}U}{\mathrm{d}z}\right)^{-2} \tag{3.29}$$

where N is the Brunt-Väisälä frequency, κ the thermal diffusivity, and R_e is a Reynolds number characterizing the shear flow. Note that this stability criterion attempts to take into account the destabilizing effect of radiative diffusion. The growth of the shear flow instability has not yet been properly studied for solar interior conditions, even in its linear regime, so that even if eq. (3.29) is taken at face value, the associated ν_{eff} and D_T cannot be computed from first principles. The Yale models again make use of an estimate due to Zahn. In the notation of these notes:

$$\nu_{\text{eff}}(\Omega) = \frac{2c}{27G} \left| \frac{\mathrm{d}\ln T}{\mathrm{d}r} - \frac{2}{3}\frac{\mathrm{d}\ln\rho}{\mathrm{d}r} \right|^{-1} \frac{r^4}{\bar{\kappa}\rho m} \left(\frac{\mathrm{d}\Omega}{\mathrm{d}r}\right)^2 \tag{3.30}$$

where m is the mass contained within a sphere of radius r in the solar model. Fully aware of the heuristic nature of the derivation leading to eq. (3.30), the Yale modelers multiply the RHS of (3.30) by a numerical coefficient f_ν (or order unity), which they treat as an adjustable parameter in their model. They also introduce another adjustable parameter, f_c (< 1), measuring the relative efficiency of mass and angular momentum transport; again in our notation,

$$D_T = f_c \nu_{\text{eff}} \tag{3.31}$$

Their total diffusion coefficients actually include contributions from other physical mechanisms, but in the outer part of the radiative core the main contribution comes from the shear flow instability, as given by eq. (3.30). Equations (3.22) and (3.23) are then solved in parallel with the equations of stellar structure, using the above prescriptions for ν_{eff} and D_T, starting the calculations on the pre-main sequence and pushing it all the way to the giant branch. Note that eq. (3.23) is now coupled to eq. (3.22), since D_T is an explicit function of Ω (more accurately, of its gradient).

The models meet with a remarkable degree of success in reproducing the light element abundances. Once the various adjustable parameters in the model (14 of them) are tuned to reproduce the solar surface rotation and light element abundances (as well as the usual structural observables such as T_{eff}, $R_\odot$, etc.), the use of the same parameter values in stellar models of masses other than $1\,M_\odot$ reproduces moderately well the surface rotation but quite well the light element abundances in solar-type stars of various ages (cf. §1.1). However, their "reference" solar model is characterized by a degree of internal differential rotation in the radiative core that is far in excess of the bounds set by helioseismology. Despite the model's successes, an important component seems to be lacking. In the following section we look into one physical mechanism that can provide the missing ingredient.

3.5 Magnetic transport of angular momentum

In this section we consider the main sequence rotational evolution of an internally magnetized solar-type star. Specifically, we are interested in modeling the time-dependent, magnetically mediated redistribution of angular momentum which takes place within the radiative interior of a $1\,M_\odot$ star, in response to wind-induced rotational deceleration of the outer, convective envelope. We *assume* the existence of a large-scale poloidal magnetic field within the solar radiative interior. This field is assumed to be of fossil origin, i.e., a relic from star formation.

3.5.1 Basic mechanism

Consider an axisymmetric system, i.e., one in which the rotation and magnetic axes coincide, and where flux freezing is effectively enforced. An externally imposed shear $\nabla\Omega$ acting on a pre-existing poloidal magnetic field $\mathbf{B}_p$ induces a toroidal component, as described by the ϕ-component of the induction equation:

$$\frac{\partial B_\phi}{\partial t} = \varpi \mathbf{B}_p \cdot \nabla\Omega. \tag{3.32}$$

in the absence of dissipation ($\eta \equiv 0$). For a time-independent shear and poloidal field, eq. (3.32) yields a growth of B_ϕ that is locally linear in time, at a rate proportional to the magnitudes of the poloidal field and shear. This growth will not proceed indefinitely, however. The toroidal component gives rise to a growing azimuthally-directed Lorentz Force component[12]

$$[(\nabla \times \mathbf{B}) \times \mathbf{B}]_\phi \propto \varpi^{-1} \mathbf{B}_p \cdot \nabla(\varpi B_\phi). \tag{3.33}$$

It is easy to verify that this Lorentz force acts in such a way as to oppose the driving shear. Physically, the internal redistribution of angular momentum occurs via the propagation of torsional Alfvén waves propagating along the poloidal fieldlines.

In the absence of dissipation and external forcing, the only steady-states allowed by eq. (3.32) must satisfy

$$\mathbf{B}_p \cdot \nabla\Omega = 0. \tag{3.34}$$

Equation (3.34) constrains Ω to be constant *along* each poloidal magnetic fieldline, but does not rule out angular velocity differences *across* fieldlines. A configuration satisfying eq. (3.34) is termed *isorotational*. The timescale τ_B (cf. eq. [3.3c]) obtained previously is expected to characterize the evolution towards an isorotational state, but evidently this can be quite distinct from a state of strict solid-body rotation, i.e., Ω constant along *and* across fieldlines. In an axisymmetric system, angular momentum transport across fieldlines can only occur dissipatively. In the context of the solar spin-down, the rotational state of the interior is thus likely to depend rather sensitively on the relative timescales for

(1) Angular momentum redistribution *along* fieldlines,
(2) Viscous (dissipative) coupling *across* fieldlines,
(3) External forcing by the wind-mediated torque.

The timescale τ_B obtained in §3.1 can be expected to adequately characterize only phase (1). Hence order-of-magnitude arguments for the existence of a state of strict solid-body rotation in the solar interior based exclusively on estimates of the timescale τ_B should be considered with some caution[13].

---

[12] Is this the only Lorentz force component associated with the shearing of the poloidal field?

[13] What do you think would happen in a *non-axisymmetric* system, i.e., one where the rotation and magnetic axes no longer coincide? Is isorotation still an acceptable steady-state? Hint: consider the ϕ-component of the equations of motion in the equatorial plane of an axisymmetrically rotating star within which is embedded a magnetic dipole with its axis tilted by $pi/2$ with respect to the rotational symmetry axis.

3.5.2 The Charbonneau & MacGregor model calculations

We focus now on one set of axisymmetric model calculations, discussed in a relatively recent paper by yours truly and K.B. MacGregor, with additional results from the more recent work of G. Barnes *et al.* (see bibliography). The calculations span the interval between the time of arrival on the ZAMS and the age of the present-day Sun, and *assume* the existence of a large-scale, time-independent poloidal field in the radiative interior. Neglecting rotationally or magnetically induced large-scale meridional fluid motions, adopting spherical polar coordinates (r, θ, ϕ), and assuming strict axisymmetry, the total velocity $\mathbf{U}$ and magnetic field $\mathbf{B}$ can be written as

$$\mathbf{U} = \Omega(r, \theta, t)\, r\, \sin\theta\, \hat{\mathbf{e}}_\phi, \tag{3.35a}$$

$$\mathbf{B} = \mathbf{B}_p(r, \theta) + B(r, \theta, t)\, \hat{\mathbf{e}}_\phi. \tag{3.35b}$$

The problem reduces to solving the (coupled) ϕ-components of the momentum and induction equations:

$$\rho\, r^2 \sin^2\theta\, \frac{\partial \Omega}{\partial t} = \nabla \cdot (\rho\, \nu r^2 \sin^2\theta \nabla\Omega) + \frac{1}{4\pi}\mathbf{B}_p \cdot \nabla(r \sin\theta\, B_\phi), \tag{3.36a}$$

$$\frac{\partial B}{\partial t} = \eta\nabla^2(B_\phi \hat{\mathbf{e}}_\phi) + r\sin\theta\, \mathbf{B}_p \cdot \nabla\Omega, \tag{3.36b}$$

where ν is as before the coefficient of kinematic viscosity, and η the magnetic diffusivity, both assumed to be constant throughout the domain of interest. The first term on the RHS of eq. (3.36a) corresponds to momentum transfer by viscous processes, while the second term is the Lorentz force. The first term on the RHS of eq. (3.36b) corresponds to resistive dissipation, and the second to magnetic induction. We write the (time-independent) poloidal part of the magnetic field ($\mathbf{B}_p$) in terms of a poloidal flux function $\Phi(r, \theta)$:

$$\mathbf{B}_p(r, \theta) = B_r \hat{\mathbf{e}}_r + B_\theta \hat{\mathbf{e}}_\theta = \frac{B_0\, f_B}{r \sin\theta}\left[\frac{1}{r}\frac{\partial\Phi(r,\theta)}{\partial\theta}\,\hat{\mathbf{e}}_r - \frac{\partial\Phi(r,\theta)}{\partial r}\,\hat{\mathbf{e}}_\theta\right], \tag{3.37a}$$

where

$$\Phi(r, \theta) = \begin{cases} r^2(R - r)\sin^2\theta & r \leq R \\ 0 & r > R \end{cases} \tag{3.37b}$$

and B_0 is a measure of the *poloidal* field strength, with the numerical factor f_B (of order unity) adjusted so that $||\mathbf{B}_p|| = B_0$ midway between the surface and the center, along the polar axis. Equations (3.37) describe a dipolar field contained within the sphere $r = R \leq R_\odot$, as shown on Fig. 3.5. We will refer to these field configurations as D1 through D4, respectively[14]. Note that D1 and D2 are such that direct magnetic coupling exists between the CE and the radiative core (i.e.,

[14] How would you write $\Phi(r, \theta)$ to generate a quadrupolar magnetic field?

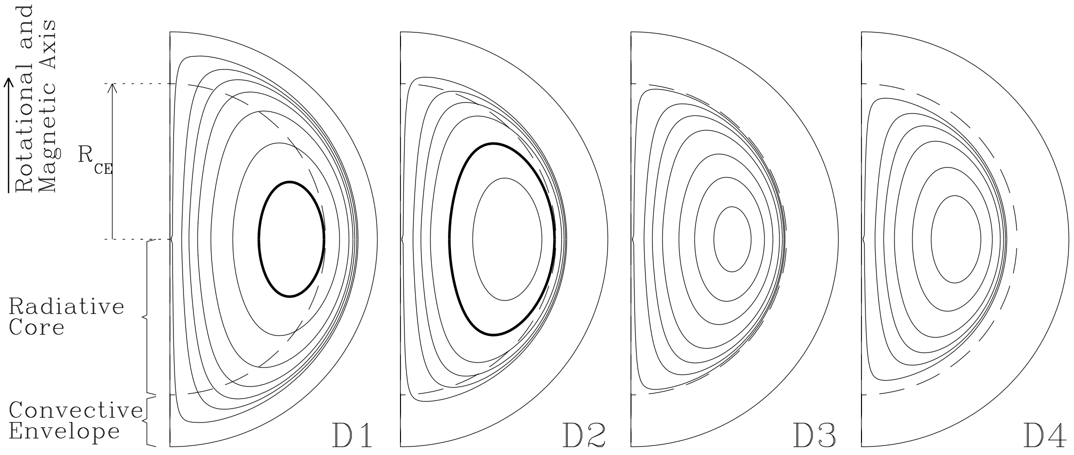

Figure 3.6: Poloidal magnetic field configurations generated via eqs. (3.37). All fields are dipoles contained below a spherical shell $r = R_2$. Fields D1, D2, D3 and D4 have $R_2/R_\odot = 0.9$, 0.8, $R_{\rm CE}/R_\odot$ and 0.7 respectively. The bottom of the convective envelope is located at $R_{\rm CE}/R_\odot = 0.74302$ in our solar model. Direct magnetic coupling exists at the core-envelope interface (i.e., $B_r \neq 0$ at $r = R_{\rm CE}$ for some θ) for the D1 and D2 configurations, but not for D3 and D4. Note however that in the former, there still exists a portion of the radiative interior (the "dead zone") that is threaded by fieldlines that do not "connect" onto the base of the envelope; the fieldline defining the boundary of this region is plotted using a thicker line.

$B_r \neq 0$ at $r = R_{\rm CE}$ for some θ), while for D3 and D4 the envelope is magnetically decoupled from the underlying core. In configurations D1 and D2, a portion of the radiative interior, centered on the equator, is threaded by fieldlines that close on themselves without ever penetrating the envelope. This region (often dubbed "dead zone" in the literature) is thus magnetically decoupled from the rest of the envelope, in the sense that transport of angular momentum by torsional Alfvén waves into or out of these regions is impossible; in axisymmetric systems, Alfvén waves redistribute angular momentum *along* fieldlines, but not across them.

Equations (3.36) describe an initial-boundary value problem in two spatial dimensions for $\Omega(r, \theta, t)$ and $B_\phi(r, \theta, t)$, governed by two coupled, linear, second-order PDEs to be solved in a meridional quadrant ($0 \leq r/R_\odot \leq 1$, $0 \leq \theta \leq \pi/2$)[15]. These must be supplemented by suitable initial and boundary conditions; Charbonneau and MacGregor begin their calculations on the ZAMS, where they set

$$\Omega(r, \theta, 0) = 50\Omega_\odot \tag{3.38a}$$

[15] Hey, hold it Scotty, shouldn't we be solving eqs. (3.36) in a full meridional quadrant instead? Why not?

$$B(r,\theta,0)=0 \tag{3.38b}$$

with$\Omega_\odot = 2.6\times 10^{-6}$ rad s^{-1} being the rotation rate of the present-day Sun. Symmetry considerations and regularity along the polar axis dictates the boundary conditions to be:

$$\frac{\partial\Omega}{\partial\theta}(r,0,t)=\frac{\partial\Omega}{\partial\theta}(r,\pi/2,t)=0, \tag{3.38c}$$

$$B(r,0,t)=0, \tag{3.38d}$$

$$B(r,\pi/2,t)=0, \tag{3.38e}$$

Once again the Weber-Davis wind solution of §I.4.3 is used, assuming $B_{\rm surf}\propto\Omega_{\rm surf}$, to compute the surface torque. The latter is actually modeled as a distributed sink term in the convective envelope, wherein solid-body rotation is enforced by artificially increasing the viscosity by six orders of magnitude. In seeking numerical solutions, it is convenient to work on non-dimensional forms of the governing equations. This is carried out by expressing all lengths in units of $R_\odot$, field strengths in units of B_0, and time in units of the Alfvén time t_A:

$$t_A=\frac{R_\odot}{u_A},\qquad u_A=\frac{B_0}{\sqrt{4\pi\rho_{\rm CE}}}, \tag{3.39}$$

where $\rho_{\rm CE}\sim 0.1\,{\rm g\,cm^{-3}}$ is the density at the core-envelope interface, and u_A is the Alfvén speed based on the *poloidal* field strength B_0. Assuming $B_0=1\,$G leads to $u_A\simeq 1\,{\rm cm\,s^{-1}}$ and $t_A\simeq 2000\,$yr. Note that t_A is much smaller than the angular momentum loss timescale, which varies from $\sim 10^6\,$yr for a rotation rate $50\,\Omega_\odot$ on the ZAMS, up to a few $10^9\,$yr for the present-day Sun. The solutions to the dimensionless equations depend only on the adopted values for the viscous and magnetic Reynolds numbers

$$\mathrm{R}_\nu=\frac{R_\odot u_A}{\nu}, \tag{3.40a}$$

$$\mathrm{R}_m=\frac{R_\odot u_A}{\eta}, \tag{3.40b}$$

which are (unconventionally) defined in terms of the Alfvén speed, rather than some other characteristic *fluid* velocity. Using microscopic values for ν ($\sim 10^2\,{\rm cm^2\,s^{-1}}$) and η ($\sim 10^4\,{\rm cm^2\,s^{-1}}$) then implies $\mathrm{R}_m\sim 10^7$ and $\mathrm{R}_\nu\sim 10^9$ for $B_0=1\,$G. Due to computational limitations, Charbonneau & MacGregor obtained solutions for

$$\mathrm{R}_\nu=10^6,\qquad \mathrm{R}_m=10^5, \tag{3.41}$$

which implies enhanced dissipation, yet is still large enough for the induction and Lorentz force terms to dominate the RHSs of eqs. (3.36), at least on the global length scale $\sim R_\odot$. Charbonneau & MacGregor computed solutions for the four poloidal field configurations of Fig. 3.6, and for poloidal fields strengths of 0.01, 0.1, 1 and 10 Gauss. Here we will discuss in some detail a subset of these solutions.

Figure 3.7 depicts the force balance in a series of D2-type solutions of various poloidal field strengths. The Figure is similar in format to Figure 3.4, in that it shows the time variations of the wind-mediated applied torque (curves labeled $\mathrm{d}J/\mathrm{d}t$), viscous stresses (labeled σ_ν) and magnetic stresses σ_B at the core-envelope interface, defined as

$$\sigma_B \equiv 2\pi r^3 \int_0^\pi B_r B_\phi \sin\theta \,\mathrm{d}\theta, \tag{3.42}$$

The first thing to notice is that viscous stresses are at all times much smaller than magnetic stresses. Nonetheless, the curves bear some similarity to those plotted on Figure 3.4 for purely viscous evolution. From a dynamical point of view the evolution can be broken into three more or less distinct phases:(∗):

(1) At first the induced toroidal field is too weak to produce a magnetic stress of sufficient magnitude to counteract the shear caused by the braking of the convective envelope. The shear at the core-envelope boundary then increases approximately linearly in time, which in turn causes the toroidal component to grow quadratically in time. The distribution of angular velocity is little affected outside of the boundary layer which forms below the base of the envelope. The characteristic timescale for this phase is the Alfvén time t_A defined above.

(2) Once magnetic stresses have grown to the point of being comparable to the angular momentum loss rate, the rotational profile begins to couple to the growing toroidal component. In poloidal magnetic configurations for which direct magnetic coupling exists between the core and envelope, this epoch is characterized by vigorous *phase mixing* throughout the radiative core, a process which leads to the rapid damping of any extant large-scale toroidal oscillations, completed after some $\sim 10^2$—10^3 Alfvén times[16].

(3) The interior then settles in a state of dynamical balance, in which the toroidal field maintains an amplitude such that on any spherical shell in the interior, the surface-integrated magnetic stresses nearly equal the (decreasing) surface torque.

You will have noticed (hopefully) that this scenario bears some striking similarities to that outlined in §3.4.3 for purely viscous models, except that now magnetic stresses are the main agent counteracting the applied torque[17].

The state of dynamical balance, as expressed by equation (3.42), has important consequences for the internal rotational evolution of the system. Because it is effectively the *product* of $|\mathbf{B}|_p$ and B_ϕ that must balance the applied torque, models

---

(∗) Animations of the D1 and D3 solutions covering the first two of these phases can be viewed on the course Web Page

[16] Problem (3.2) has you explore the nature of phase mixing in the context of a much simpler problem in Cartesian geometry.

[17] Would this be true of all four magnetic configurations shown on Figure 3.6?

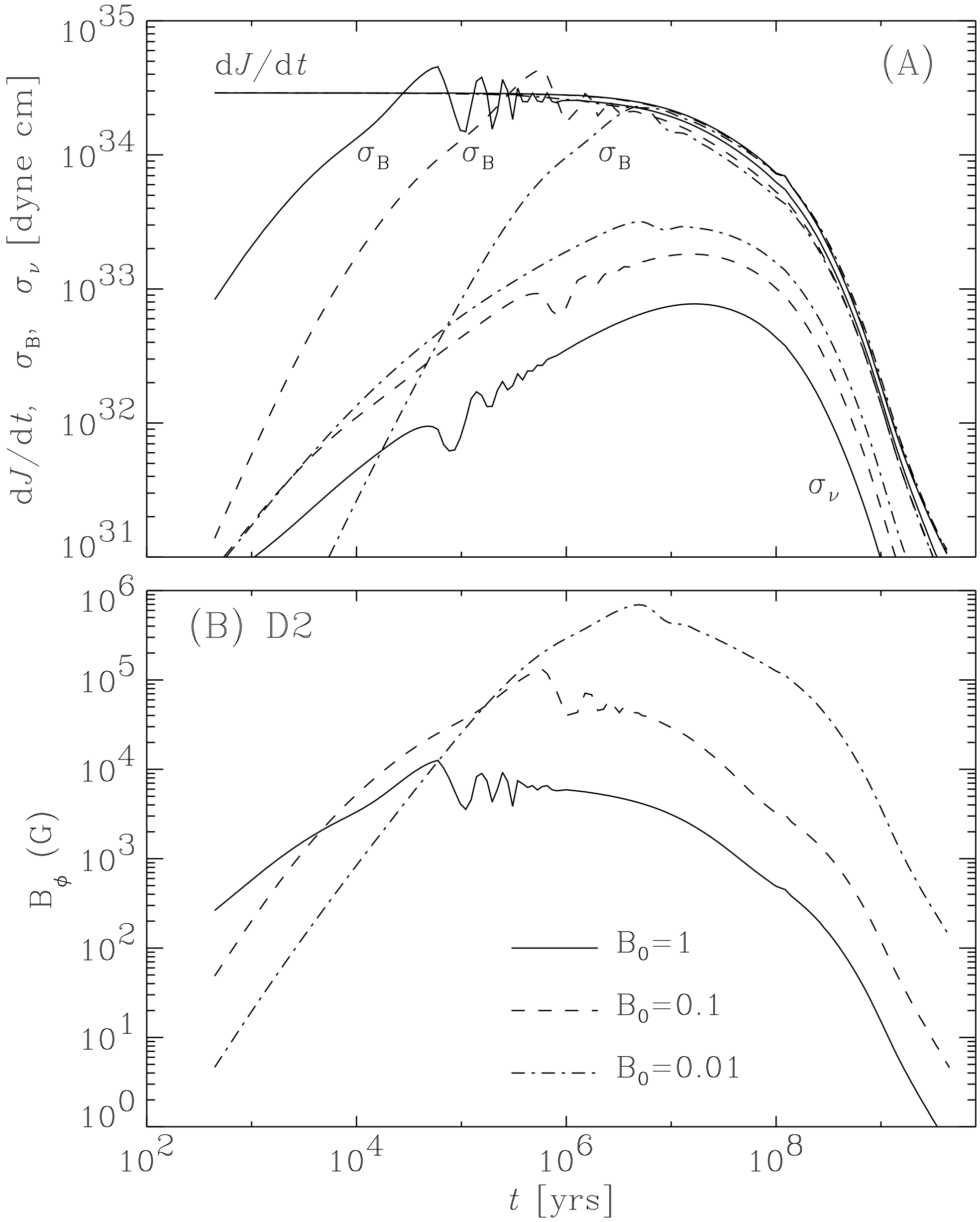

Figure 3.7: Dynamics of the magnetized spin-down model. Panel (A) shows the evolution of the applied torque ($\mathrm{d}J/\mathrm{d}t$), magnetic stresses (σ_B) and viscous stresses (σ_ν) are shown for three D2 solutions of varying poloidal field strength, as labeled. Stresses are evaluated at the core-envelope interface (cf. eqs. [3.26] and [3.42]). The "wiggles" seen in the time interval 10^5—10^6 yr are real, and correspond to the epoch of phase mixing, as described in the text. Part (B) shows the corresponding evolution of the latitudinally averaged toroidal field at the core-envelope interface.

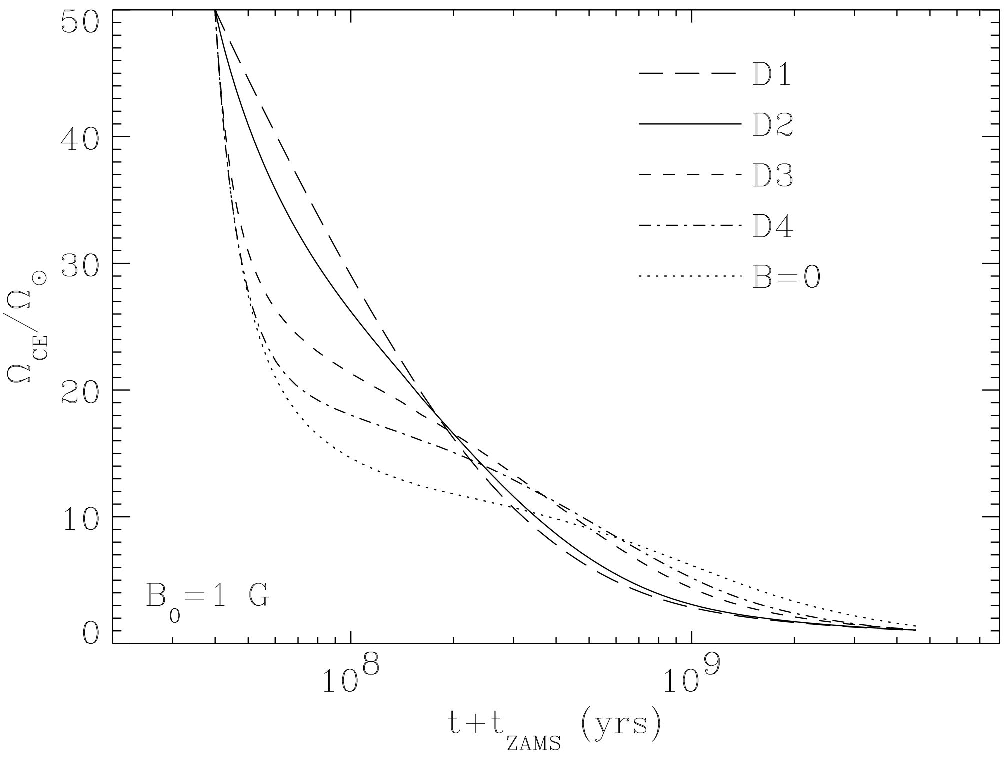

Figure 3.8: Time-evolution of the surface rotation rate for the various poloidal field configurations of Figure 3.6. The dotted line corresponds to the evolution of a non-magnetic configuration, i.e., evolution in response to purely viscous coupling as parametrized by the viscous Reynolds number R_ν. The zero point of time is the age of arrival on the ZAMS (4×10^7 yr) for the solar model used here. Note the convergence of surface rotations rate at $t \gtrsim 10^9$ yr.

with weaker poloidal fields simply generate stronger B_ϕ during phase (1) described above, until (3.42) is approximately satisfied. This is clearly seen on panel (B) of Figure 3.7. The quasi-static evolutionary phase (3), typically of longest duration, becomes then insensitive to the poloidal field strength. *Consequently, at late epochs the evolution of both surface and internal rotation is largely insensitive to the adopted poloidal field strength.*

Figure 3.8 illustrates the evolution of the surface rotation in the course of spin-down. All these solutions were obtained for the same value of R_ν and R_m, and so are characterized by the same level of viscous coupling in the interior. Comparing to Fig. (3.3), one sees that increasing magnetic coupling at the core-envelope interface (D4$\rightarrow$D1) roughly mimics enhanced viscous coupling, in the sense that more strongly coupled models (D1 and D2, or higher $\nu_{\rm eff}/\nu$ on Fig. 3.3) spin down more slowly than less strongly coupled models (D3 and D4), and end up rotating slightly more slowly by the solar age. This is also the case for the internal differential rotation. Figure 3.7 shows the evolution of the quantity

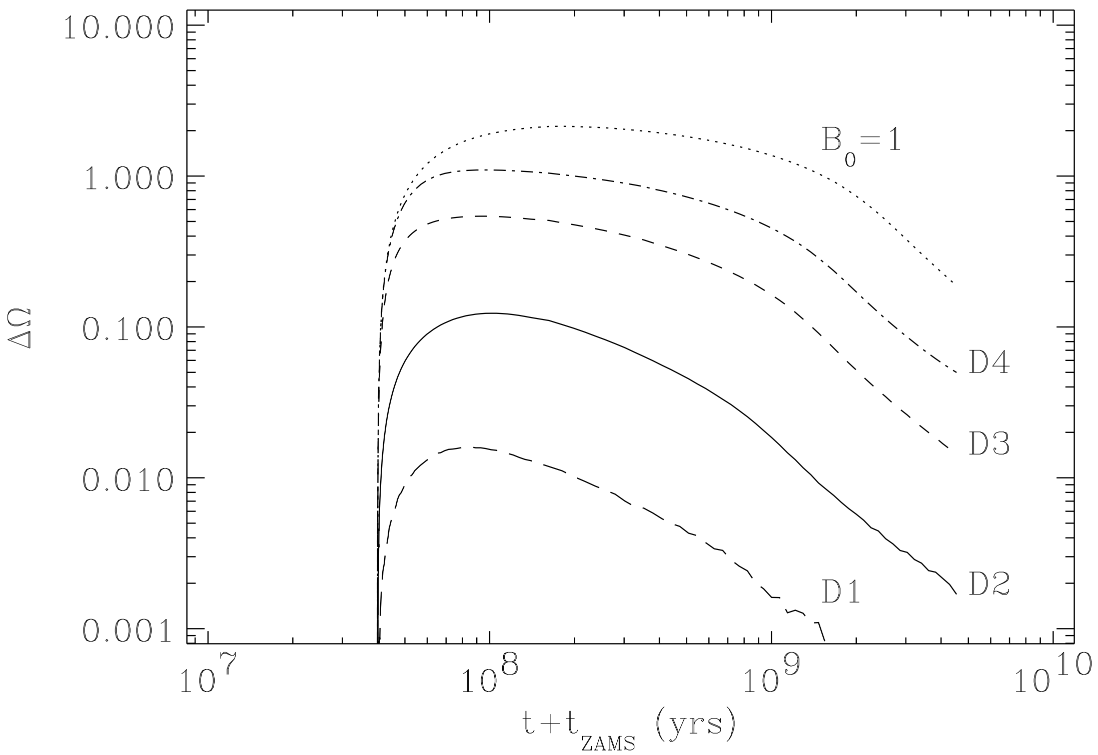

Figure 3.9: Time-evolution of the internal differential rotation, as defined by the quantity $\Delta\Omega$ (see eq. [3.43]), for the four poloidal field configurations shown on Fig. 3.6, all at strength $B_0 = 1\,$G. The geometry of the poloidal field affects the magnitude of internal differential rotation to a much larger degree than its strength (see text).

$$\Delta\Omega(t) = \frac{3}{2R_{\rm CE}^3}\int_0^\pi \int_0^{R_{\rm CE}} \left| \frac{\Omega(r,\theta,t) - \Omega_{\rm CE}(t)}{\Omega_{\rm CE}(t)} \right| r^2 \sin\theta {\rm d}r{\rm d}\theta, \tag{3.43}$$

essentially a global measure of internal differential rotation. The dotted line is a purely viscous solution, computed for the same value of R_ν as the magnetized models. Clearly the inclusion of magnetic fields greatly reduces the degree of internal differential rotation at all evolutionary epochs, the more so the greater the core-envelope magnetic coupling.

In the context of the observational constraints identified at the end of §1.1, important conclusions can be drawn on the basis of the Charbonneau & MacGregor model calculations:

(1) The present-day solar surface rotation rate is insensitive to the assumed strength or geometry of the internal poloidal magnetic field;

(2) At later evolutionary epoch (specifically, phase 3 above), the internal differential rotation is insensitive to the assumed poloidal field strength, but is

sensitive to the assumed degree of magnetic coupling at the core-envelope interface;

(3) The rapid spin-down experienced by solar-type stars following their arrival on the ZAMS can only be accomodated in models having little or no magnetic coupling at the core-envelope interface (i.e., D3 or D4).

(4) Except for D4-type geometries and very low internal poloidal field strengths ($B_0 \lesssim 10^{-3}\,$G), all magnetized models produced a level of differential rotation at the solar age that is within the bounds inferred from helioseismology.

An important caveat is in order: because the calculations are started on the ZAMS, it is yet unclear whether point (3) would still hold if the toroidal field were given the chance to grow in the course of pre-main sequence evolution, during which significant internal differential rotation may well materialize as a consequence of contraction. Extending the Charbonneau & MacGregor calculations to the pre-main sequence is the next logical step in this type of calculations, and one that is yet to be undertaken[18]

3.5.3 The light element abundances, again!

The internal differential profiles produced by the above calculations can be used to compute *a posteriori* the evolution of light element abundances, using whatever prescription for $D_T(\Omega)$ one wishes to experiment with. Figure 3.10 is taken from recent work by G. Barnes *et al.*, who did precisely this.

Because the internal differential rotation profiles arising from the magnetized spin-down calculations are essentially two dimensional (i.e., $\Omega \to \Omega(r,\theta)$, a 2-D equivalent of the transport equation (3.23) must be solved:

$$\rho\frac{\partial c}{\partial t} = \frac{1}{r^2}\frac{\partial}{\partial r}\left[\rho D_r r^2 \frac{\partial c}{\partial r}\right] + \frac{\partial}{\partial \mu}\left[\frac{\rho D_\mu (1-\mu^2)}{r^2}\frac{\partial c}{\partial \mu}\right] + \rho S c \tag{3.44}$$

where $\mu \equiv \cos\theta$, S is again the nuclear reaction rate appropriate for the chemical species under consideration, and D_r and D_μ and vertical and horizontal diffusion coefficients. These are assumed to take the form

$$D_r = D_0 \left|\frac{\partial \Omega}{\partial r}\right|, \qquad D_\mu = \frac{D_0}{r}\left|\frac{\partial \Omega}{\partial r}\right|, \tag{3.45}$$

where D_0 is some numerical coefficient, in practice an adjustable parameter of the model. We will restrict our attention here to one important aspect of the Barnes *et al.* calculations, namely the dependence of light element depletion on the assumed strength and geometry of the underlying poloidal field. Figure 3.10 shows a series of Li (and a few Be) abundance evolution curves in a solar model, for evolving internal differential rotation profiles $\Omega(r,\theta,t)$ computed as in §3.5.2 for the D1 and D3 configurations (cf. Fig. 3.6[A] and [C]) at various poloidal field

[18] Anybody interested?

strengths. For each configuration, the coefficient D_0 in eq. (3.45) was adjusted so that the present-day solar Li depletion is recovered for the $B_0 = 1\,\mathrm{G}$ model. Note that the use of that same D_0 value leads to a level of Be depletion in the D3 model that is in good agreement with observations. Then, keeping D_0 fixed, solutions were computed for other field strengths.

It is quite clear from Figure 3.10 that the light element abundances are extremely sensitive to the assumed internal poloidal field strength. Firthermore, matching the present-day solar Li abundance requires markedly different values of D_0 for the D1 and D3 configurations, indicating that light element depletion is a sensitive function of the assumed geometry of the underlying poloidal magnetic field. This is in marked contrast to angular momentum, as discussed previously. This important difference can be traced to the fact that in contrast to angular momentum, it is far harder to "hide" Li deep in the envelope at early time, for subsequent resurfacing at later epochs (although the D1 configuration manages to do so to some extent). This is because once Li is destroyed by nuclear reactions, it is gone for good, and the size of the buffer zone where Li can be stored (but not burned) below the envelope is rather restricted (cf. Fig. 3.2).

There are a number of fundamental uncertainties in this whole approach. Perhaps the most pressing is our complete lack of knowledge concerning the transport properties of magnetohydrodynamic turbulence. The (time-dependent) diffusion coefficients implied by the D_0 values adopted here end up being two to three orders of magnitudes above microscopic values. This level of enhancement is actually cmparable to that implicitly implied by the R_ν and R_m values adopted in the Charbonneau & MacGregor calculations for numerical reasons. So in a restricted sense there is no inconsistency there. However, particle transport by small-scale turbulence is very likely to be affected by the presence of magnetic fields, especially early in the evolution when the toroidal field strength is in excess of 100kG for $B_0 = 1\,\mathrm{G}$. With the purely hydrodynamical transport problem still not adequately treated, it is very unlikely that its MHD equivalent will be cracked any time soon.

To further complicate matters, the interaction of magnetic fields with differential rotation can in itself lead to global instability. An example of this possibility will encountered in the following chapter, the bibliography of which contains references to the literature on this aspect of the problem.

Such considerations notwithstanding, if the results described here are taken at face value (one big leap of faith), then to the four main conclusions listed at the end of §3.5.2 we can add:

(5) The present-day solar light element abundances are very sensitive indicators of both the strength and geometry of any large-scale poloidal magnetic field pervading the solar radiative interior.

Once again however, calculations need to be started on the pre-main sequence, rather than on the ZAMS, before detailed comparison to light element abundances in young clusters can be modeled with confidence.

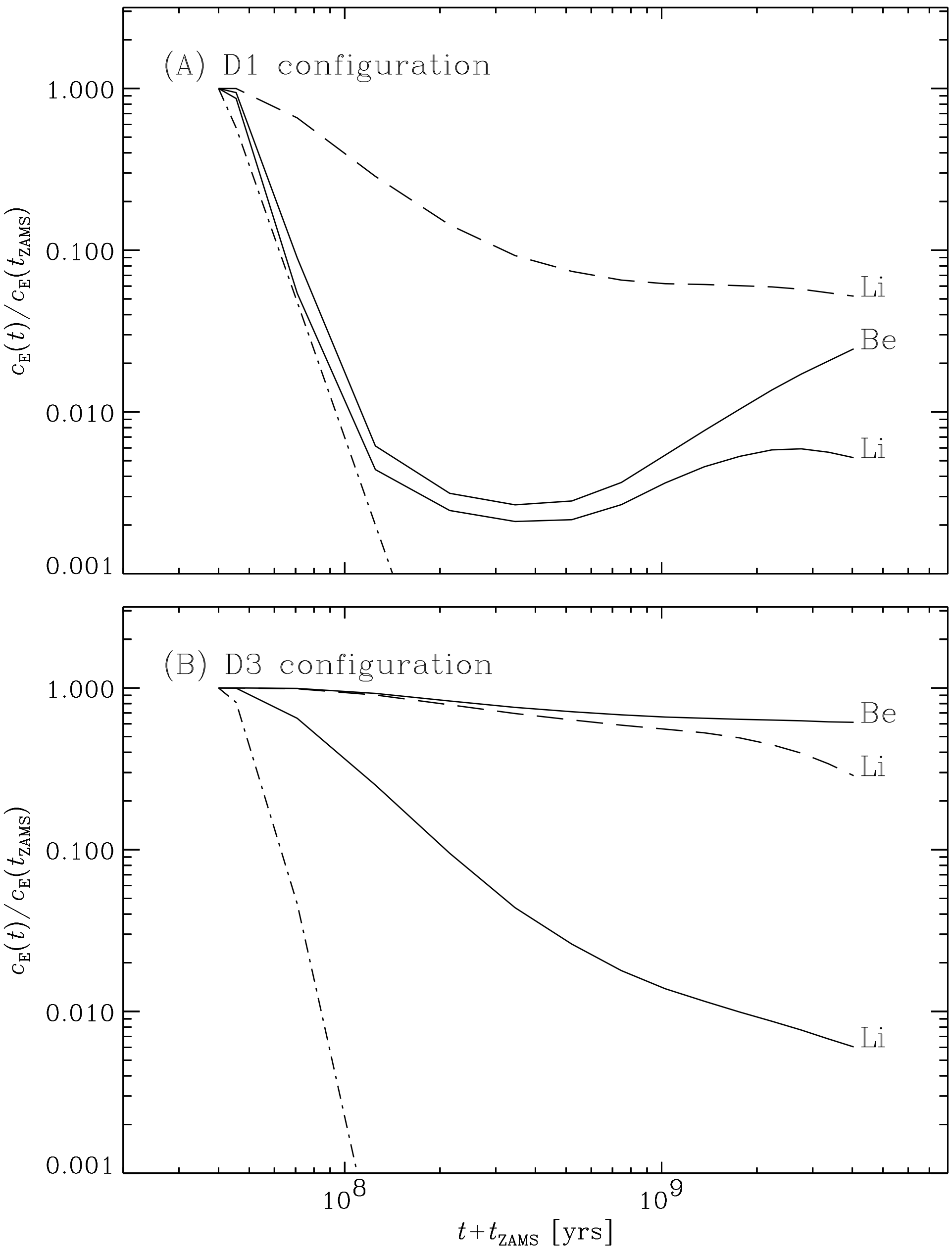

Figure 3.10: Evolution of light element abundances in response to turbulent mixing, in a model where internal angular momentum redistribution occurs primarily via magnetic stresses. Solutions are shown for the D1 and D3 poloidal configuration of Figure 3.5, with the curves coded according to poloidal field strengths: dash-dotted, solid, and dashed lines correspond $B_0 = 0.1, 1, 10$ Gauss respectively. The value of D_0 has been adjusted so that the Li depletion is reproduced in the $B_0 = 1$ G model (requiring $D_0 = 3.0$ and $2.6 \times 10^{-2}\text{cm}^3$ for D1 and D3, respectively), but then held fixed at that value as B_0 is varied.

3.6 Closure

One final point, applicable to all models discussed in this chapter, is worth emphasizing as we close this chapter. Whether it is magnetic stresses or viscous-like turbulent transport that are the main agent responsible for the internal redistribution of angular momentum in the course of the solar spin-down, the interior always tends to adjust itself —i.e., producing a strong enough toroidal field or angular velocity gradient— to approximately equilibrate the wind-mediated applied torque. This means that a proper calculation of angular momentum loss in a magnetized wind is *essential* even to the modeling of the *internal* solar rotation. This being said, try to think back at the various simplifying assumptions made in constructing the Weber-Davis model, and decide for yourselves how seriously you must take some of the results discussed in this chapter.

Problems

(3.1) This problem requires that you go to the course Web Page:

`http://www.hao.ucar.edu/public/education/astr7500.html`

click on Animation Gallery, and find the magnetized spin-down animations listed under §II.3.5. Study the two animations and answer the following questions.

(a) Estimate a global Alfvén time for each solution, i.e., the time required for the original Alfvén wavefront originally emanating from the core-envelope interface to reach the center. How does this compare to the estimate for τ_B obtained in §3.1? How do you explain the differences, if any?

(b) Estimate the length, in years, of the epoch of phase mixing. How does this compare to the Alfvén time?

(c) Estimate the magnitude of the toroidal field produced in the D1 and D3 configurations at the peak of phase mixing. In which configuration is it strongest? why?

(d) Which of the two configurations (D1 or D3) ends up producing the strongest toroidal field in the interior, once phase mixing has ended? How do you explain this?

(e) How do you explain the peculiar zigzag shape of the u_ϕ isocontours at the end of the D3 animation?

(3.2) This problem lets you explore some aspects of phase mixing, in the context of a simple analytical model. Working in cartesian coordinates, consider an inviscid incompressible perfectly conducting fluid contained betwen two infinite parallel plates located at $z = \pm L$, across which exists a vertical (z-oriented), imposed magnetic field with strength a function of the y-coordinate, i.e., $\mathbf{B} = (0, 0, B_z(y))$. At $t = 0$ a perturbation $\mathbf{U} = (U_x(z), 0, 0)$, with $U_x(z) = 1 - (z/L)^2$ is impulsively applied in the positive x-direction.

(a) Show that the shear corresponding to the imposed flow profile $U_x(z)$ will induce a magnetic field in the x-direction. Assuming $\mathbf{U}$ to be fixed, obtain an expression for the growth, as a function of time, of B_x.

(b) Show that the Lorentz Force associated with the growing B_x is such that it always opposes the applied shear, i.e., that it acts in the negative x-direction.

(c) Manipulate the x-components of the induction equation and equation of motion into a single differential equation for the time variation of B_x as a function of B_x and B_z. What does this equation remind you of?

(d) Write down a general solution to the differential equation you obtained in (c).

(e) Plot B_x as a function of y in the $z = 0$ plane, for a series of selected times (> 0). Fourier transform each curve, and plot the resulting power spectrum as a function of time. Calculate the time required for the peak in the power spectrum to reach wavenumber k.

(f) What do you think will happen if we now account for the fact that the fluid is not exactly perfectly conducting or inviscid?

Bibliography

Equations (3.6) and (3.7) for the kinematic viscosity are are taken from

Spitzer, L. Jr. 1962, *Physics of fully ionized gases*, John Wiley/Interscience.

Good introductory discussions of the Eddington-Sweet rotationally-induced meridional circulation can be found in

Tassoul, J.-L. 1978, *Theory of Rotating Stars*, Princeton: Princeton University Press, chap. 7 and 8,
Kippenhahn, R., & Weigert, A. 1990, *Stellar Structure and Evolution*, New York: Springer, chap. 42.

At a more technical level, see

Tassoul, J.-L., & Tassoul, M. 1982, ApJS, 49, 317,
Tassoul, M., & Tassoul, J.-L. 1995, ApJ, 440, 789,

The following are a few classical papers on the topic:

von Zeipel, H. 1924, MNRAS, 84, 665,
Eddington, A.S. 1925, Observatory, 48, 73,
Vogt, H. 1925, Astr. Nach., 223, 229,
Sweet, P.A. 1950, MNRAS, 110, 548,
Mestel, L. 1953, MNRAS, 113, 716.

On the spin-up/down of viscous fluids by Ekman pumping, see

Greenspan, H.P. 1968, *The Theory of rotating fluids*, Cambridge University Press [reprinted 1990 by Breukelen Press].

Watch also for a new book by Jean-Louis Tassoul, entitled *Stellar Rotation*, to be published by Princeton University Press in 1998. The book includes a clear and thorough discussion of rotating fluids in the geophysical and astrophysical context. Ekman layer models for the solar core-envelope interface are discussed in

Clark, A., Clark, P.A., Thomas, J.H., & Lee, N.-H. 1971, J. Fluid Mech., 45, 131,
Clark, A., Thomas, J.H., & Clark, P.A. 1969, *Science*, 164, 290,
Howard, L.N., Moore, D.W., and Spiegel, E.A. 1967, *Nature*, 214, 1297.

The first reliable abundance determinations of Li, Be and B in the Sun were carried out by

Greenstein, J.L., & Richardson, R.S. 1951, ApJ, 113, 536 (Li)
Greenstein, J.L., & Tandberg-Hanssen, E.S. 1954, ApJ, 119, 113 (Be)
Kohl, J.L., Parkinson, W.H., & Withbroe, G.L. 1977, ApJL, 212, 101 (B)

The solar and meteoritic light element abundances of Table 3.1 are taken from

Anders, E., & Grevesse, N. 1989, Geo. Cos. Acta, 53, 197.

The evolution of light element abundances in the Sun and solar-type stars in response to rotationally-induced turbulent mixing has been considered by a number of authors, from widely varying points of view. For recent entry points into that literature, see

Schatzman, E., & Baglin, A. 1991, Å249133,
Zahn, J.-P. 1992, Å265115.

Purely viscous (with enhanced viscosities) models of the solar internal differential rotation were considered, among others, by

Tassoul, J.-L., & Tassoul, M. 1989, Å213397

Although their treatment differs from that of §3.4.3 herein in that they assume Skumanich's $t^{-1/2}$ relation to hold at all times, they reach essentially identical conclusions as we do here. For the various incarnations of the Yale models applied to the Sun, see

Endal, A.S., & Sofia, S. 1981, ApJ, 243, 625,
Pinsonneault, M.H., Kawaler, S.D., Sofia, S., & Demarque, P. 1989, ApJ, 338, 424,
Chaboyer, B., Demarque, P., & Pinsonneault, M. 1995, ApJ, 441, 865.

For more details on the shear instability criterion and associated transport coefficients used in the Yale models, see

Zahn, J.-P. 1993, in *Astrophysical Fluid Dynamics, Les Houches 1987*, eds. J.-P. Zahn & J. Zinn-Justin, Elsevier Science Publishers, chap. 8, §3.

The results discussed in §3.5 are taken directly from

Charbonneau P., & MacGregor K.B. 1993, ApJ, 417, 762

but for a somewhat different point of view on the topic see

Mestel, L., & Weiss, N.O. 1987, MNRAS, 226, 123,
Li, J., & Cameron, A.C. 1993, MNRAS, 261, 766.

One specific uncertainty with models that assume the solar radiative interior to be magnetized has to do with the *stability* of such large-scale magnetic fields. This is an immense and confusing topic. Those interested should start with

Pitts, E., & Tayler, R.J. 1985, MNRAS, 216, 139,
Balbus, S.A., & Hawley, J.F. 1994, MNRAS, 266, 769,

as a good entry points into the technical literature on this topic. The results for light element discussed in §3.5.3 are taken from

Barnes, G., Charbonneau P., & MacGregor K.B. 1997, submitted to *The Astrophysical Journal* (preprint available upon request).

The following papers focus on a simple model for internal angular momentum redistribution. The model catches many important features of the more elaborate ones discussed in this chapter, yet is simple enough to allow extensive parametric studies:

MacGregor, K.B., & Brenner, M. 1991, ApJ, 376, 204
Keppens, R., MacGregor, K.B., & Charbonneau, P. 1995, Å294469

4. THE SOLAR CONVECTIVE ENVELOPE

SCHÜLER: Kann Euch nicht eben ganz verstehen.
MEPHISTOPHELES: Das wird nächstens schon besser gehen.

Johann Wolfgang von Goethe
Faust I (1808)

Thermally-driven convection occurs in the outer $\sim 30\%$ in radius of the Sun, because of the rapid increase in opacity ($\bar{\kappa}$) brought about by the recombination of Hydrogen and, near the surface, the production of the H- ion. Deeper in the energy flux is carried by radiation. In the diffusion limit, the radiative flux is given by:

$$\mathcal{F}_r = -\frac{4acT^3}{3\bar{\kappa}}\nabla T \tag{4.1}$$

Clearly, with the net radiative flux fixed by the thermonuclear energy release in the inner core, a large increase in $\bar{\kappa}$ must be compensated by a corresponding increase in the temperature gradient. In the radiative regime, the maximal temperature gradient that can be tolerated is the adiabatic temperature gradient

$$(\nabla T)_{\rm ad} \equiv \nabla_{\rm ad} T = -\frac{p}{\rho c_p T}\left(\frac{\partial \ln \rho}{\partial \ln T}\right)_p \equiv \left(\frac{p}{T}\frac{{\rm d}T}{{\rm d}p}\right)_S \tag{4.2a}$$

If $\nabla T > (\nabla T)_{\rm ad}$, the stratification becomes unstable with respect to small radial displacement of fluid elements, and large-scale convective motions set in. The *convective flux* of energy associated with these motions is given by an expression of the form

$$\mathcal{F}_c = \rho u c_p (\nabla T - \nabla_{\rm ad} T) \tag{4.2b}$$

where u is the net upward convective velocity, and the quantity in parentheses is the temperature excess advected by the convective motions. The quantity $\rho u c_p$ can be interpreted as a convective "heat conductivity" coefficient (χ_c) analogous to the radiative conductivity χ_R (cf. eq. [3.16]). In the parameter regime characterizing the solar envelope, this convection is turbulent, with flow patterns assuming a wide range of spatial scales, and turbulent velocities intermittently exceeding the speed of sound near the surface(∗).

These turbulent fluid motions carry not only heat, but also momentum. Their contribution to angular momentum balance in the solar convective envelope turns out to be quite important.

Direct observation of the solar surface reveals a large-scale latitudinal (i.e., θ-directed) differential rotation, which is usually parameterized as

$$\frac{\Omega(\theta)}{\Omega_{\rm eq}} = 1 - a_2 \cos^2\theta - a_4 \cos^4\theta \tag{4.3}$$

where $\Omega_{\rm eq}$ is the equatorial ($\theta = \pi/2$) rotation rate. Under this normalization, the upper portions of the radiative core have a rotation rate $\simeq 0.94\Omega_{\rm eq}$. The Doppler determination the surface differential rotation (cf. §1.1) implies $a_2 = 0.1264$ and $a_4 = 0.1591$. Helioseismology has revealed that this horizontal gradient is maintained throughout the bulk of the convective envelope, with little radial variation except very near the surface.

In addition, Doppler observations have revealed the existence of an equator-to-pole surface *meridional flow*, which is typically parameterized as

$$U_\theta(\theta) = u_2 \sin\theta\cos\theta \tag{4.4}$$

The most recent observational fit yields $u_2 = -54 \pm 1\,{\rm m\ s}^{-1}$. This flow is much slower than the zonal differential flow, which has pole-equator amplitude of over half a kilometer per second (cf. eq. [4.3]). Obviously this flow must close within the solar interior, but is far too slow to be detectable with current helioseismic data and techniques[1].

In this chapter we will focus on the physical origin of eq. (4.3), with little attention paid to the meridional flow except for its capacity to transport angular momentum. Likewise, we will not consider the many fascinating dynamical aspects of turbulent convection, beyond their ability to produce large-scale stresses that can affect rotation. We begin (§4.1) with some implications of eq. (4.3) for global angular momentum balance. We continue (§4.2) by considering the application of mean-field theory to the turbulent convective envelope, which allows us to parameterize the action of small-scale turbulents motion on the large-scale differential rotation. We then construct a few simple mean-field models of envelope rotation (§4.3).

In terms of the overall philosophy of the course we have a bit of a problem here. Rotating convection is not something which lends itself readily to the construction of simple models. Consequently, in terms of style this chapter departs significantly

(∗) Links to various animations of turbulent convection have been set up under the Animation Gallery section of the Course Web Page.

[1] Fifty meters per second does not seem that slow... but do you think that this flow speed is maintained within the interior? why?

from the preceding and following ones. Rather than constructing simple models, we have to describe complex ones, hopefully in a manner that will adequately clarify some (though certainly not all) important physical aspects of the problem.

4.1 Angular momentum in the solar convective envelope

Let us consider the angular momentum content ΔJ of a thin spherical shell (radius r, thickness Δr, and average density ρ) within the convective envelope. Equation (1.3) reduces to

$$\Delta J = 2\pi\rho r^4 \Delta r \int_0^\pi \Omega(r,\theta)\sin^3 \mathrm{d}\theta \tag{4.5}$$

Here we have $\Omega(r,\theta) \to \Omega(\theta)$, as given by eq. (4.3), so that

$$\Delta J = 2\pi\rho r^4 \Delta r \Omega_{\mathrm{eq}} \int_0^\pi \left[\sin^3\theta - a_2\cos^2\theta\sin^3\theta - a_4\cos^4\theta\sin^3\theta\right] \mathrm{d}\theta \tag{4.6}$$

Problem (4.1) asks you to verify that the integral on the RHS of this expression is equal to 1.2814. In the case of *rigid* rotation, what would the angular velocity of the shell have to be to contain the same amount of angular momentum? The answer is $0.961\,\Omega_{\mathrm{eq}}$.

The interesting thing about this number is that it is very close to the rotation rate of the upper part of the (rigidly rotating) radiative core. This indicates that there may well be very little *net* vertical exchange of angular momentum between the radiative core and convective envelope. Of course, locally vertical exchange can occur, if only by ordinary viscosity. Given the latitudinal profile of envelope differential rotation, viscosity can be expected to transfer angular momentum from the envelope to the core at low latitudes, and from the core to the envelope at high latitudes. While this plays a crucial role in the dynamics of the rotational transition layer in the upper part of the radiative core, (the so-called “tachocline”), its role in the angular momentum balance within the envelope is less clear. Within the envelope, viscous (or viscous-like) stresses can be expected to lead to angular momentum transport from high to low latitudes. Clearly, some mechanism is required to offset this angular momentum flow (and whatever poleward flow that may be mediated via the tachocline).

To a good degree of approximation, the solar differential rotation is in a steady-state[2]. Based on our dicussion in §3.1, and neglecting magnetic fields, one

[2] Superimposed on the largely steady solar differential rotation, surface observations reveal a global pattern of low amplitude ($\sim 5\,\mathrm{m\ s}^{-1}$) azimuthal velocity variation, travelling from pole to equator in approximately 20 years, dubbed *torsional oscillation*. The approximate coincidence of this period with the full period of the solar magnetic cycle suggests that torsional oscillations represent a magnetic perturbation to a global force balance that is largely hydrodynamical in nature (see references in the bibliography).

should think that this (axisymmetric) steady-state must be described by something like:

$$\rho \mathbf{U}_p \cdot \nabla(\varpi^2 \Omega) = \nabla \cdot [\rho \varpi^2 \nu_{\text{eff}} \nabla \Omega], \tag{4.7}$$

indicating that the latitudinal viscous stresses must be balanced by advection of angular momentum by a large-scale meridional flow of some sort, if a steady-state is to be maintained at all. Also, it is clear from eq. (4.7) that in the absence of meridional circulation ($\mathbf{U}_p = 0$) and boundary stresses, the only acceptable steady-state is solid-body rotation ($\nabla\Omega = 0$). A first (naive) estimate for ν_{eff} can be constructed via the mixing length theory (MLT) of convection[3], by forming the product of MLT estimates for the mixing length ℓ_c and associated convective velocity u_c:

$$\nu_{\text{eff}} \sim u_c \ell_c \sim 10^{10} - 10^{12}\,\text{cm}^2\,\text{s}^{-1} \tag{4.8a}$$

The corresponding dissipation timescale (eq. [3.3a]) for length scales or order $R_\odot$ is then

$$\tau_\nu = R_\odot^2 / \nu_{\text{eff}} \simeq 10^6 - 10^4\,\text{yr}. \tag{4.8b}$$

A large scale meridional flow must have speed $\sim 10^{-3}$—10^{-1} cm s^{-1} to be able to advect angular momentum on similar length and time scales. This does not sound unreasonably high, especially in view of the fact that a meridional flow of speed $\sim 10\,\text{m s}^{-1}$ is observed at the solar surface. However we have on our hands a problem of a geometrical nature. With a purely latitudinal angular velocity gradient (i.e., $\nabla\Omega \to \partial\Omega/\partial\theta$), equation (4.7) reduces to

$$\frac{U_\theta}{r}\frac{\partial(\varpi^2\Omega)}{\partial\theta} = \frac{\partial}{\partial\theta}\left[\rho \sin^2\theta \nu_{\text{eff}} \frac{\partial\Omega}{\partial\theta}\right] \tag{4.9a}$$

while the lack of radial gradient in Ω can only be accomodated in a steady-state provided that

$$U_r \frac{\partial(r^2\Omega)}{\partial r} \equiv U_r \times (2r\Omega) = 0, \tag{4.9b}$$

which clearly requires $U_r = 0$, meaning a purely latitudinal flow, which doesn't conserve mass in spherical geometry. A moment of reflection will reveal numerous ways out of this quandary. One may try to account for the fact that the angular velocity gradient in the solar convective envelope is not strictly latitudinal, and construct a flow that satisfies eq. (4.7). Introducing local angular momentum exchange between the core and envelope is also a possibility, but this actually worsens the problem.

While meridional flows and/or local vertical exchange may well contribute to the balance of angular momentum in the solar convective envelope, the physical mechanism responsible for maintaining the observed latitudinal angular velocity gradient has its origin in the turbulent nature of the envelope, and so has no real

---

[3] An excellent introduction to this topic may be found in Hansen & Kawaler's textbook *Stellar Interiors* (see bibliography at the end of chapter 1).

counterpart in the processes considered in the preceding chapter. The "turbulent" viscous stresses, as described by the RHS of eq. (4.7) with some mixing length estimate for $\nu_{\rm eff}$, amount to saying that the flow of angular momentum associated with the small-scale turbulent fluid motions is always in the direction opposite to the *large-scale* angular velocity gradient. This is a rather drastic assumption, that needs to be examined in greater depth before we strain our brains trying, for example, to cook up a meridional flow satisfying eq. (4.7).

4.2 Reynolds Stresses in turbulent fluids

In principle, the equations of motion, together with appropriate boundary and initial conditions, contain all the information necessary to follow the evolution of a fluid system in a (nonlinear) turbulent state. In practice however, the range of spatial and temporal scales to be accounted for is so wide that even the largest numerical simulations of convective turbulence in the Sun must either focus on a very restricted spatial domain ("turbulence in a box"), or consider parameter regimes far removed from the real Sun ("turbulent molasse"). Insight into the behavior of turbulent fluids can however be obtained via a mathematical procedure known as *mean field theory.*

4.2.1 Mean-field theory

Mean-field theory begins by *assuming* that all field quantities (a, say) can be divided into a large-scale, mean component $\bar{a}$, and a small-scale, fluctuating component a':

$$a = \bar{a} + a'. \tag{4.10}$$

Consider then an averaging operator, either temporal or spatial[4]:

$$\langle A \rangle = \frac{1}{\lambda^3} \int_V A d\mathbf{x}, \qquad \text{or} \qquad \langle A \rangle = \frac{1}{\tau} \int A dt. \tag{4.11}$$

The fundamental assumption underlying mean-field theory is that there exist a separation of scales between $\bar{a}$ and a' such that, for some suitably chosen intermediate temporal (τ) or spatial ($\lambda \equiv V^{1/3}$) scale, one has $\langle a \rangle = \bar{a} + \langle a' \rangle$.

In the context of turbulent flows, this fundamental assumption is formulated in terms of mass conservation; one assumes that the turbulent component of the flow does not leads to any mass transport when averaged spatially or temporally:

$$\langle \rho u'_k \rangle = 0, \qquad k = 1, 2, 3. \tag{4.12a}$$

Note that (4.12a) holds independently for each velocity component, and implies something very different from setting $\langle \rho' \rangle = 0$, or $\langle u'_k \rangle = 0$ (or both). In fact,

[4] The equivalence of temporal and spatial averages can be taken as a theorem defining *ergodic systems.* This theorem holds true only for stationary flow. Can you think of a situation where it would not apply?

the mass conservation statement (4.12a) can be used to *define* the mean velocity components as

$$\bar{u}_k \equiv \frac{\langle \rho u_k \rangle}{\bar{\rho}}. \tag{4.12b}$$

and of course, we have

$$\langle \bar{u}_k \rangle = \bar{u}_k, \qquad \langle \bar{\rho} \rangle = \bar{\rho}, \tag{4.12c}$$

and so on, in view of the fundamental assumption of mean-field theory. This also means that barred quantities can be pulled out of the averaging operator, e.g.,

$$\langle \rho \bar{u}_k \rangle = \bar{u}_k \langle \rho \rangle . \tag{4.12d}$$

finally, it should be clear from eqs. (4.11) that for any two quantities a and b,

$$\langle a + b \rangle = \langle a \rangle + \langle b \rangle \tag{4.12e}$$

and that the operations of averaging and differentiation commute:

$$\frac{\partial \langle a \rangle}{\partial x} = \left\langle \frac{\partial a}{\partial x} \right\rangle . \tag{4.12f}$$

Now, the momentum equation for the net flow $\mathbf{u}$, in component form, can be written as

$$\frac{\partial}{\partial t}(\rho u_i) + \frac{\partial}{\partial x_k}(\rho u_i u_k) = \rho g_i - \frac{\partial p}{\partial x_i} + \frac{\partial \tau_{ik}}{\partial x_k} \tag{4.13}$$

where summation on repeated indices applies. Now we insert eq. (4.10) into (4.13), and apply the averaging operation to the resulting expression. Problem (4.2) leads you to show that, by making extensive and repeated use of our fundamental assumption (eq. [4.12a]), the result of this procedure is

$$\frac{\partial}{\partial t}(\bar{\rho}\bar{u}_i) + \frac{\partial}{\partial x_k}(\bar{\rho}\bar{u}_i\bar{u}_k) = \bar{\rho} g_i - \frac{\partial \bar{p}}{\partial x_i} + \frac{\partial \bar{\tau}_{ik}}{\partial x_k} - \frac{\partial \langle \rho u'_i u'_k \rangle}{\partial x_k} \tag{4.14}$$

where we have further assumed the body forces to be unaffected by turbulence. It is a remarkable fact that eq. (4.14) for the mean flow is identical to the original momentum equation for the full flow (eq. [4.13]), except for the presence of the last term on the RHS of eq. (4.14). This term looks like the divergence of a tensor σ_{ik} if we define the latter as

$$\sigma_{ik} = - \langle \rho u'_i u'_k \rangle \tag{4.15}$$

which is called the *Reynolds stress tensor.* These extra contributions to the RHS of the momentum equation arise because even though the individual mass fluxes associated with the small-scale turbulent fluid motions vanish upon averaging, their correlation does not. The crucial point is that there are no *a priori* reasons to believe that the divergence of σ_{ik} should vanish. The implication is that small-scale turbulence can potentially act as a source term in the momentum equation, and *drive* a mean flow, in the form of a zonal flow and/or meridional flow.

It is obvious from eq. (4.15) that σ_{ik} is a symmetric tensor, and so has at most six independent components. Equation (4.15) cannot be used to *calculate* these components, since this would only be possible if the full turbulent flow problem had already been solved, in which case we wouldn't be messing around with mean-field theory in the first place. The gist of the mean-field approach is to construct plausible expressions for the σ_{ik}'s in terms of the mean quantities $\bar{\mathbf{u}}$, $\bar{\rho}$, $\bar{p}$, etc. This, in practice, requires that assumptions be made considering the statistical nature of the small-scale turbulent flow component.

4.2.2 Isotropic turbulence

Consider first incompressible, *isotropic turbulence* in Cartesian geometry. By definition, the small-scale flow field is invariant under translation or rotation, so that $\langle u'_k \rangle \equiv \langle u' \rangle$ $(k = 1, 2, 3)$, which in turn implies

$$\sigma_{ik} = -\rho \left\langle (u')^2 \right\rangle \tag{4.16}$$

so that all components of the Reynolds stresses are identical and depend only on $\langle u' \rangle$. This is a considerable simplification, but we still need to express the RHS of eq. (4.16) in terms of the large-scale flow.

This is where we make use of a rather wild analogy. Consider the turbulent flow field to be made up of fluid "eddies", which form spontaneously and maintain their spatial coherence for a typical lifetime $\tau_{\rm corr}$, during which they move a typical distance $\ell_{\rm corr} = \langle u' \rangle \, \tau_{\rm corr}$ in the large-scale flow. After this they "dissolve" and release locally whatever momentum (and heat content) they carried. This is very much like what *really* happens with the microscopic constituents of the fluid, which travel a certain mean-free-path before they collide and redistribute their momentum and energy. Microscopic shear viscosity is the consequence of particle originating from a region of higher bulk velocity travelling to regions of lower bulk velocity and releasing their momentum there, and similarly with microscopic heat diffusivity. This process clearly leads to a flow of momentum (heat) down any existing velocity (temperature) gradient. We then assume that turbulent eddies do the exact same thing, at least on the spatial scale of the mean flow. *Consequently, we will use the same functional form for the Reynolds stress tensor as for the microscopic (shear) viscosity tensor*:

$$\sigma_{ik} = \mu_T \left(\frac{\partial \bar{u}_i}{\partial x_k} + \frac{\partial \bar{u}_k}{\partial x_i} + \frac{2}{3} \delta_{ik} \frac{\partial \bar{u}_j}{\partial x_j} \right) \tag{4.17}$$

We need, in addition, an expression for the (scalar) "eddy viscosity" μ_T. This we construct as follows:

$$\frac{\mu_T}{\rho} = \frac{\left\langle (u')^2 \right\rangle}{\tau_{\rm corr}} \equiv \ell_{\rm corr} \sqrt{\langle (u')^2 \rangle}. \tag{4.18}$$

In the case of the solar convective envelope, estimates for $\tau_{\rm corr}$ and u' can be constructed from mixing length theory, and this is how the estimate given in eq. (4.8) was obtained. This is also the "theoretical" basis behind the "turbulent viscosity" approach used in the preceding chapter[5].

4.2.3 Anisotropic turbulence: effect of stratification [6]

Assume now that gravity imposes a preferred direction in the turbulent fluid[7]. Working still in Cartesian coordinates and letting gravity be parallel to the z-axis ($\equiv x_3$), we replace eq. (4.18) by a diagonal tensor μ_{ik} having components

$$\mu_{11} = \mu_{22} = \mu_H, \qquad \mu_{33} = \mu_V, \tag{4.19}$$

where μ_H and μ_V are the horizontal and vertical eddy viscosities. The general idea is again that turbulent transport still occurs down gradients of velocity or temperature, but at rates that differ between the vertical and horizontal (we will encounter this notion once again in the following chapter). The Reynolds stress tensor can now be defined as

$$\sigma_{ik} = \mu_{ij}\frac{\partial \bar{u}_k}{\partial x_j} + \mu_{kj}\frac{\partial \bar{u}_i}{\partial x_j}, \tag{4.20}$$

so that the turbulent viscous force $(\nabla \cdot \sigma)$ appearing on the RHS of the equations of motion takes the form

$$F_i = \frac{\partial}{\partial x_1}\left(\mu_H \frac{\partial \bar{u}_i}{\partial x_1}\right) + \frac{\partial}{\partial x_2}\left(\mu_H \frac{\partial \bar{u}_i}{\partial x_2}\right) + \frac{\partial}{\partial x_3}\left(\mu_V \frac{\partial \bar{u}_i}{\partial x_3}\right). \tag{4.21}$$

This depends only on the mean-flow quantities, and so the system of equations is closed.

As arbitrary as this whole procedure may appear, it has been vindicated to some degree in the geophysical context. It the Earth's atmosphere and oceans, it is possible to directly *measure* the velocity correlation $\langle u'_i u'_k \rangle$ and their effect on the mean flow, and so *calculate* μ_H and μ_V via eq. (4.15). In this atmosphere this yields $\mu_V/\mu \sim 10^5$—10^7 and $\mu_H/\mu_V \lesssim 10^2$. In the oceanic surface layers on the other hand, $\mu_V/\mu \sim 10^2$—10^4 and $\mu_H/\mu_V \sim 10^5$.

The important points demonstrated by these geophysical measurements are that (1) when turbulence is present, the associated eddy viscosities are much larger

---

[5] Equation (4.18) implicitly assumes that the full spectrum of turbulent motion is sharply peaked at one specific wavenumber, corresponding to the eddies that dominate momentum and heat transport. This is one VERY dubious assumption.

[6] The material in this section is taken from §3.6 of J.-L. Tassoul's upcoming book *Stellar Rotation*, to be published in by Princeton University Press in 1998, and which I happen to have in preprint form.

[7] How can gravity impose a preferred direction to a turbulent flow?

than their microscopic counterparts, and (2) in the presence of stratification, the eddy viscosities can be strongly anisotropic.

4.2.4 Anisotropic turbulence in the solar interior

There are two obvious sources of anisotropy in the (unmagnetized) interior of the rotating Sun: gravity, with which is associated the restoring force we call buoyancy, and rotation, with which are associated Coriolis and centrifugal accelerations. Since both the density and velocity fluctuations appear in the σ_{ik} (cf. eq. [4.15]), it can be expected that both of these sources of anisotropy can play an important role. Gravity acts only in the radial direction, so the approach described in §4.2.3 can be used. Coriolis and centrifugal forces are a different matter, since they care about the perpendicular distance to the rotation axis and the local flow velocity. Omitting hereafter overbars on mean quantities, and for a spherically symmetric background structure and axisymmetric rotation profile, invoking again the viscosity analogy leads to the following plausible forms for the Reynolds stress components:

$$\sigma_{rr} = 2\mu_V \frac{\partial u_r}{\partial r}, \tag{4.22a}$$

$$\sigma_{\theta\theta} = 2\mu_H \left(\frac{u_r}{r} + \frac{1}{r}\frac{\partial u_\theta}{\partial \theta} \right), \tag{4.22b}$$

$$\sigma_{\phi\phi} = 2\mu_H \left(\frac{u_r}{r} + \frac{u_\theta \cot\theta}{r} \right), \tag{4.22c}$$

$$\sigma_{r\theta} = \mu_H \frac{1}{r}\frac{\partial u_r}{\partial \theta} + \mu_V \left(\frac{\partial u_\theta}{\partial r} - \frac{u_\theta}{r} \right), \tag{4.22d}$$

$$\sigma_{r\phi} = \mu_V r \sin\theta \frac{\partial \Omega}{\partial r} + \Lambda_V \Omega \sin\theta, \tag{4.22e}$$

$$\sigma_{\theta\phi} = \mu_H \sin\theta \frac{\partial \Omega}{\partial \theta} + \Lambda_H \Omega \cos\theta. \tag{4.22f}$$

Note that the functional form of the first four Reynolds stress component is again identical to the microscopic viscous stress tensor in spherical geometry, with the coefficient of shear viscosity μ ($\equiv \rho\nu$) replaced by the eddy viscosities μ_V or μ_H. The same would be true of the last two components if one were to set $\Lambda_V = \Lambda_H = 0$. The terms proportional to μ_V and μ_H are hereafter referred to as the diffusive part of the Reynolds stresses. Physically, the non-diffusive part ($\propto \Lambda_H, \Lambda_V$) of the components $\sigma_{r\phi}$ and $\sigma_{\theta\phi}$ correspond, respectively, to radial and latitudinal fluxes of angular momentum; if their divergence does not vanish, a net turbulent viscous force is being exerted in the ϕ-direction, which will accelerate or deccelerate the zonal flow. At any rate, we're now down to four adjustable parameters: the two coefficients of vertical and horizontal eddy-viscosity μ_V and μ_H, and the two rotational parameters Λ_V and Λ_H (all having units g cm^{-1} s^{-1}). The first two measure the (anisotropic) viscous-like transport of angular momentum by small-scale turbulent fluid motions, as in §4.2.3. The rotational parameters measure the non-vanishing correlation between turbulent motions induced by the Coriolis force. A radially rising fluid element feels the Coriolis force maximally in the equator but not at the poles; likewise, a horizontally moving fluid element feels the Coriolis force at the poles, but not at the equator; thus the explicit $\sin\theta$, $\cos\theta$ dependencies introduced in eqs. (4.22*e,f*).

Working as usual in spherical polar coordinates, the following terms need to be added to the RHS of the momentum equations (eqs. [I.1.15]—[I.1.17]):

$$\rho\frac{\mathrm{D}u_r}{\mathrm{D}t} = \ldots + \frac{1}{r\sin\theta}\left[\frac{\sin\theta}{r}\frac{\partial(r^2\sigma_{rr})}{\partial r} + \frac{\partial(\sigma_{r\theta}\sin\theta)}{\partial\theta}\right] - \frac{1}{r}(\sigma_{\theta\theta}+\sigma_{\phi\phi}) \tag{4.23a}$$

$$\rho\frac{\mathrm{D}u_\theta}{\mathrm{D}t} = \ldots + \frac{1}{r\sin\theta}\left[\frac{\sin\theta}{r}\frac{\partial(r^2\sigma_{r\theta})}{\partial r} + \frac{\partial(\sigma_{\theta\theta}\sin\theta)}{\partial\theta}\right] + \frac{1}{r}(\sigma_{r\theta}-\sigma_{\phi\phi}\cot\theta) \tag{4.23b}$$

$$\rho\frac{\mathrm{D}u_\phi}{\mathrm{D}t} = \ldots + \frac{1}{r\sin\theta}\left[\frac{\sin\theta}{r}\frac{\partial(r^2\sigma_{r\phi})}{\partial r} + \frac{\partial(\sigma_{\theta\phi}\sin\theta)}{\partial\theta}\right] + \frac{1}{r}(\sigma_{r\phi}+\sigma_{\theta\phi}\cot\theta) \tag{4.23c}$$

Because all contributions to the meridional (r,θ) components of the Reynolds stresses defined by eqs. (4.22) are purely diffusive, the Reynolds stresses cannot, by themselves, drive a large-scale meridional circulation. Consequently, we hereafter set $\mathbf{U}_p = 0$ in the ϕ-component of the equations of motion[8]. This means that the steady-state envelope differential rotation should not described by eq. (4.7), but rather by

$$\frac{\sin\theta}{r^2}\frac{\partial(r^3\sigma_{r\phi})}{\partial r} + \frac{1}{\sin\theta}\frac{\partial(\sin^2\theta\sigma_{\theta\phi})}{\partial\theta} = 0,$$

which leads to

$$\frac{\sin^2\theta}{r^2}\frac{\partial}{\partial r}\left(\mu_V r^4\frac{\partial\Omega}{\partial r} + \Lambda_V r^3\Omega\right)$$
$$+\frac{1}{\sin\theta}\frac{\partial}{\partial\theta}\left(\mu_H\sin^3\theta\frac{\partial\Omega}{\partial\theta} + \Lambda_H\sin^2\theta\cos\theta\Omega\right) = 0 \tag{4.24}$$

The terms proportional to Λ_V and Λ_H play a crucial dynamical role. It is now possible, in principle, to obtain a steady-state solution that doesn't even involve a meridional flow $\mathbf{U}$, since the Reynolds stresses can by themselves sustain a zonal flow. This is usually called the Λ-effect. Note that solid-body rotation is no longer an acceptable steady-state, unless of course $\Lambda_V = \Lambda_H = 0$.

Let's pause and look back at what we have accomplished; we now have modified forms of the equations of motion that involve only mean quantities, with all contributions from the small-scale turbulent component subsumed into the four coefficients μ_V, μ_H Λ_V, and Λ_H. We can proceed with the solution of the equations of motion once we have chosen values for these coefficients. And that's where the *real* fun really begins...

[8] We would actually retain $\mathbf{U}_p$ if it could be argued that the circulation is driven by a physical mechanism other than Reynolds stresses. More on this soon.

4.3 Mean-field models of solar envelope rotation

The two Λ-coefficients are properties of the turbulent flow field, and there are no *a priori* reasons to believe that they should be simple numerical coefficients. The solar convective envelope spans many scales heights, and consequently there are good reasons to believe that the properties of the turbulent flow will be depth-dependent[9] Furthermore, in a situation where Coriolis forces are expected to introduce anisotropies in the turbulent flow, one may further expect latitudinal dependencies to exist. Because of symmetry considerations, appropriate expansions for the parameters are of the form:

$$\Lambda_V(r,\theta) = \Lambda_{V0}(r) + \Lambda_{V1}(r)\sin^2\theta + ..., \tag{4.25a}$$

$$\Lambda_H(r,\theta) = \Lambda_{H1}(r)\sin^2\theta + ... \tag{4.25b}$$

Note that there is no $\Lambda_{H0}(r)$ function because latitudinal angular momentum transport must vanish at the poles[10]. These expansions are then truncated, and plausible expressions for the radial functions constructed on the basis of one's favorite turbulence model. You may well imagine that this process involves quite a few *ad hoc* assumptions.

4.3.1 Some simple mean-field models

Rather that discuss the pros and cons of the various turbulence models having been used by various authors to estimate the radial functions in eqs. (4.25), let us simply consider the properties of some simple mean-field models of envelope differential rotation. We will do so by

(1) Retaining only the leading terms in eqs. (4.25),
(2) Assume that Λ_{V0} and Λ_{H1} do not depend on r,
(3) Assume that μ_V and μ_H are independent of r and θ.

This implies $\Lambda_V \equiv \Lambda_{V0}$ and $\Lambda_H = \Lambda_{H1}\sin^2\theta$. Figure 4.1 shows a series of steady-state solutions to eq. (4.24), obtained under different assumptions concerning the sign and relative magnitudes of μ_V, μ_H, Λ_V and Λ_{H1}, as detailed in Table 4.1 below. Each panel shows isocontours of angular velocity $\Omega(r,\theta)$ in a full meridional plane, with the rotation axis coinciding with the left quadrant boundary.

---

[9] This conjecture has received ample support from direct numerical simulations of convective turbulence (see bibliography).

[10] In the literature on this topic, it is often stated, matter-of-factly, that in the limit of slow rotation one can set $\Lambda_H = 0$ but retain the Λ_V term. I have yet to understand the physical underpinning of this statement. Likewise, if anybody out there can explain to me why odd powers of $\sin\theta$ are not retained in the expansions, I would greatly appreciate it.

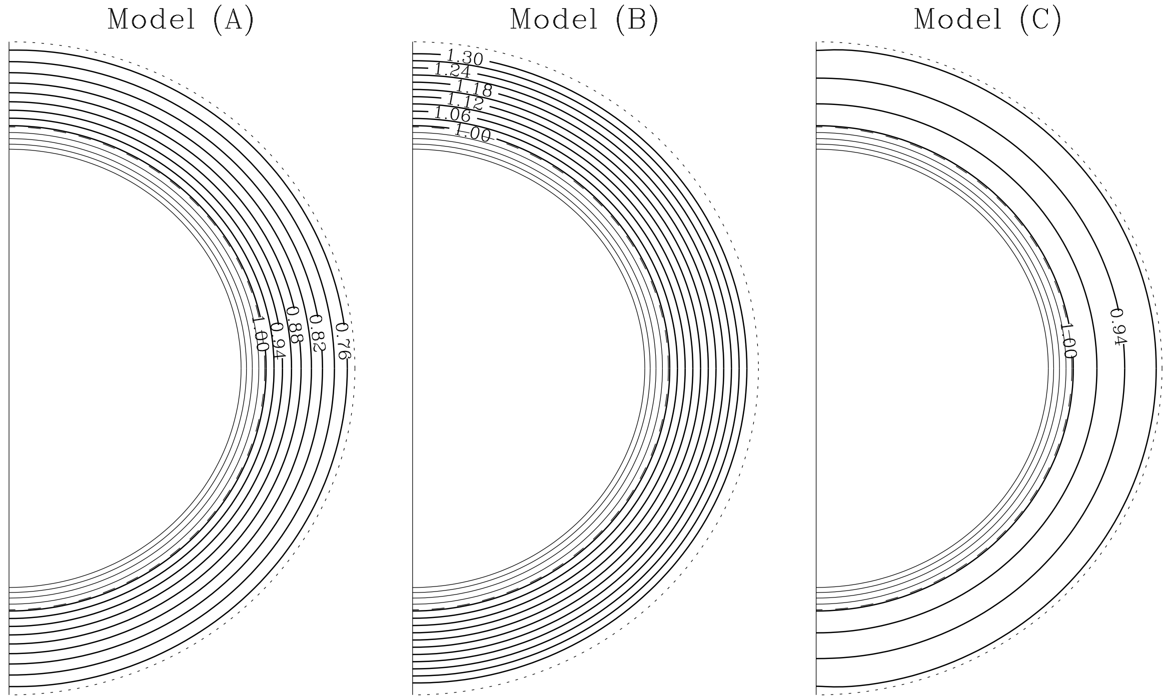

Figure 4.1: Isocontours of angular velocity for three simple mean-field models of the solar envelope differential rotation produced by including the Λ-effect contribution to the Reynolds stresses. Parameters defining each models are listed in Table 4.1. The dashed line is the core-envelope interface ($r = r_{\rm CE}$), the dotted line to the surface ($r = R_\odot$), and Ω is normalized to one at $(r, \theta) = (r_{\rm CE}, \pi/2)$, with contour spacing $\Delta\Omega = 0.03$. The solution beneath the interface is purely viscous, with $\mu_H = \mu_V = 1$.

Table 4.1

Parameters values for mean-field models

Model	μ_V	μ_H	Λ_V	Λ_{H1}
(A)	1	1	+1	0
(B)	1	1	−1	0
(C)	3	1	+1	0
(D)	1	1	−1	−2
(E)	3	1	−1	−2
(F)	10	1	−1	−3
(G)	1	1	+1	−2
(H)	3	1	+1	−3
(I)	10	1	+1	−3

All models have $\Lambda_V = \Lambda_H = 0$ and $\mu_V = \mu_H = 1$ below the core-envelope interface, indicated by a dashed line on all panels of Figure 4.1[11]. Note that this implies non-vanishing viscous stresses at the base of the envelope. At the surface ($r = R_\odot$) the stress-free condition is

$$\mu_V r \frac{\partial \Omega}{\partial r} + \Lambda_V \Omega = 0 \tag{4.26}$$

The models of Figure 4.1 are computed assuming $\Lambda_H = 0$, which implies vanishing latitudinal turbulent transport. The resulting rotation profiles are characterized by a purely radial gradient in Ω, with positive (negative) values of Λ_V leading to surface acceleration (decelleration). The magnitude of the radial gradient is of course influenced by the adopted value for μ_V; the larger μ_V (for a given Λ_V), the smaller the radial gradient (cf. model [C]). One can actually show that the radial profiles of Figure 4.1 are represented quite well by a relationship of the form

$$\frac{\Omega(r)}{\Omega_0} = r^{-\alpha}, \tag{4.27a}$$

where

$$\alpha = \Lambda_V / \mu_V \tag{4.27b}$$

and Ω_0 is some reference rotation rate. Equation (4.27a) actually holds exactly if viscous stresses vanish at both upper and lower boundaries.

Figure 4.2 shows a series of models having $\Lambda_{H1} \neq 0$. These start to get us closer to what we want, namely a latitudinal gradient, which is not surprising since the non-diffusive part of $\sigma_{\theta\phi}$ amounts to latitudinal angular momentum transport even in the absence of latitudinal gradient in Ω. Negative (positive) Λ_{H1} leads to equatorial (polar) acceleration[12], for either sign of Λ_V. So $\Lambda_H > 0$ would seem to be our ticket towards a solar-like envelope differential rotation. In view of Fig. 4.2 (and eq. [4.27a]), one may expect that the iso-Ω contours can be made more "radial" by increasing the $|\mu_V / \Lambda_V|$ ratio, while keeping μ_H fixed (the μ_H / μ_V ratio is called the *anisotropy parameter*, usually denoted s). This is indeed the case, as can be seen by going from Model (D) through (F), or (G) through (I). Models (F) and (I) both have $|\alpha| = 0.1$ and $s = 0.1$. Having $s < 1$ is actually more plausible than the other way around[13]. At any rate, models (F) and (I) are starting to look like the real thing. It looks like we are doing rather well given the

[11] Hey, then, why is there a radial gradient below the core-envelope interface in all models? Didn't we argue before that if $\Lambda_V = \Lambda_H = 0$, the only acceptable steady-state is solid-body rotation? How do you explain this?

[12] This may seem like a counterintuitive sign convention; it can be traced to our inclusion of a minus sign in eq. (4.15), which in turn was motivated by the analogy with the functional form of stress tensor for microscopic viscosity.

[13] Why is that so?

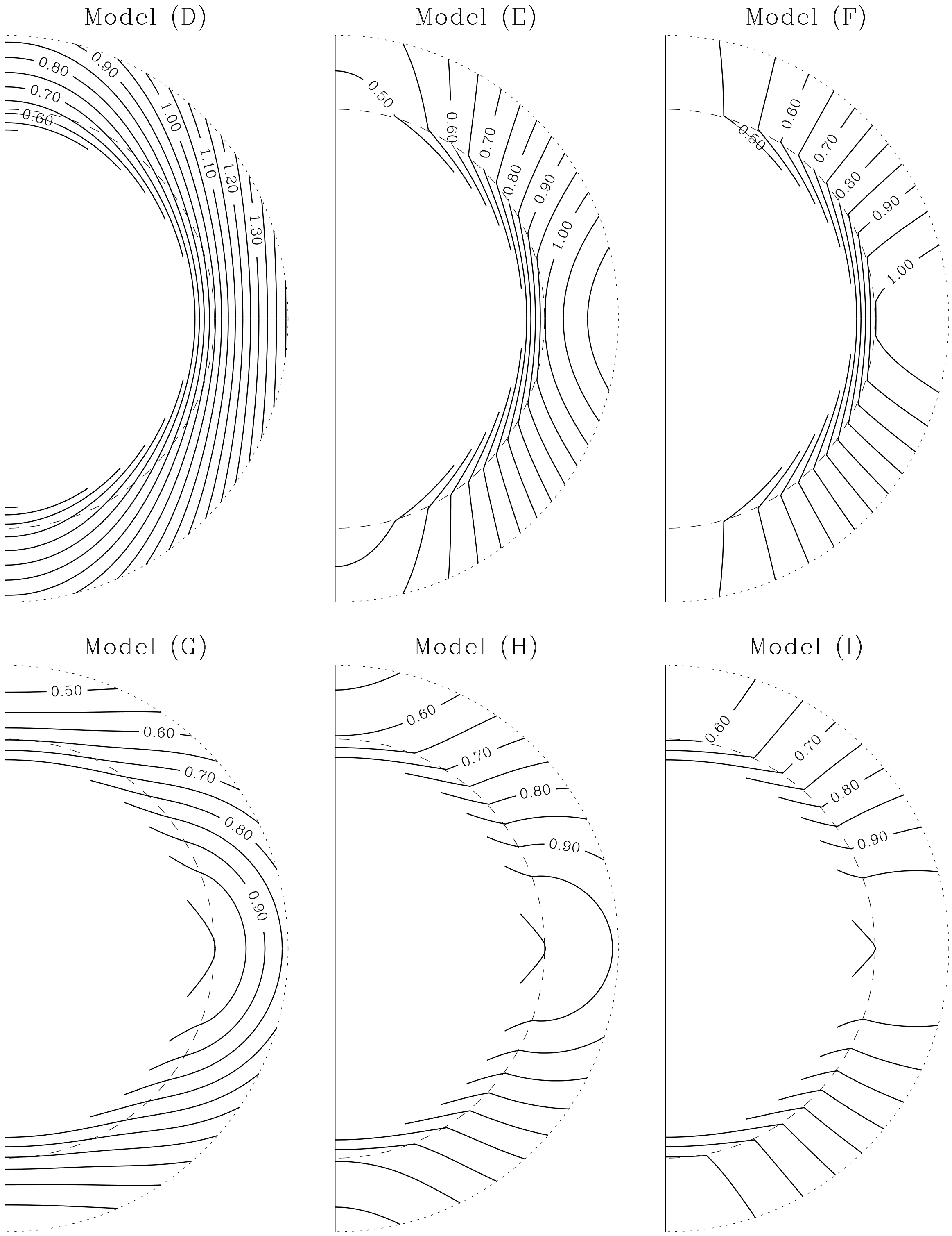

Figure 4.2: More simple mean-field model of the solar envelope differential rotation, this time with $\Lambda_{H1} \neq 0$. The format is similar to Figure 4.1, and model parameters are again listed in Table 4.1. Contour interval is now $\Delta\Omega = 0.05$.

simplistic nature of our little mean-field model. The greatest mistake we could make would be to call it a day at this point.

There is one major problem with *all* the mean-field models of Figures 4.1 and 4.2. Having gradients of angular velocity in the envelope means that there is a gradient of centrifugal force which has an horizontal component that cannot be balanced. Remember from the previous chapter what happens then? A mechanically-driven large-scale meridional circulation, à la Ekman. This circulation will advect angular momentum and affect the overall balance of angular momentum throughout the envelope (cf. eq. [4.7]). Computing self-consistnt mean-field models of the envelope differential rotation is unfortunately no simple matter, because the governing equations are no longer linear, and we won't get into this here. The end result, it turns out, is something that looks an awful lot like rotation constant on *cylinders*. So much for our simple mean-field model.

4.3.2 The Kitchatinov & Rüdiger model

More elaborate mean-field models can be constructed by (1) including a meridional circulation, and/or (2) retaining more terms in the expansions for the Λ's (cf. eq. [4.25]), and/or (3) retaining depth dependencies in the Λ_V and Λ_H functionals. To make a long story short, the more convincing of these models still do not produce a differential rotation profile comparable to helioseismic inferences; in fact most end up producing again profiles characterized by Ω approximately constant on cylinders parallel to the rotation axis. For those interested, a few selected papers, accessible to the relatively uninitiated and representative of this approach, are listed in the bibliography.

It turns out that mean-field models can produce a solar-like envelope differential rotation if one makes the additional assumption that the turbulent heat fluxes are also affected by rotation. Specifically, intead of

$$\mathcal{F}_c = -\chi_c(\nabla T - (\nabla T)_{\rm ad}), \tag{4.28}$$

one writes something like

$$\mathcal{F}_{c,i} = -\chi_{ik}\left[\frac{\partial T}{\partial x_k} - \left(\frac{\partial T}{\partial x_k}\right)_{\rm ad}\right]. \tag{4.29}$$

Once again plausible expressions for the component of the turbulent conductivity tensors are constructed on the basis of a turbulence model. One of the more far-reaching consequence of eq. (4.29) is that a second, thermally-driven meridional flow is now generated, which counteracts the aforementionned mechanically-driven flow due to centrifugal imbalance. Figure 4.3 shows the differential rotation produced by one such model, due to L.L. Kitchatinov and G. Rüdiger.

This differential rotation profile is definitely solar-like! The net meridional circulation in the envelope is characterized by one main cell with pole-to-equator flow near the base of the envelope and an equator-to-pole flow higher up, and a secondary cell near the top of the envelope. The model also predicts a temperature

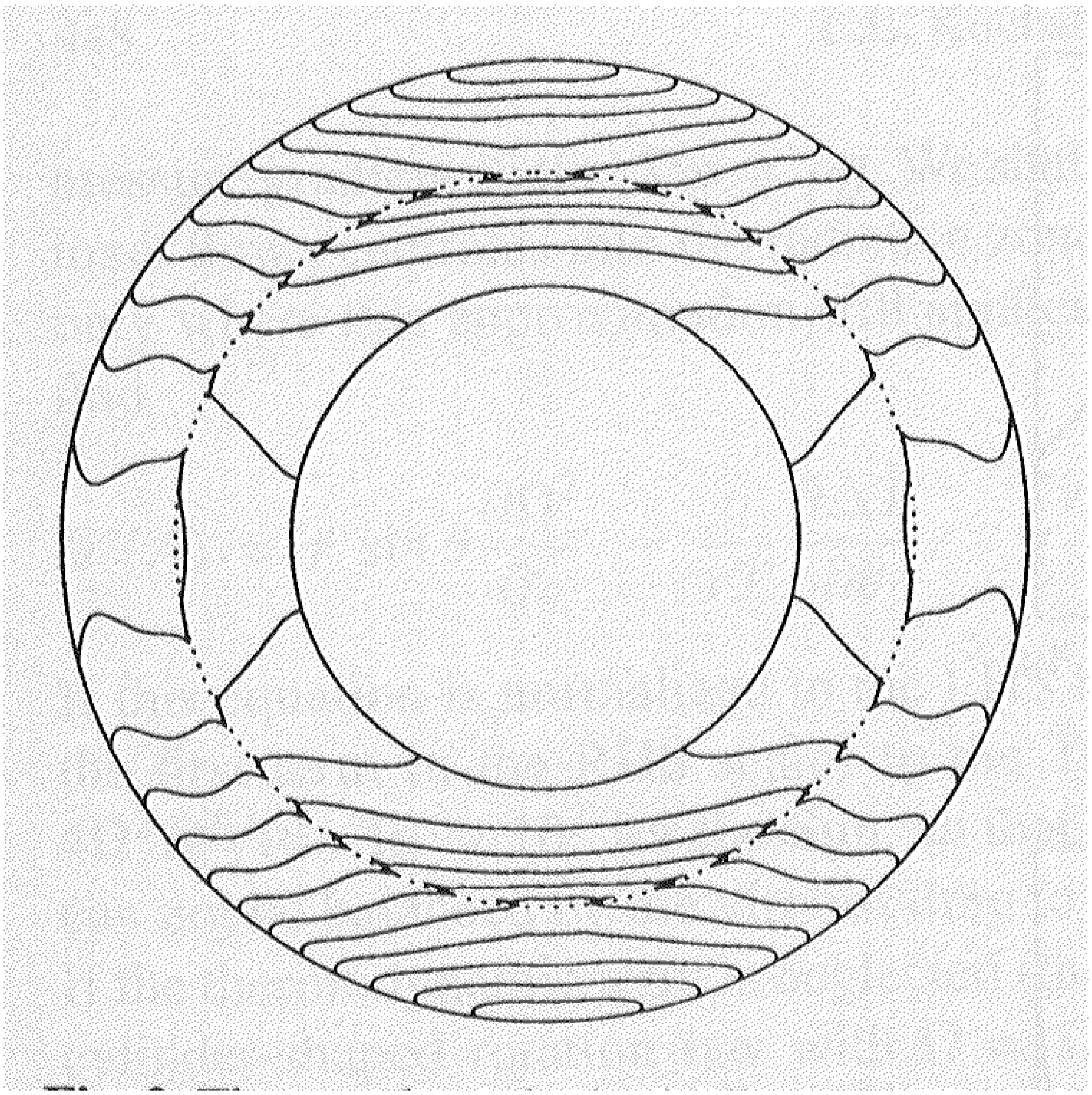

Figure 4.3: Mean-field model of the solar envelope differential rotation, including Reynolds stresses and under the additional assumption that the turbulent heat conductivity is also anisotropic (cf. eq. [4.29] in the text). The dotted line is the core-envelope interface. The solution beneath the interface is purely viscous. Figure reproduced from Kitchatinov, L.L., & Rüdiger, G. 1995, Å299446 (Figure 2, p. 450), who unfortunately do not give the contour spacing for their plot.

excess of $\sim 3\,\mathrm{K}$ at the pole and $\sim 1\,\mathrm{K}$ deficit at the equator (see Figure 4.4), which is within the upper limit inferred observationally.

Should we rejoice? Yes, but not overly so. One significant source of concern is the fact that, as pointed out by Kitchatinov & Rüdiger themselves, the theory underlying the formulation of the Reynolds stress and turbulent conductivity tensor components is expected to be valid in the limit of low rotation; the dimensionless

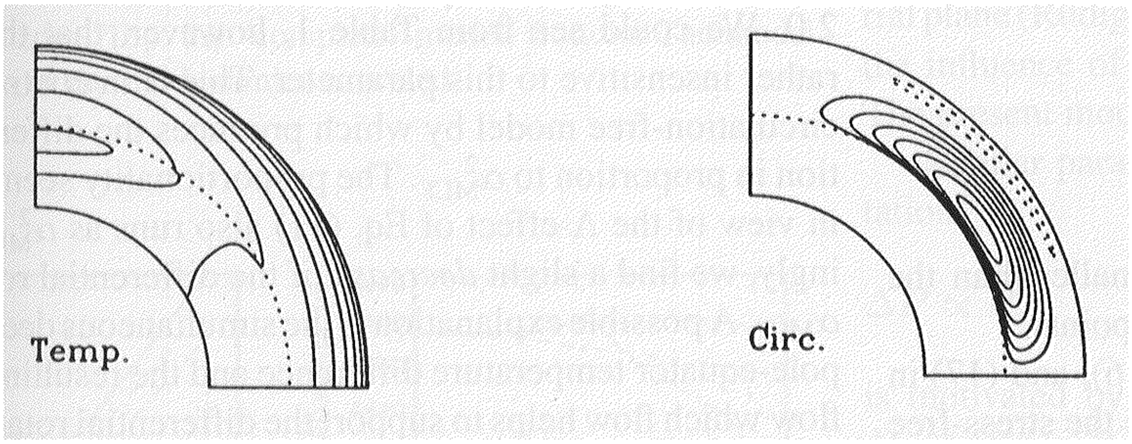

Figure 4.4: Temperature distribution and meridional circulation in the mean-field model of Figure 4.3. The contour plot on the left shows the temperature deviation with respect to the (spherically symmetric) structural reference model. The right panel shows meridional circulation streamlines, with solid (dotted) contours corresponding to counterclockwise (clockwise) flow. This flow has a speed of a few m s^{-1}. Figure reproduced from Kitchatinov, L.L., & Rüdiger, G. 1995, Å299446 (Figure 1, p. 449), who unfortunately again do not give the contour spacing for their plots.

expansion parameter entering their theory is the *Coriolis number*:

$$\Omega^* = 2\Omega\tau_{\rm corr} \tag{4.30}$$

where $\tau_{\rm corr}$ is the correlation time for the largest eddies, which they estimate to be of the order of the convective turnover time. The latter, according to mixing length theory, is of the order of a month, which implies $\Omega^* \sim 2$. What this means is that in the framework of their theory, the Sun is definitely *not* a slow rotator[14]. Furthermore, the turbulence model underlying the calculations of the Reynolds stress and Turbulent conductivity components involves some assumptions involving the functional dependences of various quantities on the local rotation rate that (to me at least) look rather *ad hoc*. The fact that the resulting model looks good doesn't make these assumptions any less *ad hoc*.

In all this we have not yet questioned the basic working asumption of mean-field theory, namely that there exist a separation of scales between the mean and turbulent components of the fields, so that a suitable intermediate averaging scale can be defined. Mean-field theory is a powerful but fragile construct. That it should not be overinterpreted is generally agreed upon, but where to draw the line remains a topic of controversy.

4.4 Numerical models of solar envelope rotation

[14] You may reflect on the validity of writing down expansions in powers of Ω^*, and truncating those series after a few terms on the grounds that $(\Omega^*)^n \ll 1$ if $\Omega^* < 1$ and $n > 1$, when in fact $\Omega^* \gtrsim 1$...

Well, this is where time ran out on me. I was hoping to give in this section an insightful discussion of the results from (1) large-scale simulations of the solar convective envelope, and (2) direct simulation of turbulent convection in a box including the effect of rotation. Instead I find myself forced to refer you to the selection of research papers listed in the bibliography at the end of this chapter. I will limit myself here to the following brief summary remarks:

- Simulations of thermally-driven convection in a rotating spherical shell almost invariably produce differential rotation profiles that are characterized by Ω being nearly constant on cylinders parallel to the rotation axis. This is likely due to the fact that such simulations are carried out in a parameter regime so far removed from solar interior conditions that the turbulent nature of the convective flow differs significantly from convection in the real Sun.
- Direct numerical simulations of the "turbulence-in-a-box" variety, including the dynamical effects of rotation, have shown quite well that rotationally-induced anisotropies in the turbulent flow field can indeed drive a well-organized large-scale flow, even though the small-scale dynamics and statistical properties of the small-scale turbulence differ significantly from that implicitly assumed in the mean-field models discussed in the previous section. Even though these simulations are still carried out in a parameter regime rather far from solar interior conditions, they do succeed in catching the turbulent nature of the flow, unlike most spherical shell simulations produced to date, which all fall under the "turbulent molasse" category.

Problems

(4.1) Work out the details of the calculation described in §4.1. Specifically, carry out the integral in eq. (4.5). Then calculate the angular velocity needed to lead to the same angular momentum content in the case of a rigidly rotating spherical shell. Repeat the calculation for the differential rotation profile associated with magnetic tracers such as sunspots (cf. eq. [1.1c]). How does this compare to the rotation rate of the upper radiative core? You may find useful the following definite integral:

$$\int_0^{\pi/2} \sin^{2m+1}\theta \mathrm{d}\theta = \frac{\prod_{k=1}^{m}(2k)}{\prod_{k=1}^{m}(2k+1)}$$

(4.2) This problem lets you derive the mean-field equations of motion (eq. [4.14]).

(a) First, since it is easier and you will need the resulting expression anyway, derive the mean-field version of the equation of mass conservation.

(b) Now go after the mean-field equivalent of the equations of motion. The trick is to manipulate the various terms so that you form products of density and velocity fluctuations ($\rho u'$) as often as you can, since these vanish upon averaging as per our version of the fundamental assumption of mean-field theory.

Bibliography

The first helioseismic reconstructions of the latitudinal differential rotation within the solar envelope and upper part of the radiative core, demonstrating the maintenance with depth of the surface latitudinal differential rotation and the lack of significant radial gradient down to the base of the envelope, were carried out by:

Brown, T.M. 1985, Nature, 317, 591.
Brown, T.M., & Morrow, C.A. 1987, ApJL, 314, L21.

For the latest on this and surface flow measurements, see

Thompson, M.J. *et al.* 1996, Science, 272, 1300,
Hathaway, D.H. *et al.* 1996, Science, 272, 1306.

Torsional oscillations were originally reported by

Howard, R., & LaBonte, B. 1980, ApJL, 239, L33.

On the general question of angular momentum balance in the solar convective envelope, see

Gilman, P.A., Morrow C.A., and DeLuca, E.E. 1989, ApJ, 338, 528.

Measurements of eddy diffusivities in the Earth's atmosphere are discussed, e.g., in

Houghton, J.T. 1986, *The Physics of the Atmosphere*, Cambridge: Cambridge University Press (second ed.).

The Λ-effect was first formulated by

Biermann, L. 1951, Z. Astrophysik, 28, 304,

and its application to models of the solar envelope differential rotation, much as in §4.3.1 herein, was originally carried out by

Kippenhahn, R. 1963, ApJ, 137, 664.

Many mean-field models for the solar differential rotation have been constructed, and the resulting literature does not exactly make for easy late night reading. For more elaborate mean-field models in all great gory details, you may want to start with

Durney, B.R., & Spruit, H.C. 1979, ApJ, 234, 1067,
Rüdiger, G. 1980, G&AFD, 16, 239
Rüdiger, G. 1989, *Differential Rotation and Stellar Convection*, Akademie Verlag Berlin (reprinted by Gordon & Breach),

in particular the 1980 paper by Rüdiger. For those interested in the history of ideas, Rüdiger's 1989 book includes a comprehensive discussion of the "history" of mean-field models. The model discussed in §4.3.2, as well as Figures 4.3 and 4.4, are taken from

Kitchatinov, L.L., & Rüdiger, G. 1995, Å299446

The paper is rather brief, and does not go into the details of the turbulence model, but ample references are provided. For a rather different take on this problem, but still within mean-field theory, you may ant to take a look at

Durney, B.R. 1996, SolP, 169, 1,

and references therein. On large-scale numerical simulations of the "turbulent molasse" variety, begin with

Glatzmaier, G.A. 1985*a*, ApJ, 291, 300,
Glatzmaier, G.A. 1985*b*, G&AFD, 31, 137,
Gilman, P.A., & Miller, J. 1986, ApJS, 61, 585.

A nice introduction to numerical calculations of the "turbulence in a box" variety is

Brummell, N., Cattaneo, F., and Toomre, J. 1995, Science, 269, 1370.

If you read only two technical papers on this topic, then read

Cattaneo, F., Brummell, N.H., Toomre, J., Malagoli, A., & Hulburt, N.E. 1991, ApJ, 370, 282
Brummell, N.H., Hulburt, N.E., & Toomre, J. 1996, ApJ, 473, 494

5. THE SOLAR TACHOCLINE

"Everything is true ... Everything anybody has ever thought."

Philip K. Dick
Do Androids dream of electric sheep? (1968)

It was argued in the preceeding chapter that the predominantly latitudinal differential rotation in the convective envelope was due to Reynolds stresses arising from the interaction of rotation with thermally-driven convective turbulence. These stresses presumably do not exist in the radiative core, which is stably stratified. On the other hand helioseismology has demonstrated that the radiative core ($r/R_\odot \lesssim 0.72$) rotates essentially rigidly down to at least $r/R_\odot \simeq 0.2$. Clearly a model for the Sun as a whole must somehow "match" these two very different rotation profiles at the core-envelope interface. Once again helioseismology comes to the rescue, having revealed that this matching occurs within a thin shear layer (now often dubbed *tachocline*) located immediately beneath the core-envelope interface. We will argue in part IV of this class that the solar tachocline is the most likely seat of the solar dynamo, which makes an understanding of its dynamical structure particularly relevant to solar magnetism and activity in general.

In this chapter we consider various ways to effect this matching, starting with simple viscous boundary layers (§5.1), as a prelude to dynamical models including thermally-driven large-scale flows. The next section is devoted to a recent model due to E. Spiegel and J.-P. Zahn (§5.2). This is followed (§5.3) by a small bit of fluid stability analysis that has important —and often ignored— consequences for the Spiegel & Zahn model, at least in its original formulation. We conclude (§5.4) with a discussion of the possible influence of large-scale magnetic stresses on the dynamics of the tachocline.

5.1 Viscous boundary layers

We already dealt with the case of viscous angular momentum transport in chapter 3. Here we revisit this mechanism in the context of the core-envelope boundary layer.

5.1.1 Purely viscous layers

We begin the discussion with a simple example. Working in cartesian coordinates, consider a flat plate coinciding with the xz-plane, with the semi-infinite space right of the plate ($y > 0$) filled with an incompressible viscous fluid (constant kinematic viscosity ν, units $\mathrm{cm}^2\,\mathrm{s}^{-1}$). At $t = 0$ the plate is impulsively set in motion in the positive x-direction, with velocity v_0:

$$v(y, 0) = 0, \tag{5.1a}$$

$$v(0, t) = v_0. \tag{5.1b}$$

Because of the no-slip condition imposed at the plate boundary (eq. [5.1b]), the fluid located very close to the plate is accelerated in the positive x-direction, leading to the buildup of a *shear* $\partial v(y, t)/\partial y > 0$, in a thin, plane parallel *boundary layer* immediately adjacent to the plate. The evolution of the flow is governed by the x-component of the equations of motion, which here reduces to

$$\frac{\partial v}{\partial t} = \nu \frac{\partial^2 v}{\partial y^2}, \tag{5.2}$$

where $v \equiv v_x$ for brevity. This parabolic PDE is a linear diffusion equation, of structure identical to the prototypical heat diffusion equation[1]. An analytical solution can be obtained by Laplace transform techniques[2]. First define the transform as

$$f(y, s) = \int_0^\infty e^{-st} v(y, t) dt \tag{5.3}$$

The transformed form of eq. (5.2) is

$$sf = \nu \frac{\partial^2 f}{\partial y^2} \tag{5.4}$$

which admits solutions in the form:

$$f(y, s) = \frac{A}{s} \exp(-\sqrt{s/\nu y}) + \frac{B}{s} \exp(\sqrt{s/\nu y}) \tag{5.5}$$

where A and B are integration constant. Regularity of the solution demands that we set $B = 0$[3]. The solution for $v(y, t)$ is given by the inverse transform:

$$v(y, t) = \frac{v_0}{2\pi i} \int_{c-i\infty}^{c+i\infty} ds\, s^{-1} e^{st} e^{-\sqrt{\frac{s}{\nu}} y} \tag{5.6}$$

[1] which is no coincidence: viscosity is momentum exchange occurring between colliding microscopic fluid constituents, just as heat diffusion is a consequence of collisional energy exchange.

[2] The following Laplace transform solution was kindly provided by Graham Barnes.

[3] What's the big deal if $B \neq 0$ in eq. (5.5)?

This integral can be calculated in the usual way, which involves things like branch cuts, etc. However, in this case it proves easier to first differentiate eq. (5.6) with respect to y, introduce a new integration variable $iu = \sqrt{s}$, and move the integration contour to the imaginary axis:

$$\begin{aligned}\frac{\partial v}{\partial y} &= \frac{(v_1 - v_0)}{\pi\sqrt{\nu}} \int_{ic-\infty}^{ic+\infty} du\, e^{-tu^2} e^{-i\frac{uy}{\sqrt{\nu}}} \\ &= \frac{(v_1 - v_0)}{\pi\sqrt{\nu t}} e^{-\frac{y^2}{4\nu t}} \int_{-\infty}^{\infty} d(\sqrt{t}u - i\frac{y}{s\sqrt{\nu t}})\, e^{-(\sqrt{t}u - i\frac{y}{2\sqrt{\nu t}})^2} \\ &= \frac{(v_1 - v_0)}{\sqrt{\pi\nu t}} e^{-\frac{y^2}{4\nu t}} \end{aligned} \tag{5.7}$$

This describes a Gaussian profile with full width at half maximum equal to $2\nu t$. Its integral with respect to y defines the error function, so that, in view of eqs. (5.1),

$$v(y,t) = v_0 \left[1 - \mathrm{erf}\left(\frac{y}{2\sqrt{\nu t}}\right)\right], \tag{5.8}$$

where $\mathrm{erf}(x)$ is the error function. Equation (5.8) indicates that in a time τ the shear propagates out to a distance

$$h \sim \sqrt{\nu\tau} \tag{5.9}$$

away from the plate. This is illustrated on Figure 5.1. Equivalently, the timescale for the shear layer to spread to a thickness ℓ is

$$\tau = h^2/\nu \tag{5.10}$$

5.1.2 A purely viscous solar tachocline

From eq. (5.10) and our estimate $\nu \sim 10^2\,\mathrm{cm^2\,s^{-1}}$, one can easily verify that under the sole influence of viscosity, the latitudinal gradient in Ω will spread radially inward a distance $0.05\,R_\odot$ in a time $\tau \sim 4\,\mathrm{Gyr}$. Figure 5.2 illustrates this evolution, under the assumption of constant viscosity, and using a normalized solar-like "surface" differential rotation given by:

$$\Omega(R,\theta) = 1 - a_2\cos^2(\theta) + a_4\cos^4(\theta) \tag{5.11}$$

with $a_2 = 0.1264$ and $a_4 = 0.1591$, corresponding to the profile inferred from surface Doppler measurements. The solution of Figure 5.2 was obtained by solving the 2-D, axisymmetric equivalent of eq. (5.2) in spherical geometry:

$$\rho r^2 \sin^2\theta \frac{\partial\Omega}{\partial t} = \frac{1}{r^2}\frac{\partial}{\partial r}\left[\rho\nu r^4 \sin^2\theta \frac{\partial\Omega}{\partial r}\right] + \frac{1}{\sin\theta}\frac{\partial}{\partial\theta}\left[\rho\nu \sin^3\theta \frac{\partial\Omega}{\partial\theta}\right] \tag{5.12}$$

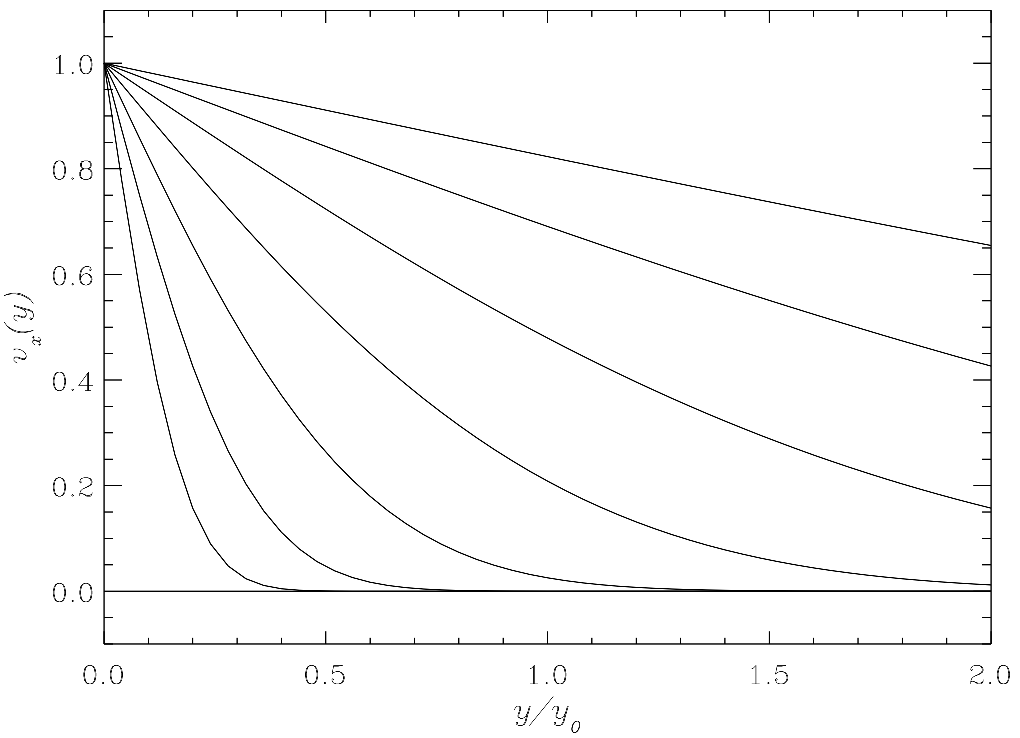

Figure 5.1: Spread of a viscous boundary layer in cartesian geometry, following the impulsive acceleration of a plane parallel boundary plate located at $y = 0$, as described by eq. (5.8). The curves are plotted at times $[0., 0.01, 0.0316, 0.1, 0.316, 1., 3.16, 10]$, measured in units of y_0^2/ν.

where $\Omega = u_\phi / r \sin\theta$, with time measured in units of the diffusion timescale based on the radius of the sphere, i.e., $\tau \sim R^2/\nu \simeq 70\,\text{Gyr}$ for $\nu \sim 10^2\,\text{cm}^2\,\text{s}^{-1}$ and $R = 0.7R_\odot$. From Fig. 5.2 one can estimate that in 4.5 Gyr the layer should have spread to a depth $r/R_\odot \sim 0.05$, i.e., essentially in agreement with helioseismic inferences[4]. Note that since eq. (5.12) is linear in Ω, this result is independent of the amplitude of the latitudinal differential rotation imposed at the upper boundary. We should not rejoice prematurely, however; the microscopic viscosity given by eq. (3.5) represents an absolute *lower* limit to the net viscosity in the solar radiative core. We saw in the preceding chapter that in the presence of turbulence, the *effective* viscosity can be many orders or magnitude larger than its microscopic value. Even a modest increase by a factor of ten leads to a tachocline that is markedly thicker than observed after 4.5Gyr.

[4] True or False: the asymptotic viscous steady-state ($t \to \infty$) is characterized by purely radial isocontours of angular velocity.

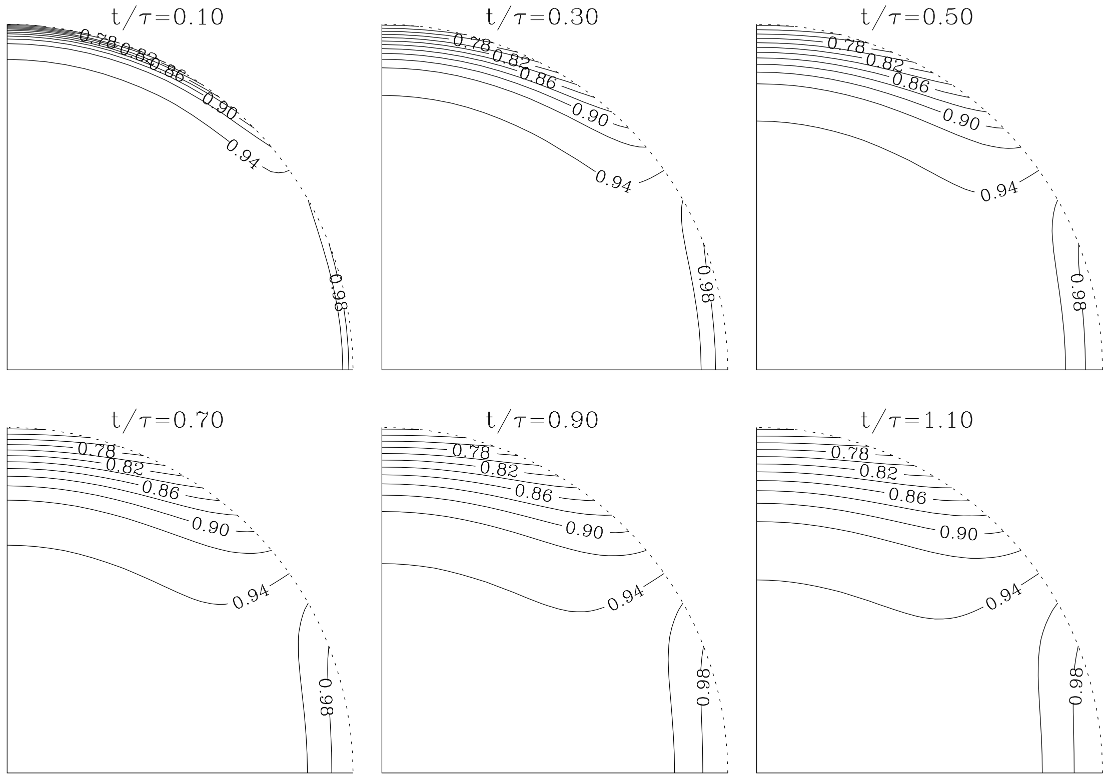

Figure 5.2: Inward spread into the radiative core of the latitudinal angular velocity gradient present at the base of the convective envelope, under the sole influence of viscosity. The upper, circular boundary (dotted line) is the core-envelope interface, *not* the solar surface. The core initially rotates at a dimensionless rate $\Omega = 0.9412$, and the latitudinal differential rotation imposed at $r = R$ is given by eq. (5.11). Time is measured in units of the viscous timescale $\tau = R^2/\nu$. For $\nu \sim 10^2\,\mathrm{cm}^2\,\mathrm{s}^{-1}$ and $R = 0.7R_\odot$, $\tau \simeq 70\,\mathrm{Gyr}$.

5.2 The hydrodynamical tachocline

In this section we will briefly consider one specific hydrodynamical model of the solar tachocline put forth a few years ago by Ed Spiegel and Jean-Paul Zahn (see bibliography for specific references). They investigate the consequences for angular momentum transport of the rotationally-induced, thermally-driven meridional flow in the upper part of the radiative core. The situation is in some ways more complicated than for the Eddington-Sweet circulation of §3.3.2, in view of the presence of *differential* rotation and of the viscous stress imposed at the upper boundary, due to the differential rotation within the convection zone. Begin by expressing all quantities (rotation, temperature, etc.) as a latitude-independent part $A(r,t)$ plus a latitude-dependent perturbation $\hat{A}(r,\theta,t)$ ($\ll A(r,t)$), where

$$\int_0^\pi \hat{A}(r,\theta,t)\sin\theta\mathrm{d}\theta = 0. \tag{5.13}$$

The next step is to drop the convective acceleration term $\mathbf{U}\cdot\nabla\mathbf{U}$ in the equations of motion on the grounds that the Rossby number is small, and to assume geostrophic balance in the latitudinal direction. This is a rather drastic assumption, but one that has the immense advantage that it allows one to formulate linear solutions that are separable in r and $\mu \equiv \cos\theta$, as

$$\hat{A}(r,\mu) = \sum_k \tilde{A}_k(r) f_k(\mu) \tag{5.14}$$

Spiegel and Zahn show that the radial function $\tilde{\Omega}$, measuring the radial dependence of the differential rotation, evolves according to the following equation:

$$\frac{\partial\tilde{\Omega}}{\partial t} = \frac{1}{\rho r^4}\frac{\partial}{\partial r}\left(\rho\nu_V r^4 \frac{\partial\tilde{\Omega}}{\partial r}\right) - \frac{4\Omega^2}{\lambda^2}\frac{1}{\rho r^2}\left\{\frac{g}{N^2 c_p T}\frac{\partial}{\partial r}\left[\chi\frac{\partial}{\partial r}\left(\frac{r^2 p T}{\rho g}\frac{\partial}{\partial r}\frac{\rho r^2\tilde{\Omega}}{p}\right)\right]\right\} \tag{5.15}$$

where g is the gravity, p the gas pressure, T the gas temperature, N the Brunt-Väisälä frequency, χ the thermal conductivity, c_p the specific heat at constant pressure, and $\lambda \simeq 3$ is a numerical coefficient that arises as an eigenvalue of the equation for the horizontal pressure perturbation[5] The first term on the RHS of eq. (5.15) is our familiar viscous transport term. The second term is far more involved, depending as it does on high order derivatives of structural parameters. Considerable simplification occurs if one assumes *a priori* that the tachocline thickness is smaller than the relevant scale heights for the background structural quantities; eq. (5.15) then reduces to:

$$\frac{\partial\tilde{\Omega}}{\partial t} = \nu\frac{\partial^2\tilde{\Omega}}{\partial r^2} - \left[\frac{\chi}{\rho c_p}\left(\frac{2\Omega}{N}\right)^2\left(\frac{R}{\lambda}\right)^2\right]\frac{\partial^4\tilde{\Omega}}{\partial r^4} \tag{5.16}$$

This expression describes the radial spread of the latitudinal differential rotation $\tilde{\Omega}$ into the rigidly rotating radiative core. The fourth order term on the RHS of eq. (5.16) behaves as a diffusion term, in the sense that it leads to the smoothing of any gradient in $\tilde{\Omega}$ across the tachocline, and so, in itself, will lead to a spreading of the initially thin tachocline. This spreading occurs in response to the advection of angular momentum by the thermally-driven secondary flow, and operates in addition to that otherwise produced by ordinary viscous transport. The quantity in square brackets is a coefficient of hyperdiffusion, which can be written in terms of the Eddington-Sweet timescale encountered previously:

$$\frac{\chi}{\rho c_p}\left(\frac{2\Omega}{N}\right)^2\left(\frac{R}{\lambda}\right)^2 = \left(\frac{1}{\lambda}\right)^2\frac{R^4}{t_{ES}} \tag{5.17}$$

[5] In the Spiegel & Zahn paper, the first term on the RHS of their eq. (4.9) — our eq. (5.15)— begins with a $1/r^2$ factor, which doesn't look right dimensionally, especially in view of their eqs. (4.6) and (4.8).

Spiegel and Zahn argue that in the regime appropriate to solar interior conditions, the radiative spreading term dominates over classical viscous spreading (first term on RHS)[6]. Dimensional analysis of eq. (5.16) with the first term on the RHS omitted then yields the following estimate for the tachocline thickness after a time t:

$$\frac{h}{R} \sim \left(\frac{t}{t_{ES}}\right)^{1/4}, \tag{5.18}$$

With $t_{ES} \sim 200\,\mathrm{Gyr}$ for the present-day Sun, one finds $h/R_\odot \sim 0.4$ after 4.5Gyr, which is now much larger than the tachocline thickness inferred from helioseismology. Numerical calculations have since demonstrated that this is *not* a consequence of replacing eq. (5.15) by (5.16), or an artefact of dimensional analysis. We have a real problem here.

5.2.3 Anisotropic viscosity

Let us step back for a bit to the simple case of purely viscous transport treated in §5.1 The tachocline spreads radially because locally, the latitudinal differential rotation in the convective envelope applies a net viscous torque on the underlying upper portions of the radiative core. This torque is a function of latitude and, moreover, changes sign at mid latitudes. We saw in §4.1 that the net angular momentum per unit mass content of a spherical shell in the convective envelope is approximately equal to that of a rigidly rotating spherical shell in the radiative core; *this implies that the convective envelope does not extert any net global torque on the radiative core.* This state of affairs opens an interesting possibility to quench the viscous inward radial spread of the tachocline demonstrated in the preceding section. If, in the tachocline itself, angular momentum can be transported *latitudinally* from equator to pole faster than it is transported radially, then in principle the radial spread can be halted since the radial gradient in Ω is obliterated by horizontal transport.

Perhaps the simplest way to achieve this effect is to invoke the existence of an *anisotropic viscosity* in the upper part of the radiative core. Such an anisotropy may arise if turbulent processes contribute to the net viscosity, and are characterized by small-scale motions that are themselves anisotropic, as they may well be in the presence of a strong radial stratification. To go beyond this sort of hand-waving wishful thinking is an extremely complex undertaking, to which we shall return in §5.3 below. For now, let us simply *assume* that the net viscosity in the tachocline is anisotropic, and can be characterized by only *two* coefficients, ν_V and ν_H, measuring the net efficiency of viscous transport in the "vertical" (i.e., radial) and "horizontal" (θ- and ϕ-directions). The ϕ-momentum equation now reads:

$$\rho r^2 \sin^2\theta \frac{\partial \Omega}{\partial t} = \frac{1}{r^2}\frac{\partial}{\partial r}\left[\rho \nu_V r^4 \sin^2\theta \frac{\partial \Omega}{\partial r}\right] + \frac{1}{\sin\theta}\frac{\partial}{\partial \theta}\left[\rho \nu_H \sin^3\theta \frac{\partial \Omega}{\partial \theta}\right], \tag{5.19}$$

[6] Carry out a dimensional analysis of eq. (5.16) to convince yourself that this is indeed the case.

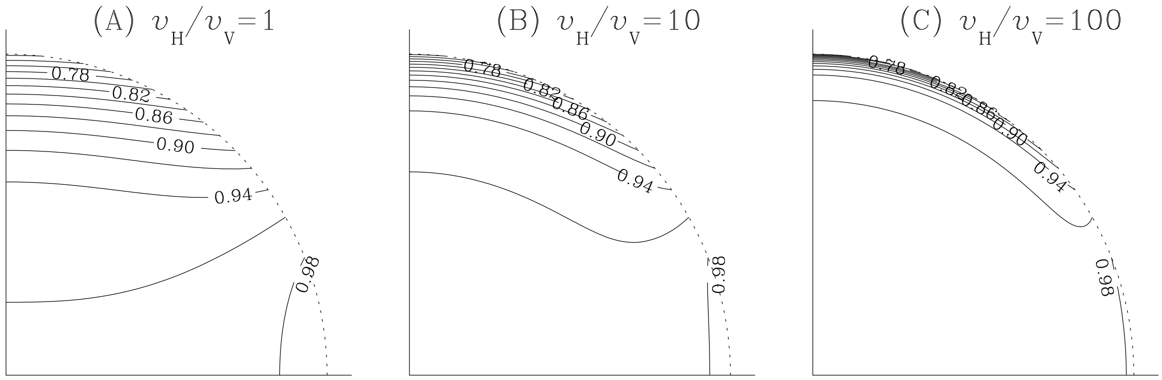

Figure 5.3: Steady-state solutions to the axisymmetric ϕ-momentum equation, under the influence of anisotropic viscosity coefficients. In this case the tachocline thickness scales approximately as the square root of the ratio of horizontal to vertical viscosity coefficients (see text).

subject to the boundary condition given by eq. (5.11), as before. It is again possible to obtain a rough estimate of the tachocline thickness h in a steady state by dimensional analysis of eq. (5.19). With $\partial/\partial t \equiv 0$ and replacing $\partial/\partial r \to h^{-1}$ and $r^{-1}\partial/\partial\theta \to R^{-1}$, one obtains

$$\frac{h}{R} \sim \left(\frac{\nu_V}{\nu_H}\right)^{1/2} \tag{5.20}$$

Requiring $h/R \lesssim 0.05$ implies $\nu_H/\nu_V \simeq 400$, which represents a rather modest level of anisotropy. Figure 5.3 shows three steady-state solutions to eq. (5.19) above, for different anisotropy levels, revealing that eq. (5.20) actually provides a reasonable estimate of the tachocline thickness.

This "trick" is precisely that invoked by Spiegel & Zahn to maintain the thickness of their tachocline within the bounds set by helioseismology. They argue that horizontal shear instability leads to anisotropic fluid turbulence, with the turbulent motions primarily confined to horizontal (i.e., r =constant) surfaces. This turbulence is presumed to lead to enhanced horizontal momentum transport, which is modeled as a diffusive process characterized by an effective viscosity ν_H. Under the assumption that horizontal turbulent heat transport can be neglected within the tachocline, and a few other more minor assumptions (including, as before, the neglect of vertical viscous momentum transport), it can be shown that the tachocline in the steady-state has a thickness of order

$$\frac{h}{R} = \frac{3\pi}{2\mu_4}\left(\frac{\Omega}{N}\right)^{1/2}\left(\frac{\kappa}{\nu_H}\right)^{1/4} \simeq 3\times 10^{-2}\left(\frac{\kappa}{\nu_H}\right)^{1/4}, \tag{5.21}$$

where μ_4 is a numerical coefficient of order unity, again obtained from solving an eigenvalue problem for the horizontal perturbations of thermodynamical quantities, and the quantity ν_H/κ looks like a kind of Prandtl number, although unconventionally defined in terms of a *turbulent* viscosity but a *microscopic* thermal diffusivity κ ($= \chi/\rho c_v$, units cm^2 s^{-1}). For a gas of fully ionized hydrogen,

$$\chi \sim 2 \times 10^{-4} \frac{T^{5/2}}{\ln \Lambda}, \qquad [\mathrm{erg\ s^{-1} K^{-1} cm^{-1}}] \tag{5.22}$$

At the base of the solar convective envelope, $\rho \sim 0.1\,\mathrm{g\,cm^{-3}}$ and $c_v \sim 2 \times 10^7$ erg K^{-1}, which leads to $\kappa \sim 3 \times 10^5\,\mathrm{cm^2\,s^{-1}}$. Requiring $h/R \simeq 0.05$ translates into $\nu_H/\kappa \simeq 10$, which in turns implies $\nu_H \sim 10^5\,\mathrm{cm^2\,s^{-1}}$. We estimated previously that the microscopic viscosity at the base of the solar convective envelope is $\sim 10^2\,\mathrm{cm^2\,s^{-1}}$, which then amounts to a anisotropy level

$$\frac{\nu_H}{\nu} \sim 10^3 \tag{5.23}$$

which is more than required in the case of pure viscous spreading, but still not extreme. The greater anisotropy needed, as compared to the purely viscous case, reflect the greater efficiency of the fourth-order "hyperdiffusion" at smoothing out a very thin tachocline.

The introduction of strong horizontal turbulent momentum transport, while neglecting horizontal turbulent heat transport, introduces a potentially serious inconsistency in the model as a whole, however. Remember that fundamentally, the hyperdiffusion term represents the (advective) angular momentum transport by the flow within the tachocline. Clearly turbulent motions can transport heat as well as momentum, and so annihilate the horizontal temperature gradient that, ultimately, is responsible for driving the tachocline meridional flow in the first place. The relative importance of momentum transport versus heat transport is measured by the *Prandtl number*, defined generally as

$$\mathcal{P} = \frac{\nu}{\kappa} \tag{5.24}$$

for microscopic values of the transport coefficients, $\mathcal{P} \sim 10^{-3}$ at the base of the envelope. In a turbulent regime, *both* the effective viscosity and thermal diffusivity are likely to be enhanced with respect to those microscopic values; whether the resulting turbulent Prandtl number ($\mathcal{P}_T$) will end up larger or smaller than its microscopic counterpart then becomes the central question, since turbulent heat transport can only be safely neglected if $\mathcal{P}_T \gg 1$. Unfortunately there exists no way to reliably estimate $\mathcal{P}_T$ for solar interior conditions. Although current numerical simulations cannot reach the appropriate parameter regime, they tend to suggest that $\mathcal{P}_T \sim 1$. This, however, is for thermally-driven convective turbulence, rather than the anisotropic shear flow turbulence invoked by Spiegel & Zahn. They actually argue that in an anisotropic turbulent regime, horizontal turbulent heat transport can still be neglected in the energy equation, as long as $\nu_H/\kappa \ll (R/h)^2$, without leading to internal inconsistencies in the model[7].

---

[7] Editorial comment: I don't see how the thickness of the tachocline has anything to do with the relative efficiency of *horizontal* heat and momentum transport within the turbulent tachocline. In fact this has always been and continues to be my main objection to Spiegel & Zahn's model. End of editorial comment.

At any rate, given all the approximations inherent in the model, it is a remarkable fact that numerical calculations of the tachocline structure, which relax many (but not all) of the assumptions inherent in Spiegel & Zahn's original formulation, should yield a tachocline thickness that is only 30% smaller than eq. (5.21), for present-day solar conditions (see paper by J. Elliot, in the bibliography). However, the numerical simulations of Elliott once again *assume* the existence of enhanced horizontal momentum transport. This is the topic to which we now turn.

5.3 The stability of horizontal shear flows

In the context of the Spiegel & Zahn model, the observed thickness of the tachocline can be only be reproduced by *assuming* the existence of enhanced latitudinal turbulent momentum transport. Spiegel & Zahn ascribe this enhancement to turbulence arising from horizontal shear instability, but do not carry out a stability analysis to support their claim. Let's look into that a bit.

5.3.1 Hydrodynamical stability

We first consider the hydrodynamical stability of a purely zonal large-scale flow ($u_\phi = r\sin\theta\Omega$), subject to purely latitudinal shear (i.e., $\mathrm{d}\Omega/\mathrm{d}r = 0$) in the adiabatic, inviscid limit. We restrict ourselves to fluid motions confined to spherical surfaces ($r = r_0$ =constant). The net flow velocity is then the sum of the large-scale, background differential rotation, and of the 2-D flow $\mathbf{u}$ associated with any growing perturbation:

$$\mathbf{U}(\theta,\phi,t) = u_\theta(\theta,\phi,t)\hat{\mathbf{e}}_\theta + [r_0\sin\theta\Omega(\theta) + u_\phi(\theta,\phi,t)]\hat{\mathbf{e}}_\phi \tag{5.25}$$

This can be justified in a first approximation on the grounds that in the solar radiative core vertical motions are inhibited by the underlying stable stratification. In what follows, we follow the approach of M. Watson (see bibliography) in *formulating* the hydrodynamical stability problem, but end up solving the problem numerically rather than analytically; this will allow us to consider differential rotation profiles of a more general form than Watson could accomodate within his analytical approach.

Working in spherical polar coordinates (r,θ,ϕ), we linearize the equation of motions by neglecting all terms of order $\mathbf{u}^2$ and higher. It can be shown[8] that the θ- and ϕ-components of equations of motions then become

$$\left(\frac{\partial}{\partial t} + \Omega\frac{\partial}{\partial\phi}\right)u_\theta - 2\Omega\cos\theta\, u_\phi = -\frac{1}{\rho_0 r_0}\frac{\partial p}{\partial\theta} \tag{5.26a}$$

$$\left(\frac{\partial}{\partial t} + \Omega\frac{\partial}{\partial\phi}\right)u_\phi + \frac{1}{\sin\theta}\frac{\partial}{\partial\theta}(\Omega\sin^2\theta)\,u_\theta = -\frac{1}{\rho_0 r_0\sin\theta}\frac{\partial p}{\partial\phi} \tag{5.26b}$$

---

[8] As you should verify for yourselves by doing problem 5.1.

where p is now the perturbation with respect to the reference pressure, while the mass conservation equation becomes

$$\frac{1}{r\sin\theta}\frac{\partial}{\partial\theta}(\rho_0\sin\theta\, u_\theta)+\frac{1}{r\sin\theta}\frac{\partial}{\partial\phi}(\rho_0\, u_\phi)=0. \tag{5.27}$$

We begin by introducing an horizontal stream function $\Psi(\theta,\phi,t)$ such that

$$\rho_0 u_\theta=\frac{1}{\sin\theta}\frac{\partial\Psi}{\partial\phi}, \tag{5.28a}$$

$$\rho_0 u_\phi=-\frac{\partial\Psi}{\partial\theta}, \tag{5.28b}$$

so that eq. (5.27) is automatically satisfied. Substituting (5.28) into (5.26*a,b*) and eliminating the pressure yields a single PDE for the stream function:

$$\left(\frac{\partial}{\partial t}+\Omega\frac{\partial}{\partial\phi}\right)\nabla^2\Psi-\frac{1}{\sin\theta}\frac{\partial}{\partial\theta}\left(\frac{1}{\sin\theta}\frac{\partial}{\partial\theta}(\Omega\sin^2\theta)\right)\frac{\partial\Psi}{\partial\phi}=0, \tag{5.29}$$

where ∇^2 represents the horizontal part (i.e., r =constant) of the usual Laplacian operator in spherical polar coordinates:

$$\nabla^2\equiv\frac{1}{\sin\theta}\frac{\partial}{\partial\theta}\left(\sin\theta\frac{\partial}{\partial\theta}\right)+\frac{1}{\sin^2\theta}\frac{\partial^2}{\partial\phi^2}. \tag{5.30}$$

Now comes the crucial part; we look for normal mode solutions having the form

$$\Psi(\theta,\phi,t)=\psi(\theta)\exp[im(\phi-\omega t)],\qquad m=0,1,... \tag{5.31}$$

where the frequency ω and amplitude ψ are complex quantities. Substituting (5.31) into (5.29) and introducing a new independent variable $\mu=\cos\theta$ yields the following ODE:

$$\left\{(\Omega-\omega)\left[\frac{\mathrm{d}}{\mathrm{d}\mu}\left((1-\mu^2)\frac{\mathrm{d}}{\mathrm{d}\mu}\right)-\frac{m^2}{1-\mu^2}\right]-\frac{\mathrm{d}^2}{\mathrm{d}\mu^2}[\Omega(1-\mu^2)]\right\}\psi(\mu)=0. \tag{5.32}$$

where the background differential rotation profile $\Omega(\mu)$ is a known quantity, and time is measured in units of the equatorial angular velocity. Regularity of the solutions requires that $\psi(-1)=\psi(1)=0$ to avoid divergence on the polar axis. For a given value of m, eq. (5.32) describes a 1-D linear eigenvalue problem for ω and $\psi(\mu)$. The eigenvalue problem can be solved in a number of ways. Here we used a method based on inverse iteration, a technique that we will encounter again in part IV of this course.

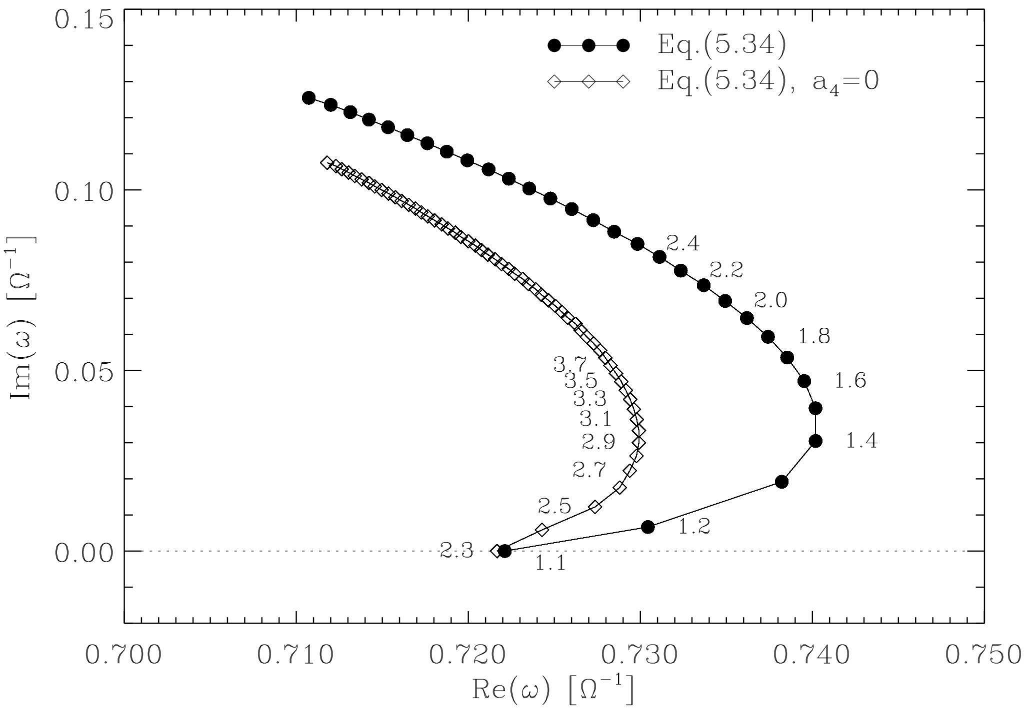

Figure 5.4: Distribution of eigenvalues ω in the complex plane, for a sequence of solutions with increasing a in eq. (5.34). The diamonds correspond to a sequence with $a_4 = 0$ in (5.34), which is the case originally treated by Watson, and the solid dots to the full latitudinal dependency. Eigenvalues are calculated for increments of 0.1 in a, with the first few a values labeled along the curves.

We carry out our first stability analysis for the latitudinal differential profile characterizing the bulk of the solar convective envelope. We saw previously that to a good approximation that profile can be parameterized as

$$\Omega(\mu) = 1 - a_2\mu^2 - a_4\mu^4, \tag{5.33}$$

where $a_2 = 0.1264$ and $a_4 = 0.1591$. Note that this corresponds to a $\simeq 29\,\%$ pole-equator difference in Ω. In view of eq. (5.31), shear flow instability is deemed to occur whenever there exist at least one value of m for which $\mathrm{Im}(\omega) > 0$. To investigate this matter, we consider a one-parameter family of solar-like rotation profiles defined as

$$\Omega(\mu; a) = 1 - a(a_2\mu^2 + a_4\mu^4), \qquad a \geq 0 \tag{5.34}$$

with $a_2 = 0.1264$ and $a_4 = 0.1591$ as always, and try to find values of a (and/or m) for which eq. (5.34) leads to horizontal shear flow instability. The solid dots on Figure 5.4 are a series of eigenvalues of eq. (5.32) plotted in the complex plane, for gradually increasing a in eq. (5.34).

Instability sets in at $a \simeq 1.1$, which represents a latitudinal differential rotation only slightly larger than observed solar rotation ($a = 1$ in eq. [5.34]). The diamonds are a similar sequence of solution, computed this time with $a_4 = 0$ in eq. (5.34)[9]. In this case a value $a \simeq 2.3$ corresponds to a $\simeq 29\,\%$ pole-equator difference in Ω, which is quite close to the $\simeq 31\,\%$ pole-equator difference for $a = 1.1$ in (5.34) with $a_4 = 0.1591$. Note that $\Omega^{-1} \sim 4\,$days, so that a dimensionless growth rate $0.05\,\Omega^{-1}$ corresponds to an e-folding time of about three months. Similar calculations for higher values of m reveal that the $m = 1$ mode is the only unstable mode for $a \lesssim 1.5$, and, for the class of profiles defined by eq. (5.34), remains the mode with the largest growth rate until very large values of a.

Figure 5.5 shows the spatial part of eigenmode for the $a = 2$ supercritical solution[10]. The instability is *global*, with the flow perturbation symmetric about the equator[11] and extending to high latitudes.

So, we have established the magnitude of the horizontal angular velocity gradient required for small amplitude horizontal perturbations to grow exponentially in time. But what is happening here, physically? To address this question we can use some of the mean-field mathematical machinery developed in the preceding chapter. Let's treat the perturbation components u_θ and u_ϕ as small-scale fluctuations in the mean-field sense[12]. The transfer of momentum due to the flow $\mathbf{u}$ can be represented by Reynolds stresses $\propto -\langle u_\theta u_\phi \rangle$. Figure 5.6(A) shows the velocity correlation $u_\theta u_\phi$ corresponding to the planform shown on Fig. 5.5. But how should we go averaging this? Since we are looking at the momentum transfer to or from an *axisymmetric* mean-flow, an average in longitude would seem like the right thing to do[13]. The result, corresponding then to the $\sigma_{\theta\phi}$ Reynolds stress component, is plotted as a solid line on Fig. 5.6(B). The stress component $\sigma_{\theta\phi}$ is positive (negative) in the North (South) hemisphere, which implies a flux of angular momentum from equatorial to polar regions. With the ϕ-momentum equation expressed in terms of Ω, the net turbulent viscous force acting on the mean-flow is given by the RHS of eq. (4.23c) divided by $\sin\theta$ and with $\sigma_{r\phi} = 0$[14], and is plotted as a dashed line on Fig. 5.6(B). It is positive (negative) at high (low) latitudes, and so acts to accelerate (deccelerate) the mean flow. Reynolds stresses counteracting the mean-flow means that energy is being transferred from the mean-flow to the horizontal flow $\mathbf{u}$. In other words, the energy source for the instability is the kinetic energy of the mean flow.

---

[9] This is actually the one-parameter formulation used originally by Watson in his paper.

[10] Given the shape of this planform, what would a "movie" of this solution look like?

[11] Figure 5.5 looks to me antisymmetric about the equator... What's going on here?

[12] Do you think this makes any sense? Look again at Figure 5.5...

[13] This is actually completely equivalent to a temporal average. Can you figure out why? Hint: the answer is related to the question asked in footnote #10.

[14] Why are we setting $\sigma_{r\phi} = 0$ here?

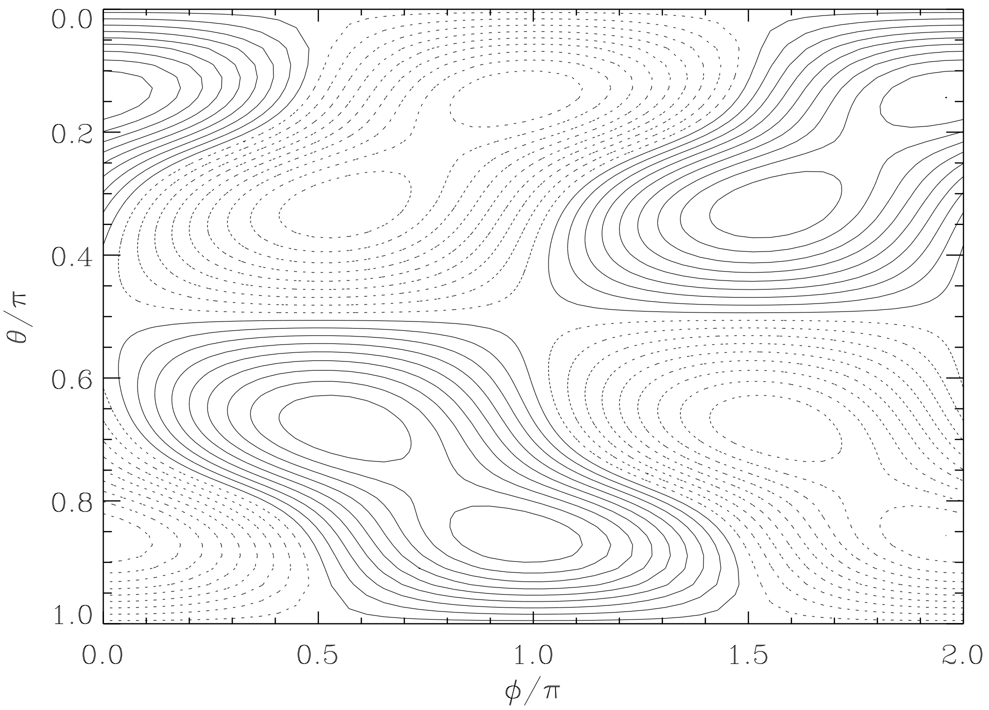

Figure 5.5: Planform of the supercritical $m = 1$, $a = 2$ mode of Figure 5.4. More specifically, the plot shows isocontours of $\mathrm{Re}[\psi(\theta)\exp(im\phi)]$, which correspond to instantaneous streamlines of the flow in view of eq. (5.28). Solid (dotted) lines correspond to counterclockwise (clockwise) fluid motions. Note the poleward tilt of the flow cells.

We have something intriguing on our hands here; is the magnitude of the solar surface latitudinal differential rotation limited by horizontal shear flow instability? One needs to be careful not overinterpreting the model; the assumption of predominantly horizontal fluid motions, in the thermally unstably stratified solar envelope, is likely a rather poor approximation. Within the stably stratified tachocline, however, that assumption has much better chances to hold true. And since $\partial\Omega/\partial\theta$ is therein everywhere smaller than the envelope value, we can only conclude that *the tachocline horizontal differential rotation is stable with respect to the hydrodynamical shear flow instability*. This is very bad news for the Spiegel & Zahn anisotropic turbulence hypothesis, since these authors invoked horizontal shear flow instability as the mechanism leading to the enhanced horizontal turbulence needed to produce a thin tachocline.

5.3.2 A joint magnetohydrodynamical instability

The hydrodynamical stability of the horizontal shear below the base of the solar convective envelope poses a serious challenge to Spiegel & Zahn's tachocline model, which in its original form invoked horizontal shear-flow turbulence to pro-

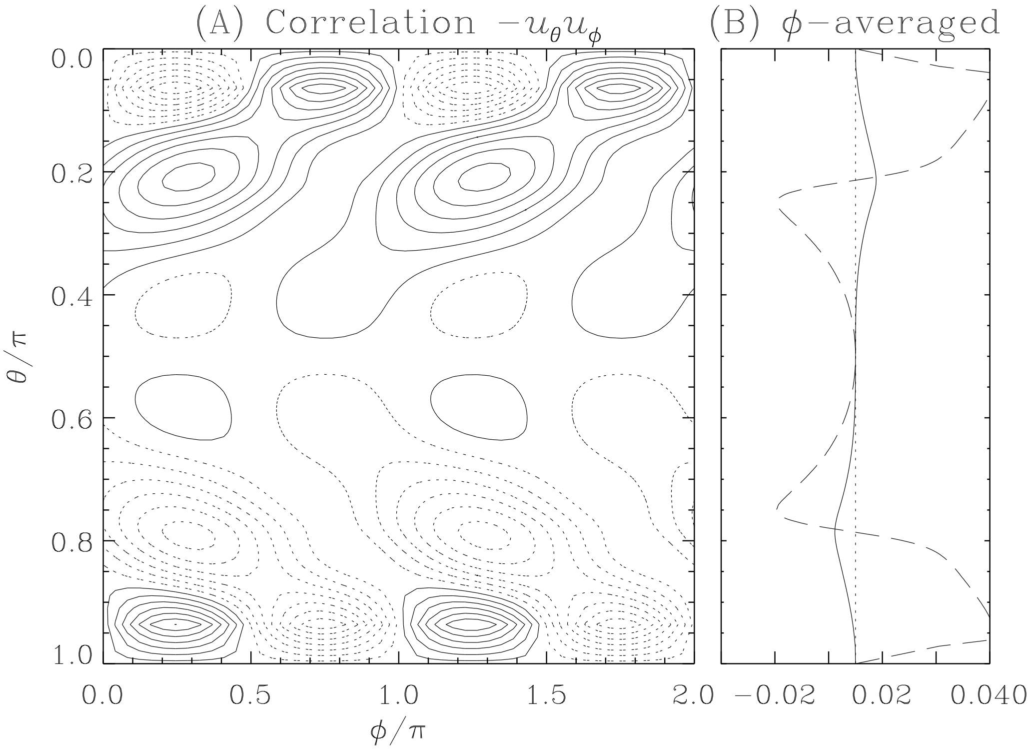

Figure 5.6: (A) velocity correlations associated with the growing horizontal flow **u** corresponding to the planform shown on Figure 5.5. Solid (dotted) lines correspond to positive (negative) velocity correlations. The solid line on part (B) is the zonal (ϕ) average of part (A), and the dashed line is the net turbulent viscous force acting on the mean flow.

vide the enhanced horizontal angular momentum transport needed to produce a thin tachocline. In this section we examine one possible solution to this difficulty.

The stability analysis carried out above was done in the purely hydrodynamical limit, i.e., in the absence of magnetic fields. Yet there is considerable evidence (to be reviewed in part IV of this class, sorry for the forward referencing...) that the tachocline is the seat of the solar dynamo, so that large magnetic fields can be expected to exist therein. Even if the solar dynamo actually resides fully within the convective envelope, any poloidal finding its way downward into the tachocline will find itself subjected to a strong radial shear, leading to the growth of a toroidal magnetic field component. As it turns out, this magnetic field can strongly alter the stability properties of the underlying differential rotation profile.

The following is a brief overview of the 2-D MHD stability analysis carried out recently by P. Gilman and P. Fox (see bibliography). Their work was motivated by the recognition that the latitudinal differential rotation within the tachocline is indeed stable with respect to hydrodynamical shear flow instabilities. Their formulation of the problem is in many ways similar to that of the purely hydrodynamical stability case discussed above[15]. In addition to a background angular velocity $\Omega(\theta)$, there now exists a background toroidal field

$$B_\phi(\theta) = \beta(\theta)\sin\theta. \tag{5.35a}$$

The velocity perturbation $\mathbf{u}$ is treated exactly as before (eqs. [5.28], [5.31]). The 2-D magnetic field $\mathbf{b}$ associated with the growing perturbation is defined in a manner analogous to the small-scale velocity perturbation $\mathbf{u}$, and is also expressed in terms of a "stream function" $X(\theta,\phi,t)$:

$$b_\theta = \frac{1}{\sin\theta}\frac{\partial X}{\partial\phi}, \tag{5.35b}$$

$$b_\phi = -\frac{\partial X}{\partial\theta}, \tag{5.35c}$$

so that the constraint $\nabla\cdot\mathbf{B}=0$ is satisfied by construction. The quantity $X(\theta,\phi,t)$ is then expanded as

$$X(\theta,\phi,t) = \chi(\theta)\exp[im(\phi-\omega t)], \qquad m = 0, 1, ... \tag{5.36}$$

again with boundary conditions $\chi = 0$ on the symmetry axis. This allows to recast the equation of motion and the induction equation —both linearized— in the form of *two* coupled ODEs defining once again a linear eigenvalue problem:

$$(\Omega-\omega)\mathcal{L}\psi - \psi\frac{\mathrm{d}^2}{\mathrm{d}\mu^2}[\Omega(1-\mu^2)] - \beta\mathcal{L}\chi + \chi\frac{\mathrm{d}^2}{\mathrm{d}\mu^2}[\beta(1-\mu^2)] = 0, \tag{5.37a}$$

$$(\Omega-\omega)\chi = \beta\psi, \tag{5.37b}$$

where, for brevity, we have defined the Legendre operator $\mathcal{L}$ as

$$\mathcal{L}A = \frac{\mathrm{d}}{\mathrm{d}\mu}\left[(1-\mu^2)\frac{\mathrm{d}A}{\mathrm{d}\mu}\right] - \frac{m^2}{1-\mu^2}A. \tag{5.37c}$$

You may easily verify that in the limit $\chi\to 0$ eqs. (5.37) reduce to (5.32) above.

Gilman and Fox have solved this eigenvalue problem for solar-like differential rotation and a broad toroidal field, defined by ($\beta(\theta) = \beta_0\cos\theta$ in eq. [5.35a], so that $B_\phi \propto \sin\theta\cos\theta$). They show that $m = 1$ wavenumber instability ($\mathrm{Im}(\omega) > 0$) occurs for almost any magnitude of the differential rotation and toroidal field

[15] Gilman and Fox use latitude/longitude (ϕ and λ in their notation) as independent variables, instead of the (θ,ϕ) of spherical polar coordinates. So do not be surprised if, upon comparing their paper to these notes, you find sines becoming cosines, and things like that.

strength, whenever a broad toroidal field strength is present. The main angular momentum transport agent turns out to be the Maxwell stresses, with the Reynolds stresses actually contributing to *equatorward* transport, in contrast to the purely hydrodynamical case. For weak toroidal field strengths, the instability extracts energy from the differential rotation, and for strong toroidal field from the toroidal field itself. The e-folding time of the instability is of the order of a few months for field strengths of a few 10^4 G.

Gilman & Fox make the interesting suggestion that transport postulated by Spiegel & Zahn may well be present, but due to this magnetohydrodynamical instability, rather than the purely hydrodynamical horizontal shear flow instability.

5.3.3 Some remarks on the relevance of linear stability theory

We have reached the point where we need to step back a bit and reflect on this whole business of (magneto)hydrodynamical stability.

The first thing we need to consider is whether the stability analysis of §5.3.1 really rules out turbulence due to purely hydrodynamical instability of the horizontal shear flow. Our analysis was based on the linearized form of the equations of motion, and focused on the growth rate of flow disturbances of infinitesimal amplitude. We concluded that in the solar tachocline, such perturbations would not grow ($\mathrm{Im}(\omega) < 0$ in eq. [5.31]). How about if the flow perturbations are not infinitesimal in their amplitude? This is no moot point, as the tachocline is located immediately beneath a fully convective envelope; overshooting (or more appropriately here, undershooting) from above represents a potentially powerful source of high amplitude perturbations. The question then becomes whether the horizontal shear within the tachocline is susceptible to *finite amplitude instability.* Such a stability analysis has not yet been carried out.

Next we should consider whether the joint MHD instability described in §5.3.2 can really provide the enhanced horizontal momentum transport needed in the Spiegel & Zahn tachocline model. The stability analysis of Gilman & Fox indicates that unlike in the purely hydrodynamical case, infinitesimal horizontal perturbations will grow ($\mathrm{Im}(\omega) > 0$) if a broad toroidal field is present within the tachocline. This is certainly an encouraging result, but it represents just the first of three needed steps, as discussed in §3.4. One should now follow the instability into its nonlinear regime until it saturates, and then construct appropriate transport coefficients (what we called ν_{eff} in §3.4, or ν_H in the context of the Spiegel & Zahn hypothesis). This has not yet been done.

Finally, in drawing conclusions from the type of stability analysis carried out in §5.3, one has to contend with a rather fundamental difficulty. The stability analysis in §5.3 used the observed solar differential rotation (in the form of eq. [5.34]) as a *reference state* from which the stability analysis was carried out. However, if the tachocline is in a turbulent state resulting from the growth of some shear flow instability (either MHD or purely hydrodynamical), then what we are seeing is the *end state* of the instability in its full nonlinearly saturated glory, *not* the originally unstable reference state. We should be especially weary of this problem if our stability analysis in §5.3.1 indicated that the presumed reference state is near the stability limit, as eq. (5.34) is with $a \simeq 1$. In fact, this lead Watson to suggest that the amplitude of the observed horizontal differential rotation in the solar convective envelope, whatever its dynamical origin may be, is in fact *limited* by the hydrodynamical stability of the horizontal shear. In the solar tachocline however, the horizontal gradient is everywhere smaller than the envelope value, which would put us not at, but rather below, the hydrodynamical stability limit. This should restore some confidence in the results of the stability analysis.

So should we conclude, from the stability analyses carried out in §5.3.1, that an unmagnetized tachocline is stable with respect to horizontal shear flow instabilities? Probably, but still, maybe not. However, it is now for the proponent of the unmagnetized turbulent tachocline to demonstrate that their tachocline is indeed shear flow unstable.

5.4 The magnetized tachocline

There is another important way in which magnetic fields can alter the structure of the tachocline. We saw in §3.5 that torsional Alfvén waves propagating along a large-scale poloidal field could lead to very efficient angular momentum redistribution. In this section we investigate whether such magnetic stresses can play the role of enhanced horizontal turbulence in keeping the tachocline thickness within the bounds set by helioseismology. Rather than working out a full magnetized equivalent of the Spiegel & Zahn model, here we simply investigate the conditions under which magnetic fields can take the place of enhanced horizontal viscous coupling in reducing the inward spread of a purely viscous tachocline (as in §5.2.3).

Assuming axisymmetry and neglecting all meridional flows, we are back simply with eqs. (3.36), which we dealt with in the same context of internal angular momentum redistribution in a magnetized solar radiative core. This time however we omit any wind-induced torque, but must take into account the latitudinal differential rotation in the convective envelope. We restrict the solutions to the radiative core, at the upper boundary ($R_{\rm CE}$) of which we impose the following boundary conditions:

$$\Omega(R_{\rm CE}, \theta, t) = 1 - a_2 \cos^2(\theta) + a_4 \cos^4(\theta) \qquad (5.38a)$$

$$B_\phi(R_{\rm CE}, \theta, t) = 0, \qquad (5.38b)$$

with $a_2 = 0.1264$ and $a_4 = 0.1591$ in (5.38a), as in §5.1. The boundary condition on B amounts to assuming that the convective envelope acts as a perfect conductor. The symmetry/regularity boundary conditions are as before (eqs. [3.38*c,d,e*]). The initial conditions are now:

$$\Omega(r, \theta, 0) = 0.9412\Omega(R_{\rm CE}, \pi/2) \qquad (5.39a)$$

$$B_\phi(r, \theta, 0) = 0. \qquad (5.39b)$$

For the poloidal field we restrict our attention to D3-type configurations (see Fig. 3.5), which are characterized by poloidal magnetic fields completely contained within the radiative core. We also impose $\mathrm{R}_\nu = \mathrm{R}_m$ in order to reduce by one the dimensions of parameter space.

Figure 5.7 shows the evolution of a $\mathrm{R}_m = \mathrm{R}_\nu = 10^3$, $B_0 = 1\,\mathrm{G}$ solution over a time span of 2.6×10^4 years(∗). Thick solid lines are contours of constant angular velocity, and the thin lines are contours of constant B_ϕ (dashed $\equiv B_\phi > 0$, dotted $\equiv B_\phi < 0$). This should be compared to the solution for purely viscous evolution (Figure 5.2). In doing so, you need to know that adopting a value $\mathrm{R}_\nu = 10^3$ here amounts to a diffusion time $\tau \sim 10^5\,\mathrm{yr}$, for a one Gauss poloidal field[16]. The radial spread of the tachocline is now highly latitude-dependent, which is hardly surprising given the shape of the poloidal field (cf. Figure 3.5[C]). Note also how a strong latitudinal differential rotation builds up in the polar regions, down to greath depths[17].

Figure 5.8 is similar in format to 5.7, but now shows steady-state solutions for various values of the Reynolds numbers. Figure 5.9 shows radial cuts in $\Omega(r, \theta)$ and $B_\phi(r, \theta)$ for these solutions. The Ω-cuts are carried out in the equator ($\theta = \pi/2$), and the toroidal field cuts at mid latitudes ($\theta = \pi/4$). You should compare Figure 5.8 to the purely viscous steady-state solution plotted on Figure 5.3(A) for isotropic viscosities.

It is clear from both these figures that the tachocline thickness h decreases with increasing Reynolds numbers. Furthermore, in view of the definition of Reynolds numbers, a sequence of solutions with increasing $\mathrm{R}_\nu, \mathrm{R}_m$ at fixed B_0 is equivalent to increasing B_0 at fixed $\mathrm{R}_\nu, \mathrm{R}_m$. Physical insight into this behavior is readily obtained once one realizes that, just as with the magnetized spin-down calculations of §3.5, the asymptotic steady-state is reached once latitudinal transport of angular momentum by magnetic stresses balances the viscous stresses imposed vertically via the boundary condition. For a D3-type poloidal configuration and a very thin tachocline, and if one stays clear of the polar regions, this balance is well described by

$$\frac{1}{r^2}\frac{\partial}{\partial r}\left(\rho\,\nu r^4 \sin^2\theta \frac{\partial \Omega}{\partial r}\right) = \frac{1}{4\pi}\frac{B_\theta}{r}\frac{\partial}{\partial \theta}(r \sin\theta\, B_\phi). \tag{5.40}$$

Because of the imposed differential rotation at the upper boundary, the growth of B_ϕ in the tachocline is *not* controlled by a Lorentz Force-mediated reduction of the differential rotation, as in §3.5. Instead the growth of B_ϕ is quenched by resistive dissipation within the tachocline. In a steady-state, and for a thin tachocline ($h \ll R_{\mathrm{CE}}$), the ϕ-component of the induction equation reduces to

$$\sin\theta B_\theta \frac{\partial \Omega}{\partial \theta} = \frac{1}{r^2}\frac{\partial}{\partial r}\left(\eta r^2 \frac{\partial B_\phi}{\partial r}\right). \tag{5.41}$$

(∗) This and other solutions for various values of Reynolds numbers can be viewed as animations on the course Web Page.

[16] What's this? Why would the diffusion time have anything to do with the poloidal field strength?

[17] Given what you have (hopefully) learned in §3.5, what is the Alfvén timescale here?

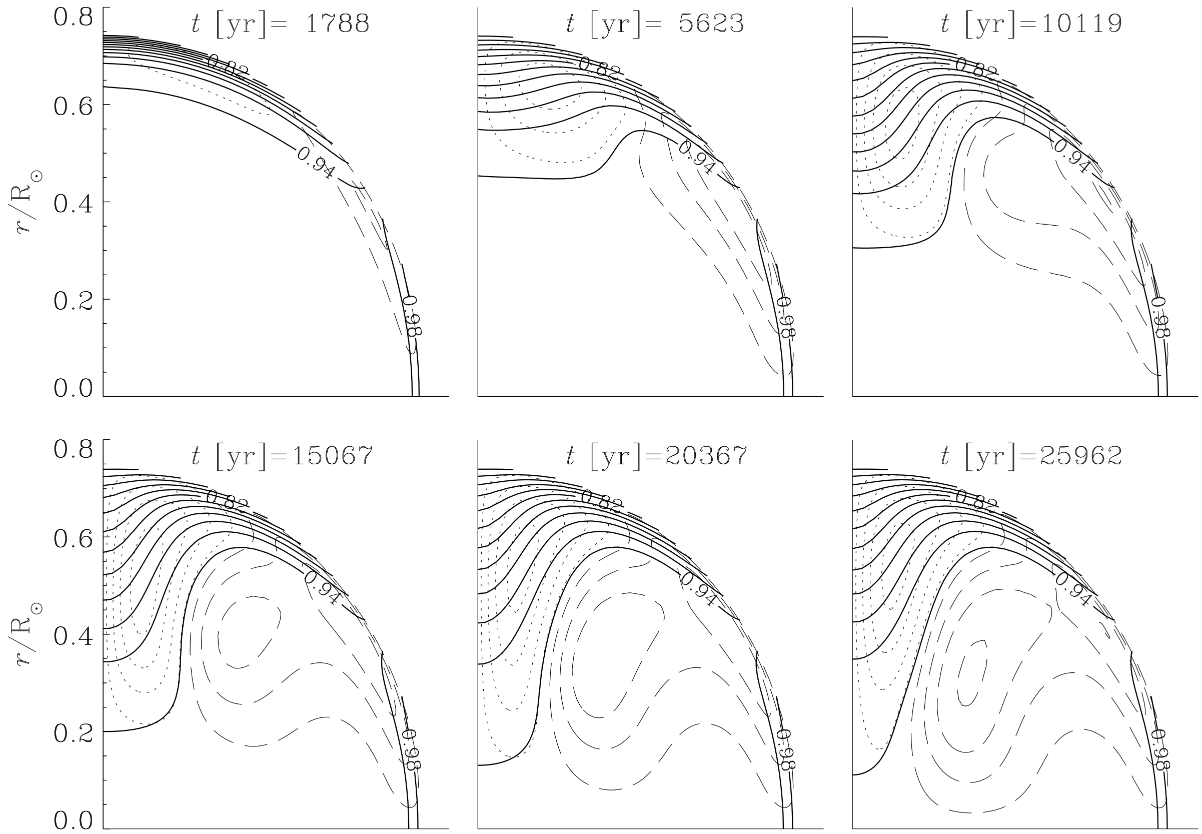

Figure 5.7: Inward spread of a (magneto-)viscous tachocline over 2.6×10^4 yr, in the presence of a large-scale poloidal field in the solar radiative core. The thick lines are isocontours of $\Omega(r, \theta)$, normalized to the (imposed) surface equatorial value and plotted at intervals of 0.02. The thin lines are isocontours of toroidal field B (dashed$\equiv B > 0$, dotted$\equiv B < 0$). The maximum toroidal field strength is $\sim 10^3$ G. Note the marked latitudinal dependency in the inward propagation of the tachocline, and the buildup of strong toroidal field and latitudinal differential rotation in the polar regions of the interior.

Dimensional analysis of eqs. (5.41) with $\partial/\partial r \to 1/h$, $r^{-1}\partial/\partial(\theta) \to 1/R_{\rm CE}$, and $r \to R_{\rm CE}$ yields

$$\left(\frac{h}{R_{\rm CE}}\right)^4 = \frac{4\pi\rho\nu\eta}{R_{\rm CE}^2 B_0^2} \tag{5.42}$$

which confirms the $h \propto B_0^{-1/2}$ scaling that can be inferred from Fig. 5.9. Recalling our definitions of the Reynolds numbers (eqs. [3.40]) in term of the Alfvén speed based on the poloidal field strength (eq. [3.39]), eq. (5.42) can be also expressed as

$$\left(\frac{h}{R_{\rm CE}}\right)^4 = \frac{1}{{\rm R}_\nu {\rm R}_m}. \tag{5.43}$$

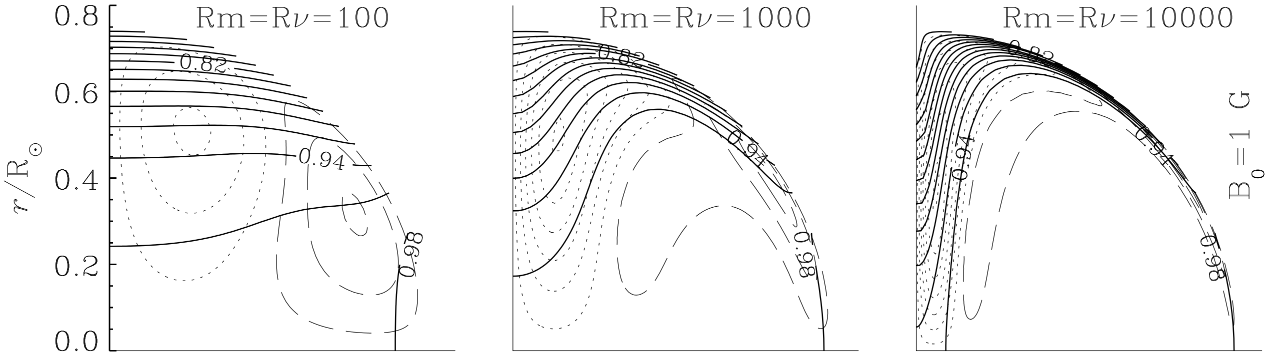

Figure 5.8: Steady-states reached asymptotically for solutions of increasing Reynolds numbers $\mathrm{R}_\nu, \mathrm{R}_m$ and fixed poloidal field strength $B_0 = 1\,\mathrm{G}$. The three solutions are identical to a sequence $B_0 = 0.1, 1, 10\,\mathrm{G}$ with $\mathrm{R}_\nu = \mathrm{R}_m = 10^3$. The format is similar to Figure 5.7. In the equator, the tachocline thickness decreases with increasing Reynolds numbers and increasing poloidal field strength.

For microscopic values of ν and η, and using as before $\rho \sim 0.1\,\mathrm{g\,cm^{-3}}$ as a representative density at the base of the envelope, eq. (5.42) can be rewritten as

$$h \simeq 100 B_0^{-1/2} \qquad [\mathrm{km}] \tag{5.44}$$

with B_0 in Gauss. Clearly, even a relatively weak field can produce a very thin tachocline. The toroidal field strength within the tachocline is roughly

$$B_\phi \sim B_0 \frac{h^2 \Delta\Omega}{\eta}, \tag{5.45}$$

where $\Delta\Omega$ is the pole-equator angular velocity difference imposed at the core-envelope interface. For $\Delta\Omega \sim 10^{-6}\,\mathrm{rad\ s^{-1}}$ and $\eta \sim 10^4\,\mathrm{cm^2\,s^{-1}}$, $B_\phi \sim 10^4\,\mathrm{G}$, independently of the poloidal field strength B_0[18].

Equation (5.40) and the subsequent dimensional analysis leading to eq. (5.42) clearly break down at high latitudes, where the field is no longer oriented primarily in the θ-direction, and the tachocline no longer thin (cf. Fig. 5.8). The force balance therein is obviously more complex than the simple balance between horizontal magnetic stresses and vertical viscous stresses, as implied by eq. (5.40). Problem (5.2) asks you to explore the dynamical details of the magnetized tachocline solutions at high latitudes.

The above derivation is valid for a situation where viscous dissipation is the primary mechanism leading to the inward spread of the tachocline. This is quite distinct from the situation encountered in the Spiegel & Zahn tachocline, where the thermally-driven large-scale flow is the primary agent responsible for the inward spread of the tachocline. An order-of-magnitude estimate equivalent to eq. (5.42)

[18] This seems rather counterintuitive. How can this be so?

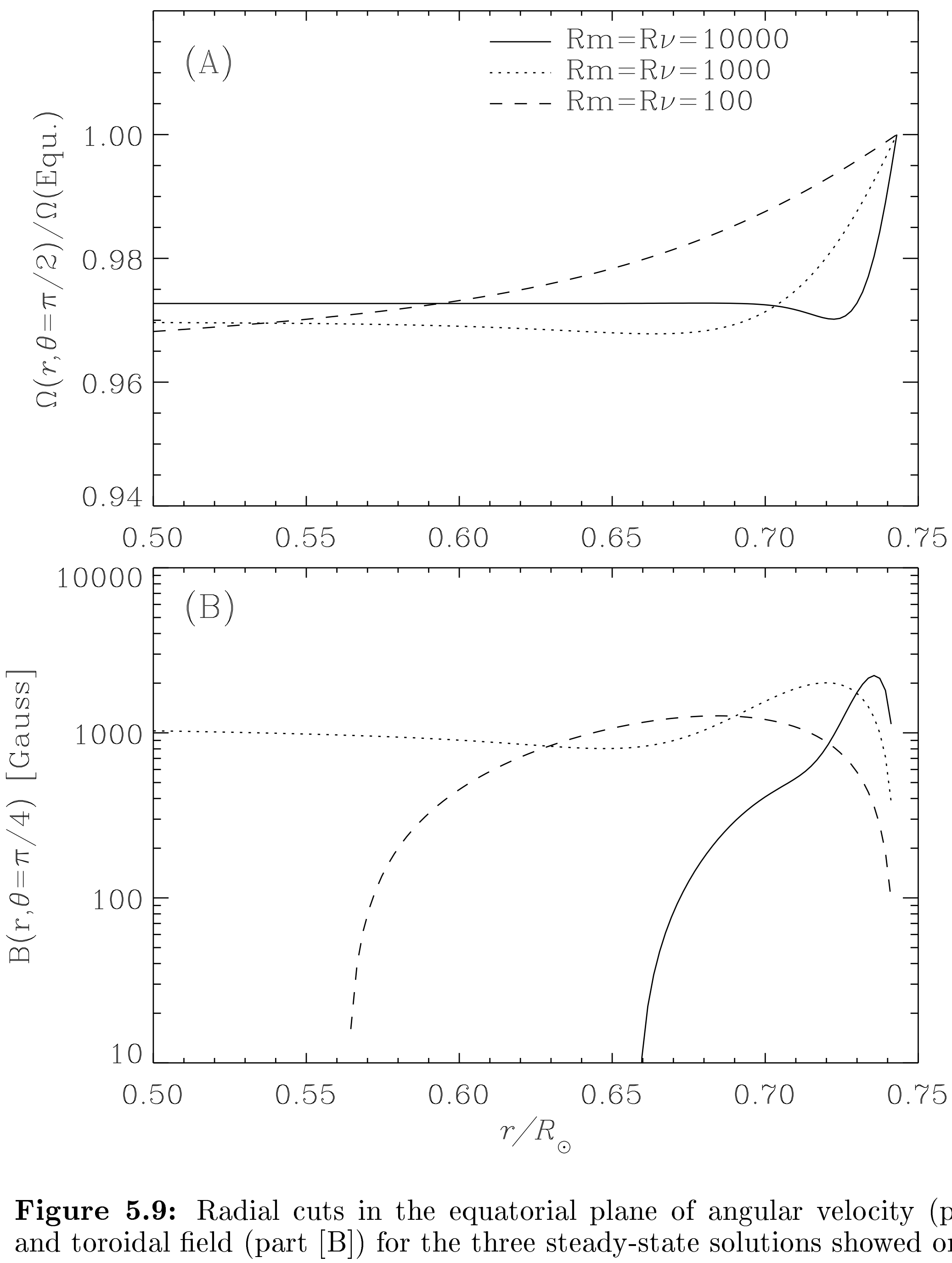

Figure 5.9: Radial cuts in the equatorial plane of angular velocity (part [A]) and toroidal field (part [B]) for the three steady-state solutions showed on Figure 5.8. Again remember that solutions for a sequence $B_0 = 0.1, 1, 10\,\mathrm{G}$ with $\mathrm{R}_\nu = \mathrm{R}_m = 10^3$ would look identical. The tachocline thickness decreases markedly with increasing Reynolds numbers (or increasing poloidal field strength), but the toroidal field within the tachocline is a much less sensitive function of these input parameters.

can still be obtained in the context of the Spiegel & Zahn model, by equating Spiegel & Zahn's hyperdiffusion term to the latitudinal magnetic stress:

$$\left[\frac{\chi}{\rho c_p}\left(\frac{2\Omega}{N}\right)^2\left(\frac{R}{\lambda}\right)^2\right]\frac{\partial^4\tilde{\Omega}}{\partial r^4}=\frac{1}{4\pi\rho r\sin\theta}\frac{B_\theta}{r}\frac{\partial}{\partial\theta}(r\sin\theta\, B_\phi) \tag{5.46}$$

assuming again that the growth of B_ϕ is limited by resistive dissipation (cf. eq. [5.41]). Dimensional analysis of eq. (5.46) then leads to

$$\left(\frac{h}{R_\odot}\right)^6=\frac{4\pi\rho\eta}{\lambda^2 B_0^2 t_{\rm ES}}, \tag{5.47}$$

or,

$$h \simeq 1300\, B_0^{-1/3} \qquad [\mathrm{km}] \tag{5.48}$$

The corresponding toroidal field is then

$$B_\phi \simeq 2\times 10^6 B_0^{1/3} \qquad [\mathrm{Gauss}] \tag{5.49}$$

Assuming $B_0 = 1\,$G then leads to $h/R_\odot \simeq 0.04$ and $B_\phi \simeq 10^6\,$G. This latter number is quite large. In fact it is rather unlikely that toroidal fields of that strength can be stored for significant lengths of time immediately beneath the convective envelope. We'll see in part IV of this class that $B_\phi \sim 10^5\,$G is likely an upper limit. This would then require $B_0 \sim 10^{-4}\,$G, but this would produce much too thick a tachocline[19].

5.5 Closure

We have considered in this chapter a number of hydrodynamical and magnetohydrodynamical tachocline models, of varying degrees of complexity and physical realism. In retrospect, perhaps the most striking thing is that our very simplest model, the purely viscous model of §5.1.2, is the only one that really reproduced observations. Why did we then bother to go on beyond that? Because there are good reasons to suspect this model to really be overly simplistic, even by the standards of this chapter...

We considered in some details the hydrodynamical tachocline model of Spiegel & Zahn, and showed that their hypothesis that horizontal shear flow instabilities provide the enhanced momentum transport needed in their model was not supported by a simple linear stability analysis. We then sought the physical origin of the needed horizontal coupling in various forms of interaction between magnetic fields and differential rotation. The MHD stability models of §5.3.2 are certainly suggestive but not yet conclusive, as rambled on in §5.3.3.

---

[19] How thick?

One difficulty facing any model relying on the presence of a large-scale magnetic field within the tachocline is the fact that the latter is the most probable site of the solar dynamo. Consequently, the magnetic field therein is likely to be time-dependent and topologically more complex that the (steady) configurations assumed in §5.4. In fact, this difficulty also plagues the magnetized spin-down calculations of §3.5, in particular for the configurations characterized by magnetic coupling at the core-envelope interface.

As far as the magnetic models of §5.4 go, all one can say at this stage is that whether or not magnetic fields can adequately limit the spread of the Spiegel & Zahn tachocline is a question that must await a true calculation, as opposed to the order-of-magnitude estimate derived here. Anybody interested?

Problems

(5.1) This problem lets you try your hand at linearization, in the context of the hydrodynamical stability problem discussed in §5.3. Don't miss this opportunity to give it a try in this simple case, you'll be happy you did it once you begin part III of the class.

(a) Linearize equations (I.1.16) and (I.1.17) to obtain eqs. (5.26) herein. This starts by omitting in the equations of motion all terms quadratic (or higher) in $\mathbf{u}$ components... and the rest is basically algebra.

(b) Fill in the missing mathematical steps leading from eqs. (5.26) to (5.32).

(5.2) This problem lets you examine force balance in the magnetized tachocline models of §5.4, for one specific steady-state solution ($\mathrm{R}_\nu = \mathrm{R}_m = 10^3$, $B_0 = 1\,\mathrm{G}$, cf. Fig. 5.8, middle panel). First go the course Web Page:

`http://www.hao.ucar.edu/public/education/astr7500.html`

From the top of the main Page, click on <u>Problems: software and data</u>, locate the appropriate subsection and follow the instructions given there to download the steady-state, 2-D profiles of angular velocity $\Omega(r,\mu)$ and toroidal field $B(r,\mu)$ for the $B_0 = 1\,\mathrm{G}$, $\mathrm{R}_m = \mathrm{R}_\nu = 10^3$ magnetized tachocline. The file `README.txt` contains detailed instructions as to the format of this data file, and suggestions for the calculation of numerical derivatives. Your first step will be to plot the solution, either as in Figure 5.8 (2-D contours) or 5.9 (radial cuts) to ensure that you can read the file in the proper order. Then,

(a) Calculate and plot the radial and latitudinal contributions to the viscous and Lorentz Forces, along a radial segment located at high latitudes ($\theta \simeq 10^o$, say). Which are the dominant contributions to force balance? Can you think of a simple explanation why this is so? Would you expect this to change in going to higher or lower Reynolds numbers? If so, in what ways and why?

(b) Since you have written all those computer codes, do now similar cuts at mid-latitudes ($\theta = 45^o$). Examine again the force balance; is eq. (5.40) actually a good approximation to the local dynamics within the tachocline?

Bibliography

Estimates for macroscopic transport coefficients (ν, χ, etc.) used in this chapter are again taken from

Spitzer, L. Jr. 1962, *Physics of fully ionized gases*, John Wiley/Interscience.

These days the tachocline is a hot target for helioseismic modelers. The trend seems to be that the thickness of the tachocline is decreasing with publication year... See the following:

Tomczyk, S., Schou, J., & Thompson, M.J. 1995, ApJL, 448, L57,
Kosovichev, A.G. 1996, ApJL, 469, L61,
Charbonneau, P., Christensen-Dalsgaard, J., Henning, R., Schou, J., Thompson, M.J., & Tomczyk, S. 1997, in IAU Symp. 181, *Sounding solar and stellar interiors*, in press,
Basu, S. 1997, MNRAS, in press, .

The tachocline model discussed in §5.2 is due to

Spiegel, E.E., & Zahn, J.-P. 1992, Å265106

see also

Elliott, J. 1997, Åin press .

The hydrodynamical stability of the solar latitudinal differential rotation was investigated by

Watson, M. 1981, G&AFD, 161, 285,

and its magnetohydrodynamic equivalent, as discussed in §5.3.2, much more recently by

Gilman, P.A., & Fox, P.A. 1997, ApJ, 484, 439.

Magnetoviscous tachocline models essentially identical to those discussed in §5.4 were first constructed by

Rüdiger, G., & Kitchatinov, L.L. 1997, Astr. Nach., [August 1997].